



## Finite-Difference Frequency-Domain Method in Nanophotonics

Ivinskaya, Aliaksandra

*Publication date:*  
2011

*Document Version*  
Publisher's PDF, also known as Version of record

[Link back to DTU Orbit](#)

*Citation (APA):*  
Ivinskaya, A. (2011). *Finite-Difference Frequency-Domain Method in Nanophotonics*. Technical University of Denmark.

---

### General rights

Copyright and moral rights for the publications made accessible in the public portal are retained by the authors and/or other copyright owners and it is a condition of accessing publications that users recognise and abide by the legal requirements associated with these rights.

- Users may download and print one copy of any publication from the public portal for the purpose of private study or research.
- You may not further distribute the material or use it for any profit-making activity or commercial gain
- You may freely distribute the URL identifying the publication in the public portal

If you believe that this document breaches copyright please contact us providing details, and we will remove access to the work immediately and investigate your claim.

DEPARTMENT OF PHOTONICS ENGINEERING  
TECHNICAL UNIVERSITY OF DENMARK

FINITE-DIFFERENCE FREQUENCY-DOMAIN  
METHOD IN NANOPHOTONICS

*by*

Aliaksandra Ivinskaya

PHD THESIS

2011  
LYNGBY

Thesis submitted in partial fulfillment of the requirements  
for PhD degree in Electronics and Communication  
from the Technical University of Denmark

Supervisor:  
Andrei Lavrinenko

Submitted 20 April 2011

# Summary

Optics and photonics are exciting, rapidly developing fields building their success largely on use of more and more elaborate artificially made, nanostructured materials. To further advance our understanding of light-matter interactions in these complicated artificial media, numerical modeling is often indispensable. This thesis presents the development of rigorous finite-difference method, a very general tool to solve Maxwell's equations in arbitrary geometries in three dimensions, with an emphasis on the frequency-domain formulation. Enhanced performance of the perfectly matched layers is obtained through free space squeezing technique, and nonuniform orthogonal grids are built to greatly improve the accuracy of simulations of highly heterogeneous nanostructures. Examples of the use of the finite-difference frequency-domain method in this thesis range from simulating localized modes in a three-dimensional photonic-crystal membrane-based cavity, a quasi-one-dimensional nanobeam cavity and arrays of side-coupled nanobeam cavities, to modeling light propagation through metal films with single or periodically arranged multiple subwavelength slits.



# Resumé

Optik og fotonik er spændende og dynamiske forskningsområder i en rivende udvikling, der i høj grad baserer sig på mere og mere komplicerede nanosstrukurerede materialer. Numeriske beregninger er ofte uundvrlige for at øge forståelsen af lys-stof vekselvirkning i sådanne kunstige materialer. Denne afhandling præsenterer udviklingen af en rigoristisk finite-difference-metode til løsning af Maxwells ligninger i vilkårlige geometrier i tre dimensioner med fokus på frekvensdomæne-formuleringen. Gennem en metode til at presse det tomme rum opnås en forbedret virkning af perfekt tilpassede lag (Perfectly Matched Layers), og ikke-uniforme ortogonale net benyttes til at øge nøjagtigheden af beregninger for stærkt heterogene strukturer. Eksempler på udregninger med den tre-dimensionelle finite-difference-metode i frekvensdomænet i denne afhandling strækker sig fra lokaliserede tilstande i kaviteter i fotoniske krystal-membraner, kvasi-en-dimensionelle nanobjælke-kaviteter og rkker af side-koblede nanobjælke-kaviteter til modellering af lysudbredelse gennem metalfilm med sprækker der er mindre end bølgelængden.



# Preface

This thesis is based upon studies conducted during my stay at the Department of Photonics Engineering, Technical University of Denmark, Lyngby, Denmark. Initially I intended to work in quantum optics of nanostructures but my first encounter with the finite-difference modeling of photonic-crystal cavity has opened the realm so physically rich and computationally challenging in itself that I focused on the finite-difference methods to model photonic band-gap and metal-based nanostructures.

It is my great pleasure to take this opportunity and thank many people who helped me with my project — in the first place this is of course Andrei Lavrinenko, my principle supervisor. I am also grateful to Peter Lodahl and Jesper Mørk, my co-supervisors at the initial stages of the project. A critical component for my professional growth was communication with many colleagues from DTU and abroad, in particular Andrei Novitski, Andrei Sukhorukov and Dzmitry Shyroki, and the family-like and stimulating atmosphere created in the Metamaterials group here at DTU-Fotonik. I would also like to acknowledge Ulf Peschel (University Erlangen-Nürnberg) for his kind permission to use computing facilities of his group to model coupled nanobeam cavities in 2010.

A. Ivinskaya  
Lyngby, April 2011



# List of publications

## Journal papers

- P1. D. M. Shyroki, A. M. Ivinskaya & A. V. Lavrinenko, “Free-space squeezing assists perfectly matched layers in simulations on a tight domain,” IEEE Antennas and Wireless Propagation Letters, vol. 9, pp. 389–392, 2010.
- P2. A. M. Ivinskaya, D. M. Shyroki & A. V. Lavrinenko, “Modeling of nanophotonic resonators with the finite-difference frequency-domain method,” IEEE Transactions on Antennas and Propagation, accepted, 2011.
- P3. A. M. Ivinskaya, A. V. Lavrinenko, D. M. Shyroki & A. A. Sukhorukov, “Mode tuning and degeneracy in longitudinally coupled nanobeam cavities,” Applied Physics Letters, submitted, 2011.

## Conference proceedings

- C1. A. Ivinskaya & A. V. Lavrinenko, “Q-factor calculations with the finite-difference time-domain method,” XVI International Workshop OWTNM, Copenhagen, Denmark, PO-01.37, p. 43, 27–28 April, 2007.
- C2. A. M. Ivinskaya, A. V. Lavrinenko, A. A. Sukhorukov, D. M. Shyroki, S. Ha & Y. S. Kivshar, “Coupling of cavities: the way to impose control over their modes,” Proceedings of SPIE, vol. 7713, pp. 77130F-1–9, 2010.
- C3. A. M. Ivinskaya, A. V. Lavrinenko, A. A. Sukhorukov, S. Ha & Y. S. Kivshar, “Longitudinal shift in coupled nanobeams and mode degeneracy,” AIP Conference Proceedings, vol. 1291, pp. 121–123, 2010.
- C4. A. M. Ivinskaya, D. M. Shyroki & A. V. Lavrinenko, “Three dimensional finite-difference frequency-domain method in modeling of photonic nanocavities,” 12th International Conference on Transparent Optical Networks ICTON 2010, Mo.P.16-1–4, Munich, Germany, June 27 – July 1, 2010.



# Contents

<b>Summary</b>	<b>iii</b>
<b>Resumé</b>	<b>v</b>
<b>Preface</b>	<b>vii</b>
<b>List of publications</b>	<b>ix</b>
<b>1 Introduction</b>	<b>1</b>
1.1 Tailored light-matter interactions: photonic crystals . . . . .	2
1.1.1 Photonic-crystal-based resonators . . . . .	2
1.1.2 Calculation of $Q$ -factor with finite-difference methods .	6
1.2 Light at nanoscale: metallic nanostructures . . . . .	7
1.2.1 Phenomenological description of metal . . . . .	7
1.2.2 Nanostructured metals in optics . . . . .	9
1.3 Electromagnetics from computational perspective . . . . .	13
1.3.1 Maxwell's equations and transformation optics . . . . .	13
1.3.2 Application to the finite-difference methods . . . . .	15
1.4 The aim and outline of this thesis . . . . .	18
<b>2 Finite-difference time-domain method for resonators</b>	<b>21</b>
2.1 Formulation of the FDTD method . . . . .	22
2.1.1 Spatial discretization . . . . .	22
2.1.2 Time stepping . . . . .	23
2.2 $Q$ -factor evaluation with the FDTD method . . . . .	24
2.2.1 Excitation of single resonance in the time domain . . . . .	24
2.2.2 Sphere benchmark: field components or energy density?	26
2.3 Transfer to the frequency domain: motivation . . . . .	29
<b>3 Finite-difference frequency-domain method</b>	<b>31</b>
3.1 Two variations . . . . .	32
3.1.1 Monochromatic wave transmission analysis . . . . .	32
3.1.2 Eigenmode analysis . . . . .	32
3.2 Discretization matters . . . . .	34

3.2.1	Discretization of computational domain interior . . . . .	34
3.2.2	Boundary conditions and domain reduction . . . . .	38
3.3	Modeling of a sphere . . . . .	42
3.3.1	Adjusting parameters . . . . .	42
3.3.2	Convergence studies . . . . .	45
<b>4</b>	<b>Ultra-high-<math>Q</math> nanophotonic resonators</b>	<b>49</b>
4.1	PhC membrane cavity . . . . .	50
4.1.1	Equidistant mesh and arctanh squeezing function . . . . .	50
4.1.2	Non-equidistant mesh and $x/(1-x)$ squeezing . . . . .	52
4.2	Nanobeam cavity . . . . .	56
4.2.1	2D modeling: high- $Q$ design . . . . .	56
4.2.2	3D modeling . . . . .	61
<b>5</b>	<b>Coupled nanobeam cavities</b>	<b>65</b>
5.1	Two coupled nanobeams . . . . .	66
5.1.1	2D analysis of field profiles . . . . .	66
5.1.2	3D $Q$ and $\lambda$ dependence on the longitudinal shift . . . . .	71
5.2	Three coupled nanobeams . . . . .	75
5.2.1	Weak coupling regime . . . . .	75
5.2.2	Strong coupling regime . . . . .	77
<b>6</b>	<b>Metallic gratings</b>	<b>81</b>
6.1	Planar metallic slab at THz frequencies . . . . .	82
6.1.1	Analytic solution . . . . .	82
6.1.2	FDFD testing . . . . .	84
6.2	Single slit . . . . .	84
6.2.1	$1/f$ law for enhancement . . . . .	86
6.2.2	Enhancement dependence on the slit width . . . . .	87
6.3	Periodic slits in metal film . . . . .	88
6.3.1	10-nm-wide slit in gratings of different periods . . . . .	90
6.3.2	Changing slit width when the period is fixed . . . . .	96
<b>7</b>	<b>Conclusion</b>	<b>99</b>
<b>Appendix A</b>	<b>Fourier transformation</b>	<b>101</b>
A.1	Continuous Fourier transformation . . . . .	101
A.2	Discrete Fourier transformation . . . . .	102
<b>Appendix B</b>	<b>Fabry-Perot resonator: FEM versus FDFD performance</b>	<b>103</b>
<b>Bibliography</b>		<b>105</b>

# Chapter 1

## Introduction

Just half a century ago manipulating light at the micro- and nanoscale was hardly possible or even imaginable. By now progress in fabrication techniques and our understanding of light-matter interactions have turned optics into one of the most dynamic, rapidly developing and promising fields of mesoscopic physics; even the new term, photonics, was invented and widely accepted to emphasize numerous new developments and directions such as image resolution below diffraction limit [1–4] and superfocusing [5–7]; optical cloaking [8–11]; ultrafast photonic chips [12–16]; lossless, nonlinear and gain materials [17–19]; optical modulators [20, 21], couplers [22, 23], switches [24, 25] and light sources on nanoscale [26–29]. This is naturally followed by a multitude of applications to technology [30], biophysics [31, 32], energy harvesting [33–35], lightning [36, 37], and medical science [38–40]. And like fifty years ago it was hard to envisage the perspectives of semiconductor transistor in building computers and all of that today’s electronic equipment, it is in the same way unpredictable what current research activity in nanophotonics will lead to. What we can say with confidence yet is that in order to utilize the tremendous potential of classical and quantum optics phenomena in real-life applications, a systematic understanding and deep intuition for the behavior of light in various nanostructured arrangements should be developed by each practitioner in the field.

To develop such intuition for light-matter interactions in complex photonic bandgap or plasmonic structures, to design nontrivial devices and to explore new phenomena, efficient numerical modeling is the key. For an impression of typical basic problems faced in nanophotonics and computational electromagnetics today, we describe in the following introductory sections two examples: light trapping in photonic-crystal cavities and propagation through metal gratings. Then we formulate equations to be solved and sketch the ways we follow to do that cleverly, using the same ideas that underpin the recent rise of transformation optics. Formulating the aim and outline of this thesis closes the introduction.

## 1.1 Tailored light-matter interactions: photonic crystals

### 1.1.1 Photonic-crystal-based resonators

In the coming decade in physics great effort will probably be devoted, among other things, to improving quantum storage and teleportation, and the development of quantum computer. This would require increased level of control over quantum behavior of light. In experiments, quantum states are easily destroyed by decoherence induced by surroundings. To make use of quantum processes one should avoid this influence, or use specifically designed environment to modify the process considered. This is the case when an atom or a quantum dot — nanosized emitter in active material — is located inside a medium exhibiting modified density of electromagnetic states, i.e., a photonic crystal.

As a popular definition goes, photonic crystal is a structured medium that can block light within a range of frequencies called photonic band gap [41]. Main advantages of dielectric photonic crystal components over, for instance, their plasmonic analogues are low-loss operation and low-cost production. Photonic crystal based structures — beam splitters, cavities, slow light and logic devices — allow for a lot of diverse operations with light. Fundamental characteristic of photonic crystal that regulates quantum dot spontaneous emission lifetime is the local density of states, i.e. density of electromagnetic modes in a particular point in the structure. Changing photonic crystal geometry and quantum dot position placed inside the crystal can dramatically alter spontaneous emission rate. In fact, prospects to modify the density of states gave major motivation to investigate photonic crystals back in the years of their inception, and still they generate large interest from the fundamental cavity quantum electrodynamics perspectives [42–44].

A defect in photonic crystal gives rise to new modes with discrete frequencies inside the band gap and acts as a cavity capable of trapping radiation due to multiple reflections from the rest of the photonic crystal. A quality factor of a cavity mode is defined as  $2\pi$  times the ratio of the cycle-averaged total energy of the cavity to the energy loss per cycle [45–47]:

$$Q = 2\pi \frac{\frac{1}{T} \int_T \int_V w d^3\mathbf{r} dt}{-\int_T \int_V \frac{\partial w}{\partial t} d^3\mathbf{r} dt} \quad (1.1)$$

where  $w = \frac{1}{4}(\mathbf{E} \cdot \mathbf{D}^* + \mathbf{B} \cdot \mathbf{H}^*)$  is the period-averaged energy density of electromagnetic field,  $V$  the volume of the cavity,  $T$  the period of field oscillations, and minus in the denominator corresponds to the energy loss. Assume the energy density decays exponentially,

$$w(\mathbf{r}, t) = w_0(\mathbf{r}) e^{-\frac{\omega_0 t}{\xi}} \quad (1.2)$$

where  $\omega_0$  is the angular frequency of electromagnetic wave. Substituting this to Eq. (1.1) gives  $\xi = Q$ . This solution does not depend on which part of the cavity,  $V$ , we use to calculate the  $Q$ -factor. The electromagnetic field components of a *single* cavity mode are given by the usual solution of Maxwell's equations, the harmonic wave of frequency  $\omega_0$  with the exponential multiplier standing for the losses:

$$A(\mathbf{r}, t) = A(\mathbf{r}) e^{-\frac{\omega_0 t}{2Q}} e^{-i\omega_0 t} \quad (1.3)$$

Formula (1.3) is valid only for one mode being excited, when the field evolution can be described as single-exponential. Squared absolute value of Fourier decomposition of exponentially decaying harmonic signal,  $|A(r, \omega)|^2$ , gives a package of monochromatic waves spread near the resonance frequency  $\omega_0$  with the half-width  $\delta\omega = \frac{\omega_0}{Q}$  as shown in Appendix 1. Thus the  $Q$ -factor can be defined from  $|A(\omega)|^2$  averaged over the area,

$$Q = \frac{\omega_0}{\Delta\omega}. \quad (1.4)$$

When we deal with a high- $Q$  cavity, energy decays very slowly in it and only part of the total decay time is used for FFT. Frequency spectrum fitting to lorentzian is commonly done to reconstruct discretized signal correctly.

The dissipation of power described by the denominator of (1.1) can be rewritten in a more convenient way with use of the conservation law

$$\int_V \frac{\partial w}{\partial t} dv = - \oint_{\Gamma} \mathbf{S} \cdot \mathbf{n} ds \quad (1.5)$$

where  $\mathbf{S} = \frac{1}{2}\mathbf{E} \times \mathbf{H}^*$  is the Poynting vector,  $\Gamma$  is the surface surrounding the volume  $V$  and having the unit normal vector  $\mathbf{n}$ . So the quality factor is

$$Q = \frac{\omega_0 \int_T \int_V w d^3 r dt}{\int_T \oint_{\Gamma} \mathbf{S} \cdot \mathbf{n} d^2 r dt}. \quad (1.6)$$

For cavities formed by objects with dimensions comparable with the wavelength of light it is often difficult to define precise physical dimensions of the cavity, and it is possible only when the mode is excited. Indeed, resonance phenomena in nanoscale structures are often characterized by very intensive fields behind the borders of the objects formally shaping the resonator by itself. As a measure of light localization in the cavity it is convenient to use mode volume defined in quantum mechanics as

$$V = \frac{\int \epsilon(\mathbf{r}) |\mathbf{E}(\mathbf{r})|^2 d^3 r}{\max[\epsilon(\mathbf{r}) |\mathbf{E}(\mathbf{r})|^2]} \quad (1.7)$$

where  $\epsilon(\mathbf{r})$  is the dielectric permittivity and  $\mathbf{E}(\mathbf{r})$  the electric field, the integration assumed to be carried out through the whole space. In the finite-difference

implementation the integral is replaced by summation over the computational domain.

Photonic crystals (PhC's) are currently considered as a perspective platform to host low mode volume cavities with high quality factors. A defect can be formed in a photonic crystal by breaking a perfect symmetry of the structure either by removing or shifting basic constitutive units or by local modification of refractive index. The defect acts as a cavity capable of storing energy during time proportional to the  $Q$ -factor. For a quantum dot placed inside a defect in a photonic crystal as in Fig. 1.1a, the radiation rate is directly connected with the quality factor of the microresonator. This gives an explicit way to enhance the quantum dot radiative lifetime by increasing the  $Q$ -factor. Another important parameter is mode volume  $V$ . Radiative emission lifetime of an ideal emitter placed inside a cavity is given via Purcell's factor [48]:

$$F_p = \frac{3Q(\lambda/n)^3}{4\pi^2 V}. \quad (1.8)$$

Photonic-crystal-based cavities exhibit very high ratios  $Q/V$  [49, 50] and thus they are attractive for use as passive optical components in the rapidly developing area of cavity quantum electrodynamics [51, 52]. Astonishing quantum phenomena are possible to observe with this kind of cavities, such as the enhancement of luminescence, alternation of emitter lifetime, Rabi oscillations, single-photon emission, and the enhancement of slow down factor in electromagnetically induced transparency. A variety of high- $Q$ , low- $V$  cavity designs were proposed based on structural modifications in photonic crystal matrices [53–56]. Basically, for a photonic crystal featuring full 3D band gap, a defect in it should give the  $Q$ -factor approaching infinity, i.e., light can be kept inside the resonator infinitely long. However, fabrication of photonic crystals with full 3D band gap, e.g., inverted opals and woodpile structures and defects in them is quite complicated.

That is why a standard way to create a cavity is to use 2D photonic crystal platform, mostly silicon or GaAs slabs with perforation. Position of holes in a slab is manually defined, giving thus flexibility in the design and optimization of cavities and other photonic components. The main channel for loosing radiation from a free-standing membrane cavity is through coupling to radiative modes. In the plane of the slab photonic crystal acts as a distributed mirror strongly holding radiation, thus in-plane leakage of radiation from photonic crystal is typically small. By separating the energy flow into in-plane ( $\parallel$ ) and out-of-plane ( $\perp$ ) parts, we can write [57]:

$$\frac{1}{Q} = \frac{1}{Q_{\parallel}} + \frac{1}{Q_{\perp}}, \quad (1.9)$$

where  $Q$  is the total  $Q$ -factor,  $Q_{\parallel}$  quantifies losses only in the plane of the slab, while  $Q_{\perp}$  stands for the out-of-plane losses. Knowing that  $Q_{\parallel}$  is very large we immediately see that the total  $Q$ -factor is mainly governed by  $Q_{\perp}$ . In the out-of-plane direction light is primarily confined by total internal reflection, thus

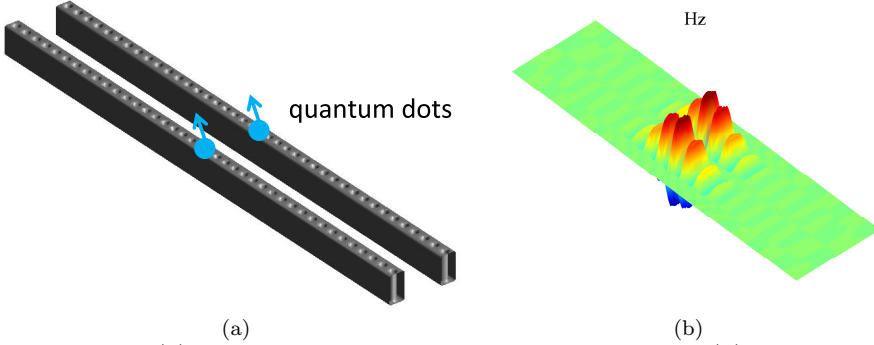


Figure 1.1: (a) Two coupled identical nanobeam cavities. (b) Even mode in coupled nanobeams.

the magnitude of  $\mathbf{k}_\perp$  vector should be as small as possible to reduce losses. In-plane mirror imperfections and parasitic leakage by coupling of the cavity radiation to vacuum modes are not clearly separated one from another and can be closely connected for some modes. Distribution of  $\mathbf{k}_\parallel$  for a specific mode can be obtained through spatial Fourier transformation of a given mode field component. The usual approach employed for optimization of cavities is through some guess for the design that would give  $\mathbf{k}_\parallel$ -vectors mostly lying far enough from the light cone.

Thus if some modes are to be confined at the nanoscale to achieve high  $Q$ , this should be done gently without abrupt changes in the structure geometry or refraction index because otherwise undesirable leakage will appear. In this sense the best designs are given by utilizing the mode-matching rule [58] when the holes pattern changes gradually going from the cavity center towards the mirror part. Waveguide-like [59] and nanobeam cavities [60] having simple arrangement of field maxima and minima along a straight line allow application of such mode matching approach and actually they give the highest of reported  $Q$ -factors. For modes of more complicated symmetries, for instance, for the hexapole mode in a one-hole-missing membrane [61], this approach is not readily applicable since the mode by itself can be easily destroyed and it disappears completely by a moderate geometry modification, especially if symmetry breaks even slightly.

Nanobeam cavity designed by mode-matching approach gains intensive interest [62]. It exhibits a set of highly desirable characteristics: high mode quality factor  $Q$ , low mode volume  $V$  (less than the cubic wavelength of light) and the smallest footprint size among other high- $Q$  cavities; this stimulates intensive investigations of nanobeam-related acousto-optic and optomechanic interactions [63, 64]. Tiny size of nanobeam cavities makes them also very promising for densely integrated photonic circuits.

One of the challenging tasks in cavity design remains the shaping of the far field radiated from the cavity to form a spot, which is necessary if this

cavity is to be used to make a laser. High-intensity emission to the far field is achieved by perturbing cavity design in order to create significant coupling to radiation modes. Recently periodic modification of hole radii in the mirror part was proposed as a stable way to extract radiation from the cavity [65]. Unfortunately, such solutions completely destroy high  $Q$ -factor desirable for lasing; a special design where all leakage of radiation goes into a single space channel is highly needed. Although active research is being carried out in this direction [66–69] the question whether it is possible to create a 2D-based photonic crystal cavity which simultaneously has high  $Q$  and is capable of highly collimated emission along specified direction is waiting for an answer.

Of particular interest are ensembles of cavities [70] with quantum dots placed inside, Fig. 1.1a. Three-dimensional description of such systems is not yet a routine task, but it is very important for fundamental investigations of light-matter interactions [71–73]. Coupling between resonators is an important feature that allows to shift operation wavelengths. Figure 1.1b shows one of the super-modes showing up when two cavities are brought together. This ‘even’ mode has the wavelength significantly different from a single-cavity eigenwavelength. Several cavities in close proximity to each other cannot be considered independently: their interaction should be taken into account as it can alter substantially the operation of these cavities on a densely integrated chip. Avoiding of parasitic coupling is crucial for photonic integrated circuits and in optic network design. On the other hand, there are many applications where strong and controllable coupling [74] is required: for example, in order to create low-threshold lasers [75], to observe Fano line shapes [76], to design field concentrators for detection of molecules [77], to create flat passband for slow light [78, 79], holographic storage [80], nonlinearities [81]. Formally, consideration of coupled cavities is directly paralleled with mode hybridization in molecules, that is why coupled resonators are often called ‘photonic molecules’ [82, 83].

### 1.1.2 Calculation of $Q$ -factor with finite-difference methods

Investigation of light behavior in photonic crystals of finite size in two or three dimension relies heavily on numerical computation methods. In fact, direct numerical methods attained rapid development in line with rise of nanophotonics and in particular with the development of the concept of photonic crystal. Multi-surface photonic crystal structures are difficult to describe even approximately using analytical considerations. One of the most challenging computational tasks is evaluation of the  $Q$ -factor of a resonator. High  $Q$  implies large, multi-period-extended photonic mirror capable of holding radiation for a long time avoiding the losses through coupling to radiative leaky modes. Traditional way here is to use time-domain modeling to simulate these spatially extended structures, with the subsequent extraction of  $Q$  by analyzing the ring-down of electromagnetic field components; such simulations can take considerable

time up to several days per single run for high- $Q$  three-dimensional resonator. Of course, for this type of problem we even do not mention the possibility of thorough convergence studies; only a few papers report such investigations [84]. Many approaches are suggested to minimize time consumption of  $Q$ -factor evaluation by transient analysis [85, 86] but systematic comparative studies of these various approaches are still lacking and this complicates the choice of a suitable one for a particular resonator considered.

Transition to the frequency domain analysis for cavity eigenmodes is very natural; it greatly reduces computation time and no post-processing is needed to determine the  $Q$ -factor. At the same time reliable frequency-domain solvers to find the  $Q$ -factor of a resonator are scarcely reported, probably because of large memory consumption inherent to many algorithms for computing the eigenvalues of the finite-difference matrix. This work is intended partly to address this issue by showing that the finite-difference frequency-domain (FDFD) method is capable of calculating high  $Q$  factors of membrane resonators even on a personal laptop if special care is paid to the physical issues of problem set-up, such as solution-adapted continuous grid density variation (of lower resolution in photonic crystal mirror part, for example; see Fig. 1.1b where the field decays rapidly from the nanobeam cavity center), exploiting the symmetries of a resonator to reduce computational domain, and squeezing the free space around a membrane.

## 1.2 Light at nanoscale: metallic nanostructures

### 1.2.1 Phenomenological description of metal

For metals containing free electrons of density  $\rho$  the expression for ‘effective’  $\epsilon$  can be constructed with use of relation for current  $\mathbf{J}$  generated by these free electrons when external electric field is applied:

$$\mathbf{J} = \sigma \mathbf{E}, \quad (1.10)$$

$\sigma$  being the conductivity of metal. Supposing time-harmonic excitation such that  $\partial_t \rightarrow -i\omega$ , we can write:

$$\mathbf{J} = \frac{\partial \mathbf{P}}{\partial t} = -i\omega \mathbf{P} \quad (1.11)$$

Combining (1.10) and (1.11) gives

$$\mathbf{P} = i \frac{\sigma}{\omega} \mathbf{E} \quad (1.12)$$

so that the effective permittivity of metal in this model can be introduced is

$$\epsilon^* = \epsilon + i \frac{\sigma}{\epsilon_0 \omega} \quad (1.13)$$

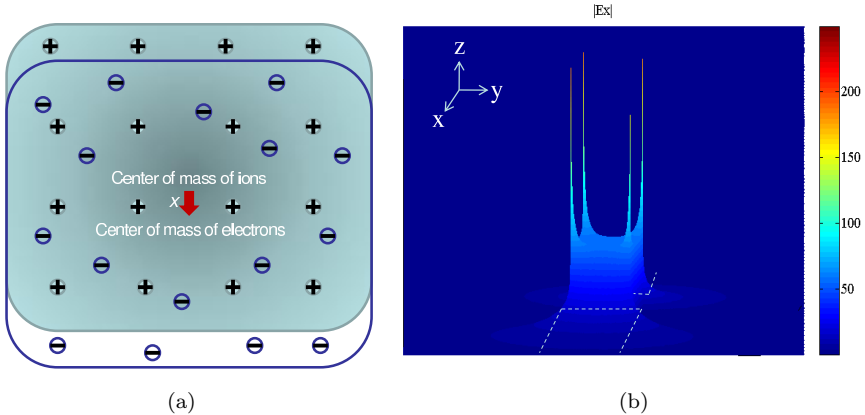


Figure 1.2: (a) Plasma model for metal. (b) Field singularities at the corners of a rectangular slit (shown schematically with white dashed lines) of width 10 nm in a gold grating of periodicity  $P = 1000$  nm in the air, calculated with the FDFD method. Incident light of wavelength 1015 nm is  $p$ -polarized so that surface plasmon polaritons are excited close to the Rayleigh-Wood anomaly. Z-axis shows the intensity of the field. The field is enhanced near the edges and inside the slit. Note that the peak singularities in the picture actually has the same weight, some asymmetry is due to inadequate color interpolation.

In this way polarization  $\mathbf{P}$  induced by the incident field can be incorporated into material parameters. Thus by redefining the dielectric function Maxwell's equations can be written in a source-free form for metals if there are no external charges and polarization now includes both intrinsic and external-field-induced terms. For phenomenological description of metal, frequency-dependent conductivity  $\sigma = \sigma(\omega)$  is normally assumed. The easiest way to derive dispersive permittivity from simple physical considerations is to approximate the metal by the model of free-electron gas contained in a positively charged ion lattice. Knowing that Maxwell's equations allow the existence of longitudinal electromagnetic mode in the bulk piece of metal under the condition that permittivity turns to zero, one can suggest that this resonance phenomenon is the main effect contributing to the frequency dependence of material parameters of free electron gas. Supposing that the whole electronic cloud can move with respect to the lattice and the distance between their 'centers of charge' is  $\mathbf{x}$ , see Fig. 1.2a, the equation of motion of the whole electronic cloud with concentration of electrons  $n$ , mass and charge of a single electron  $m$  and  $e$ , and damping coefficient of electron motion  $\gamma$  is

$$nm\ddot{\mathbf{x}} + nm\gamma\dot{\mathbf{x}} = -ne\mathbf{E}. \quad (1.14)$$

For harmonic electromagnetic field  $\mathbf{E}(t) = \mathbf{E}_0 \exp(-i\omega t)$  this gives the displacement law and hence the polarization as

$$\mathbf{P} = -n\epsilon \mathbf{x} = -\frac{ne^2}{m(\omega^2 + i\gamma\omega)} \mathbf{E} \quad (1.15)$$

Inserting this into the expression for electric displacement vector we arrive at the Drude model for metal permittivity:

$$\epsilon = \epsilon_\infty - \frac{\omega_p^2}{\omega(\omega + i\gamma)} \quad (1.16)$$

Here  $\omega_p = \frac{ne^2}{\epsilon_0 m}$  is plasma frequency at which in the lossless model ( $\gamma = 0$ ) electronic gas suspended in the air ( $\epsilon_\infty = 1$ ) responds to incident radiation by excitation of a bulk plasmon, so that  $\epsilon = 0$ . In general the term  $\epsilon_\infty$  can also be frequency-dependent and then additional terms described by Lorentzian functions appear to take into account the interband transitions. In this thesis we will mostly deal with pure noble metals at low frequencies that are very well described by simple Drude model, but one should remember that with the same easiness arbitrary dispersion can actually be handled by the frequency-domain method.

### 1.2.2 Nanostructured metals in optics

Metal-containing nanostructures exhibit amazing physical phenomena due to inherent property of metal to react to electromagnetic radiation through the induction of electron currents which are bound within metallic parts of the nanostructure. This can significantly change the properties of the system under the condition of resonance excitation. Electromagnetic cloaking, resolution under diffraction limit, negative refraction, extremely high local density of states are only part of the most cited phenomena obtained with the use of metal-containing structures. The most amazing feature of interaction of light with metals is the existence of plasmon polaritons — coupled resonance excitations of light and electrons close to the metal surface. Two main types of resonance-like effects are possible to observe in metallic structures [87]: resonances originating mainly from the geometry of the structure like Fabry-Perot conditions or Rayleigh-Wood anomalies (Fig. 1.3) and resonances by matching conditions between permittivity function of the metal and of the host matrix like Mie resonances, i.e. localized plasmons or propagating surface plasmon polaritons. Of course, for many realistic complicated structures it is difficult and sometimes not possible to distinguish between the two mechanisms as both of them simultaneously contribute to the process of light transmission and scattering, and geometrical parameters of the structure regulates contribution from each of the mechanisms. For instance, although Fabry-Perot and Rayleigh-Wood phenomena show up in dielectric structures, in metals their appearance is also associated usually with excitation of surface plasmons [88–90]. Of course, here

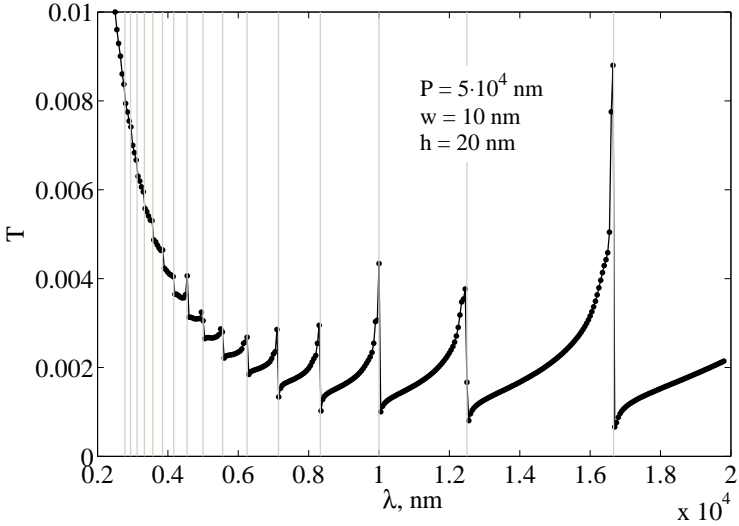


Figure 1.3: Transmission spectrum of the gold grating of period  $P$ , thickness  $h$  and width of the air opening  $w$  under illumination by  $p$ -polarized light, calculated with the FDFD method. Note that the gold behaves very much like the PEC in this wavelength range, and the Rayleigh-Wood resonances are quite accurately given by the rule  $P/n$ , where  $n$  is positive integer.

we are discussing Fabry-Perot ‘nanoscale’ resonances, e.g. those appearing in structures having one of the dimensions with size on the order of one wavelength or less. For example, slits in metal films of height  $h$  can give resonances at condition  $kh + \phi = \pi$  where  $\phi$  is the phase of reflection and  $k$  is the wave number of whatever mode is propagating back and forth inside the slit, and could, e.g., be the wave number of a gap plasmon polariton as in Ref. [90]. Because of the reflection phase in the resonance condition, Fabry-Perot transmission peaks are observed even for thin films [90].

### Localized plasmons

Physical explanation of the existence of localized plasmons is that at certain conditions the electrons in metal behave like plasma. For a bulk piece of metal, plasma-like behavior occurs at  $\epsilon_{\text{metal}} = 0$  when the longitudinal solution of Maxwell’s equations exists and leads to the emergence of bulk plasmons, whereas for small pieces of metals, for example small spheres, this transfers to condition of zero denominators in the Mie scattering coefficients giving the Fröhlich condition [91]:

$$\text{Re}(\epsilon_{\text{metal}}(\omega)) = -2 \epsilon_{\text{host}} \quad (1.17)$$

where  $\epsilon_{\text{metal}}$  stands for the metal permittivity and  $\epsilon_{\text{host}}$  for the dielectric function of the host medium.

More than a hundred of years from the discovery of Mie, his analytic theory for light scattering and transmission by a spherical particle is a reference point in various fields of research. Nowadays metal nanoobjects get much attention in photovoltaics due to high absorption at resonance [92], while closely placed nanoparticles arranged in special manner can lead to unique features like extra-high field enhancements and negative refraction due to magnetic resonances.

To describe the ensemble of nanoparticles, multiple scattering theories are usually employed where single scattering event is described in the quasi-static approximation [93]. In this approximation only the first order dipole mode is considered in Mie theory decomposition. When separate particles are small and their dilution is of low concentration the quasi-static approximation works perfectly, but for higher concentrations this approximation fails. The reason for this is unusual response of nanoobjects under illumination by evanescent waves, large amount of which is present in the near field of a resonating sphere for example. It was shown that evanescent radiation incident upon a simple sphere can efficiently excite higher order electric and magnetic multipoles [94] which leads to their scattering cross section many times enhanced compared to plane wave excitation and thus higher-order terms in Mie decomposition cannot be neglected. In a densely packed ensemble of particles they shine on each other not only by transversal scattered waves but also by evanescent waves, so analytical multiple-scattering theories cannot describe correctly all spectral features of the sample. Thus direct numerical methods to solve Maxwell's equations need to be employed in the case of aggregates of spherical resonators, although rigorous analytic solution is available for each single sphere.

### Surface plasmon polaritons

We consider localized plasmons which are resonant excitations of metal nano-objects, i.e. standing wave pattern is formed inside plasmon nanoparticles and these standing waves do not transfer energy. At metal-dielectric interface it is possible to excite surface plasmon polariton (SPP) that can propagate along the plane separating the two media. In the direction perpendicular to the surface, SPP has exponentially decaying tails. Dispersion relation for SPP propagating at the interface between two half-spaces is:

$$k_{\text{spp}} = k_0 \sqrt{\frac{\epsilon_1 \epsilon_2}{\epsilon_1 + \epsilon_2}} \quad (1.18)$$

Here  $k_{\text{spp}}$  is the propagation constant of SPP,  $k_0$  is the wave vector in vacuum,  $\epsilon_1$  and  $\epsilon_2$  are permittivities of metal and dielectric. Thus in contrast to localized plasmons, propagating SPPs can exist in wide range of frequencies. SPPs are launched by evanescent coupling through a waveguide or a prism, or another option is to introduce a corrugation to the flat surface, see Fig. 1.2 displaying strong diffraction of light near sharp metallic edges. It was suggested that

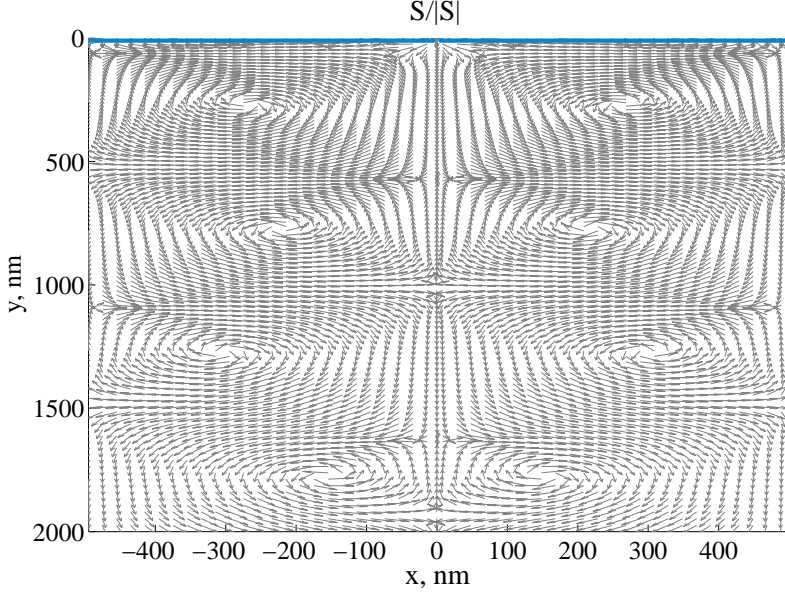


Figure 1.4: Distribution of the Poynting vector  $\mathbf{S}$  directions for the same structure and incident wavelength as in Fig. 1.2b. Only lower semi-space with light outgoing from a tiny 10-nm-wide aperture in the gold slab that is marked with blue is shown.

periodic perforation of metal surface or film with period  $P$  can excite SPPs due to momentum matching [95]:

$$k_{\text{spp}} = k_{||} \pm \frac{2\pi n}{P} \quad (1.19)$$

where  $k_{\text{spp}}$  is the surface plasmon wave vector,  $k_{||}$  is the wave vector of incident wave in the plane of the grating,  $n$  is integer. A feature that distinguishes SPP-based structures over dielectric nanostructured elements is a significant reduction in size of channels along which a signal can propagate, and accordingly the size of interconnects and other components made for plasmonic waves is reduced essentially as well. The main drawback of propagating SPPs used as operational signals is high loss inherent to metal, especially at telecom and optical frequencies. Hybrid modes formed by coupling plasmonic with refractive-index-guided modes in dielectrics are proposed to increase propagation length of SPPs [96–98].

In this very common example of utilization of metals in optics — gratings — semi-analytical methods of field decomposition in the plane-wave basis, for example, are widely used. However, these methods may suffer from slow convergence with respect to the number of terms in a series representing periodic quantities on a grating of non-smooth profile, and they anyway use some

absorbing boundary conditions similar to those used in real-space methods; often, real-space numerical simulation has to be performed to confirm the results of these semi-analytical mode decomposition approaches [99].

Figure 1.2b shows how well the field singularities can be described if non-uniform mesh is introduced to better resolve high-intensive fields near the metal edges. Evanescent waves close to these hot spots in metals are very intensive and can spread far enough in space, so the computational domain should be extended accordingly to let these evanescent tails decay sufficiently. This is not the only reason why metallic structures require thick air buffer: see the energy flow behind metal grating illuminated with *p*-polarized light in Fig. 1.4 which is characteristic also for off-resonance condition [100, 101]. To calculate transmission by grating correctly, at least some field vortices should fall inside the computational domain — otherwise numerical accuracy degrades very fast. This motivates the application of free-space squeezing for metallic structures no matter whether the structure is on or off resonance.

By now we have discussed two examples: aggregates of metallic spheres and gratings, where application of some analytic considerations is possible. It was shown [99] that these semi-analytical approaches sometimes cannot catch all the features inherent to metal-dielectric structures and some help from direct brute force methods is required. A huge variety of plasmonic structures, in particular those emerging within new fascinating directions in optics such as invisibility or negative refraction, have such complicated shapes that it would not be possible to explore them at a sufficient level at all if not the usage of direct numerical methods.

## 1.3 Electromagnetics from computational perspective

### 1.3.1 Maxwell's equations and transformation optics

The equations that are known for more than a century and still form the basis for much of the current progress in nanophotonics are Maxwell's equations:

$$\nabla \times \mathbf{E} = -\partial_t \mathbf{B}, \quad \nabla \cdot \mathbf{B} = 0 \quad (1.20a)$$

$$\nabla \times \mathbf{H} = \partial_t \mathbf{D} + \mathbf{J}, \quad \nabla \cdot \mathbf{D} = \rho \quad (1.20b)$$

where **E** and **B** are the electric and magnetic ‘force vectors’ while **D** and **H** are the electric and magnetic ‘flux vectors,’  $\rho$  and **J** denote charge and current densities. The richness of solutions to Maxwell's equations owes itself to a great variety of natural and artificial materials and structure geometries giving rise to various forms of the constitutive relations between excitation fields **E**, **B** and inductions **D**, **H**; in many cases they can be written as simply as

$$\mathbf{D} = \epsilon_0 \mathbf{E} + \mathbf{P} = \epsilon_0 \epsilon \mathbf{E} \quad (1.21a)$$

$$\mathbf{B} = \mu_0 \mu \mathbf{H}. \quad (1.21b)$$

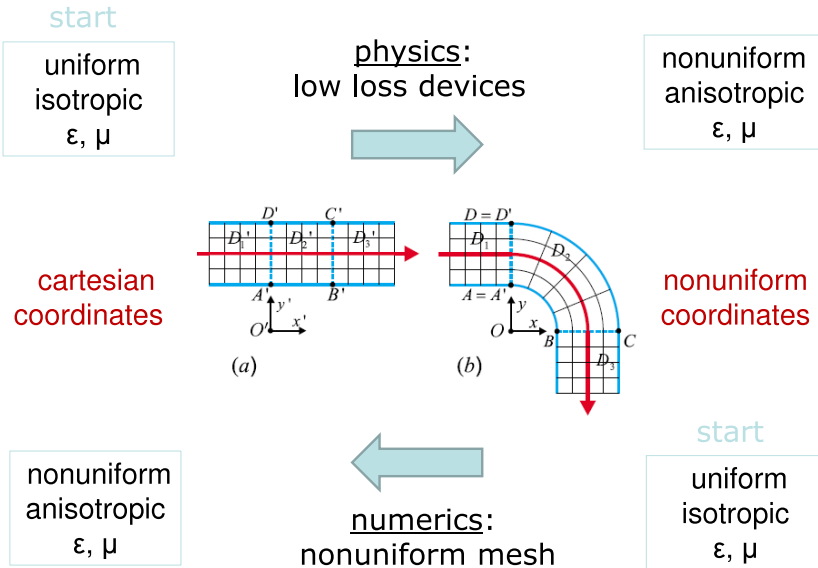


Figure 1.5: Covariance of Maxwell's equations applied to optimize devices in optics and for creation of non-uniform meshes in computational electromagnetics. (a) and (b) are after [102].

Here  $\epsilon_0$  and  $\mu_0$  are the electric permittivity and magnetic permeability of vacuum,  $\epsilon$  is the relative permittivity of medium considered. The intrinsic medium polarization  $\mathbf{P}$  is related to the electric field through the susceptibility  $\chi$ ,  $\mathbf{P} = \epsilon_0\chi\mathbf{E}$ , and the relative permittivity is thus  $\epsilon = 1 + \chi$ .

A great deal of activity in optics in the last years exploits the transformation invariance of Maxwell's equations, i.e., the property to look the same in different coordinate systems [103]; even a specific term, transformation optics [11, 104, 105], was coined to represent this new fascinating area of research. When going from one coordinate frame to another linked according to a differentiable law, all the transformation properties are enclosed in the permittivity, permeability and electric and magnetic field transformation laws while the form of Maxwell's equations preserves unchanged. The  $x$  to  $x'$  mapping (spanning over all coordinates is supposed here) gives the jacobian

$$[J] = \frac{\partial x'}{\partial x} = [J(x')], \quad (1.22)$$

and material parameters in the primed system are:

$$[\epsilon'] = |\det J|^{-1} [J] [\epsilon] [J]^T \quad (1.23a)$$

$$[\mu'] = |\det J|^{-1} [J] [\mu] [J]^T \quad (1.23b)$$

Here we suppose that knowing the analytical dependence  $x = x(x')$  material properties can be redefined in primed system, for example, dielectric function is written as  $\epsilon \rightarrow \epsilon(x(x')) = \epsilon(x')$ . The form of transformation rules for electric and magnetic fields is one and the same: if for simplicity the field is denoted as  $\mathbf{F}$ , in the primed space it will take the value

$$\mathbf{F}' = [J^{-1}] \mathbf{F} \quad (1.24)$$

This formula means that, for example, when a new, primed system is three times ‘stretched’ in one direction,  $x'_i = 3x_i$  and hence  $J = J_i^{i'} = 3$ , the field components pointing along the  $i^{\text{th}}$  direction are three times ‘stretched’ in the  $x'$  coordinate frame. This opens a new way to manipulate fields through a fairly simple mathematical tool. The field can be easily stretched [106], squeezed [102, 107], screwed [102, 105] and pushed out from some place [9] at the price of complicated artificial  $\epsilon$  and  $\mu$ . Starting from electromagnetic wave in free space the desirable field distribution can be sculptured by choosing appropriate curvilinear system of coordinates, permittivity and permeability of the designed component are given by equations (1.23). These permittivity and permeability are to be used in real space devices to deform the fields in the same way as nonuniform system of coordinates modifies orthogonal grid in cartesian frame.

As an example we can consider the design of a waveguide bend as shown in Fig. 1.5a,b. Light travelling trough the waveguide from Fig. 1.5b with material properties derived via transformation approach will not experience leakage of radiation at the bend in contrast to waveguide with somehow otherwise chosen  $\epsilon$  and  $\mu$  profiles. In fact, both sides of Fig. 1.5 correspond to Maxwell’s equations written in free space with the only difference that they are described by two different ways with coordinate transformation method applied to transfer from left to right. Thus transformation optics not only suggests the recipes to shape fields but also to create absolutely lossless devices. Of course after using approximations to simplify anisotropic  $\epsilon$  and assigning  $\mu$  the unity value, unwanted scattering is added and the losses appears [8–10]. But still the device might preserve its main functionality, besides there are some tricks to overcome too complicated material parameters. For example, if coordinate transformation is applied in a plane and only  $p$ -polarization (with electric field vector lying in that plane) is of interest,  $\mu$  is not changed if the determinant of the jacobian is unity [11, 102].

### 1.3.2 Application to the finite-difference methods

The key observation for efficient numerical electromagnetics modeling is that Maxwell’s equations have a Cartesian form with respect to arbitrary coordinate

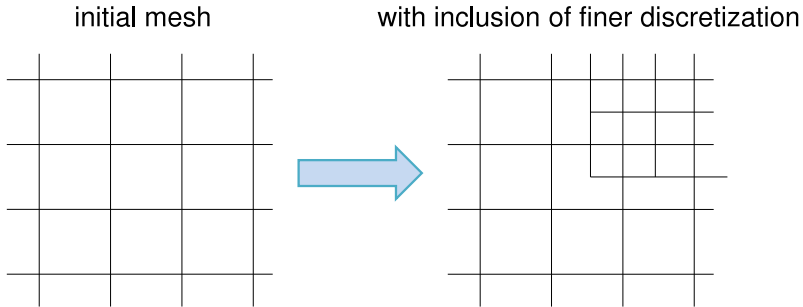


Figure 1.6: Sample of a two-dimensional finite-difference grid with a subgridding region introduced on the right.

system and for arbitrary medium because they do not involve metric quantities at all, in their naturally invariant form. Figure 1.5 illustrates how the transformation invariance can be used for the design of optical components (top part) and in computational electromagnetics (bottom part). In the case of numerics we swap the order of operations when applying the coordinate transformation method. It is illustrated at the bottom part, where now we go from right to left. The invariance of Maxwell's equations helps in several important areas in numerical modeling:

The first is nonuniform gridding. Various approaches were proposed to locally improve the meshing as, for example, shown in Fig. 1.6 where the discretization changes in a stepwise manner between the coarse grid region and the subgridding region. This approach is justified for some time-domain algorithms since the time step in the region of coarse discretization can be kept large to reduce computation time drastically, but the time coupling of the coarse and the fine grids is a nontrivial problem [108–111] and noticeable artificial reflection of electromagnetic wave propagating along the numerical grid may occur [85]. In the frequency domain, if no special care is taken of the fine-to-coarse grid interface, the convergence rate of a numerical scheme deteriorates on the grid with jumps in sampling and thus, abrupt variation of discretization should be avoided in favor of gradually varying mesh density.

When building such physically nonuniform grid of varying density to better resolve fine features of the structure, the form-invariance of the governing differential equations allows to work with one and the same, ‘logically Cartesian’ code for equidistant orthogonal meshes while hiding the complexity of grid geometry into the covariantly transformed permittivity and permeability tensors (1.23). If smooth analytic function is used to create non-equidistant mesh, it assures the impedance matched transformation leading to the absence of reflection in the region of transition to the finer mesh.

Another important application of curvilinear grids (and hence the form-

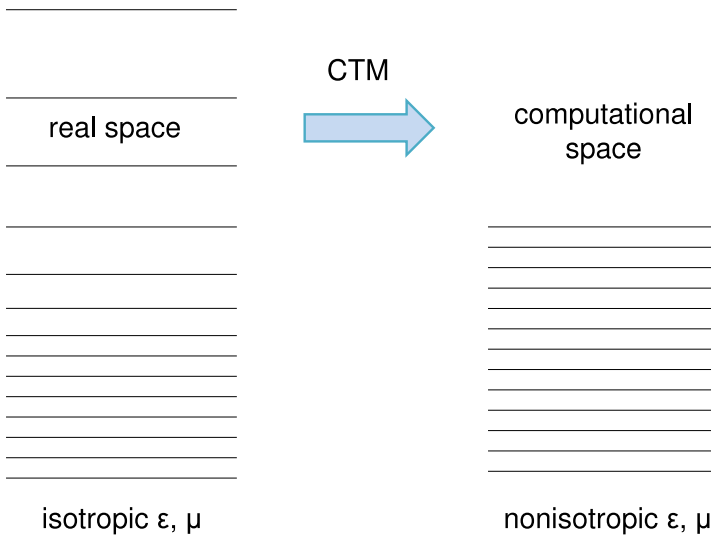


Figure 1.7: An example of employment of transformation optics approach to introduce stretched mesh and for squeezing of free space.

invariant formulation of Maxwell's equations) is modeling material objects with curved surfaces, when it is reasonable to transfer from Cartesian frame to the curvilinear system of coordinates such that the coordinate surfaces follow actual material boundaries of the structure. Thus, sinusoidally patterned gratings and bend waveguides like in Fig. 1.5b can be 'straightened' in appropriate coordinates what in turn helps to avoid stair-casing in describing curved boundaries.

Third, by transferring to curvilinear system of coordinates some objects can be described with lesser degrees of freedom, i.e. the dimensionality of the problem can be reduced [112]. In these non-Cartesian systems of coordinates, e.g. spherical or cylindrical or helical, there is no need to use new expressions for the curl and div operators modified because of transfer to curvilinear coordinates, but instead the invariant form of Maxwell's equations with material parameters evaluated via (1.23). This makes it possible to use standard rectangular-grid-based 2D numerical codes for VECSELs, discs and spirals.

The fourth application is use of various nonlinear mapping functions between real and computational spaces in order to map the infinite open space onto the finite computational domain. This helps to mitigate the problem of open boundaries inherent to most problems in photonics. The perfectly matched layers (PMLs) were originally designed to absorb only oscillating electromagnetic waves while evanescent waves can be even intensified inside PMLs. Constructing the PMLs far from the resonating object and then squeezing

the PML-to-resonator distance [113] prevents perturbing the solution by the evanescent field tails originating from hot spots in nanostructured objects, for example, near sharp metal edges.

Thus we see that computational methods can benefit a lot from using the invariance of Maxwell's equations, and below in this thesis we use this invariance for free-space squeezing and nonuniform mesh construction.

## 1.4 The aim and outline of this thesis

The importance of efficient simulation tools for the design of nanophotonic devices is reflected by the rapid growth of the market of commercial software products for photonics in the last decade; moreover, widespread became the practice of using commercial black-box software for photonics simulations published even in the most highly ranked journals like *Nature*. Extensive benchmarks for both commercial and in-house developed software for numerical photonics and plasmonics are being published [115–117]; interestingly, the finite-difference frequency-domain (FDFD) method is not even listed in such benchmark com-

	Time Domain	Frequency Domain
Mesh generation effort	+	-
Transient simulation	+	-
Broadband solutions	+	0
Cosimulation	+	0
Low-frequency problems	-	+
Gigantic problems $> 10^{10}$ unknowns	+	-
Nonlinear materials	+	-
Nonlinear cosimulation	+	-
Field and particle beam simulation	+	-
EMC simulations	+	0
Eigenmode calculations	-	+
Highly resonant structures	-	+
Periodic structures	0	+

Figure 1.8: Table highlighting the performance of time- and frequency-domain methods in different problems in nanophotonics, from [114].

parisons.

In this thesis we simulate fairly complicated photonic and plasmonic structures for which we find the FDFD method the best choice. In particular, we consider the eigenmodes in PhC membrane based and nanobeam resonators, and light propagation through subwavelength metallic gratings whose period to slit width ratio reaches  $10^4$  and more. From Fig. 1.8 with a table comparing the time- versus frequency-domain methods published in a recent review [114] it is clear that such structures are advantageous to be simulated in the frequency domain. The structured FDFD method is chosen as the simplest and, potentially, most efficient one.

Maxwell's equations in their discretized form can be viewed not as some approximated version of continuous formulation but as a self-consistent and rigorous way to describe optics in condensed matter. Indeed, Maxwell's equations written for small volume (termed computational cell in the context of the finite-difference modeling) can be interpreted as the integral equations [118]; moreover, the placement of components on the staggered Yee grid corresponds to the geometric nature of oscillating electromagnetic waves. Thus the main origin of numerical errors in direct methods lies not in the discretization of the structure but rather in other approximations such as the substitution of open space with the PMLs and treatment of object boundaries with stircasing or dielectric index averaging approximations.

After sketching the FDTD formulation and its use in finding the eigenfrequency and  $Q$ -factor of a photonic-crystal membrane resonator in Chapter 2, we formulate the FDFD method in its two versions, one for the eigenmode analysis and another one for monochromatic wave propagation modeling, in Chapter 3. Two examples of application of the FDFD method to the eigenmode analysis in photonic-crystal resonators follow in Chapter 4: a photonic-crystal membrane based cavity and an elongated nanobeam PhC cavity. Then in Chapter 5 the coupling of two and more cavities is analyzed; and in Chapter 6 the FDFD method is applied to modeling light propagation and enhancement in extremely-sub-wavelength metal gratings in a broad frequency range.

As regards numerical aspects of modeling, our emphasis is on the choice of reasonable computational domain size and buffer layer width, use of squeeze transform layers in combination with PMLs to mimic infinite open space, and construction of grids of varying density to better resolve small features in the nanostructured materials. These issues, especially the construction (and placement) of absorbing boundaries, are not yet completely settled in the electromagnetic modeling community, which is indicated, for example, by the absence of the option to use absorbing boundaries in the eigenmode solver modules of such popular commercial software products as CST Microwave Studio or Comsol Multiphysics.



## Chapter 2

# Finite-difference time-domain method for resonators

Possessing all-embracing universality, time-domain analysis has firmly entered computational electromagnetics and rightfully holds the first place by quantity of diverse modeling tasks that they can solve. Commercialized finite-difference time-domain (FDTD) and transient finite-element method are everyday tools in hands of experimentalists demanding multiple routine calculations of device operation under fabrication constraints and imperfections. So there is no surprise that before passing to the FDFD algorithm we start by getting acquainted with its time-domain counterpart — the FDTD method — that already became a standard tool in nanophotonics.

One of the main advantages of transient algorithms is the possibility to simulate large structures (Fig. 1.8). Moreover, parallelization of the FDTD simulations has already become a well-established procedure for modeling of gigantic numerical problems. As for frequency-domain methods, parallelization is also possible here, however, it is not that well established and thus simulation of large models is not a strong point here. As another essential advantage we can mention obtaining a spectral response from the structure in the whole range of frequencies during a single run with excitation by a broadband pulse.

In addition, the FDTD algorithm has many extensions starting from inclusion of nonlinearity and to modeling coupled Maxwell-Bloch equations. To describe an ensemble of active quantum dots or nonlinear medium in nanosstructured environment an additional polarization term for the active material is usually included into the FDTD-discretized Maxwell-Ampere equation to take into account multiple reemission and reabsorption of light by quantum dots or nonlinear enhancement. Practically, similar polarization term is introduced also to describe metal dispersion in time-domain approaches.

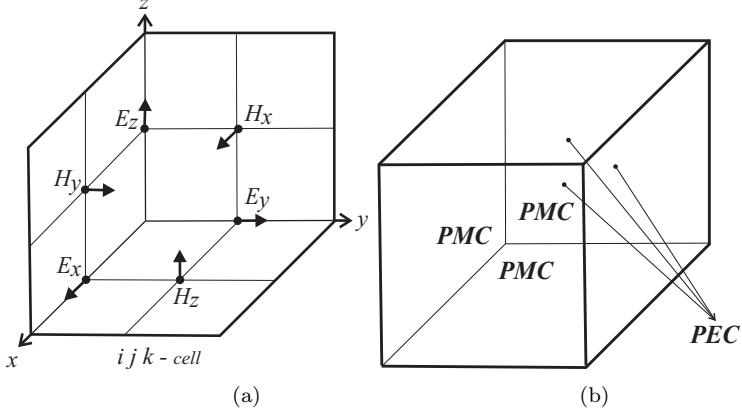


Figure 2.1: (a) Unit Yee cell with spatial positions of electric and magnetic field components. (b) Location of the perfect electric or magnetic conductor walls (PEC and PMC, respectively) at the outer boundaries of the computational domain.

## 2.1 Formulation of the FDTD method

### 2.1.1 Spatial discretization

The FDTD algorithm is based on discretization of Maxwell's curl equations in real space and tracing of the source field distribution in time [119]. We discretize the object according to the Yee mesh [120], Fig. 2.1a, and construct three different permittivity and three permeability arrays for each field component as their meshes are shifted spatially. Then we introduce six arrays for electromagnetic field components and use the initial values in these arrays and some given source field distribution (in space and time) to calculate the field evolution as governed by Maxwell's equations.

The source-free Maxwell's equations can be written as

$$\nabla_f \times \mathbf{E} = -\mu \partial_t \mathbf{H}, \quad \nabla_f \cdot \mu \mathbf{H} = 0 \quad (2.1a)$$

$$\nabla_b \times \mathbf{H} = \epsilon \partial_t \mathbf{E}, \quad \nabla_b \cdot \epsilon \mathbf{E} = 0 \quad (2.1b)$$

where subscripts \$f\$ and \$b\$ near the operators are introduced to point out their different action on a staggered Yee mesh [120], Fig. 2.1a, which can be illustrated for differential of some vector component \$A\$ along the \$x\$-direction:

$$\Delta_f A = A(x + \Delta x) - A(x) \quad (2.2a)$$

$$\Delta_b A = A(x) - A(x - \Delta x) \quad (2.2b)$$

The subscript \$f\$ means that the *curl* and *div* operators are constructed on the basis of the forward finite difference scheme, the subscript \$b\$ implies usage of

the backward finite differences. Each of forward or backward differences by themselves imply first-order accurate scheme if their result is assigned to one of the side points. However, on the staggered Yee mesh these differentials  $\Delta_{f,b}A$  are used to define dual-mesh field components positioned in the points in between the given mesh nodes. Thus in fact our scheme is a central-difference scheme giving second-order convergence.

Let's define now the differential operators if our vector fields are represented by three-dimensional arrays on Yee mesh. For example, 3D forward  $F_{...n...}$  and backward  $B_{...n...}$  derivatives acting along  $n$ th direction (corresponding to  $x$ ,  $y$  or  $z$  axis) with a step  $\Delta h_n$  on some field component  $A$ :

$$(F_n A)_{...i_n...} = \frac{1}{\Delta h_n} (A_{...i_n+1...} - A_{...i_n...}) \quad (2.3a)$$

$$(B_n A)_{...i_n...} = \frac{1}{\Delta h_n} (A_{...i_n...} - A_{...i_n-1...}) \quad (2.3b)$$

This operators are analogous to the MATLAB based function `diff`. With this definition of difference matrices we can easily obtain the boundary condition on the borders of the computational domain as depicted in Fig. 2.1b.

As on staggered Yee grid the divergence equations in Eq. (2.1) are automatically fulfilled [119] we are now interested only in constructing of *curl* operators with use of already defined differential operators. For example,  $(\nabla_f \times \mathbf{E})_x$  component can be written as  $F_y E_z - F_z E_y$  what proportional to the time derivative of magnetic field  $H_x$ .

## 2.1.2 Time stepping

Having defined space derivatives we can pass to writing update equations for field evolution in time (described by the superscript  $j$ ):

$$E_x^{j+1} = E_x^j + \frac{\Delta t}{\epsilon} (B_y H_z^j - B_z H_y^j) \quad (2.4a)$$

$$E_y^{j+1} = E_y^j + \frac{\Delta t}{\epsilon} (B_z H_x^j - B_x H_z^j) \quad (2.4b)$$

$$E_z^{j+1} = E_z^j + \frac{\Delta t}{\epsilon} (B_x H_y^j - B_y H_x^j) \quad (2.4c)$$

$$H_x^{j+1} = H_x^j - \frac{\Delta t}{\mu} (F_y E_z^{j+1} - F_z E_y^{j+1}) \quad (2.4d)$$

$$H_y^{j+1} = H_y^j - \frac{\Delta t}{\mu} (F_z E_x^{j+1} - F_x E_z^{j+1}) \quad (2.4e)$$

$$H_z^{j+1} = H_z^j - \frac{\Delta t}{\mu} (F_x E_y^{j+1} - F_y E_x^{j+1}) \quad (2.4f)$$

If a source is defined at some place in the computational domain, propagation of light from this source in time and space can be obtained starting from Eq. (2.4a–c) by inserting some initial values of fields corresponding to this

source. Then electric field at the next time step might be evaluated straightforwardly and if inserted to Eq. (2.4d-f) magnetic field components in the next time step can also be found. This time staggered calculation of electric and magnetic field components is often called leapfrogging. Proceeding the time cycle gives evolution of fields in time and space which was searched for. It could be shown that the necessary condition for the stability of the time-stepping algorithm is the Courant criterium relating the Yee cell size and the time step [119]:

$$\Delta t < \frac{1}{c\sqrt{1/\Delta x^2 + 1/\Delta y^2 + 1/\Delta z^2}} \quad (2.5)$$

## 2.2 *Q*-factor evaluation with the FDTD method

### 2.2.1 Excitation of single resonance in the time domain

To find all the modes for the given cavity when no preliminary information about resonance frequencies exists, a broad-band excitation pulse is launched in the system. In the case of multiple resonance excitation we see characteristic modulation of the electromagnetic field with time caused by superposition of the modes oscillation. For a 2D holey PhC slab with the cavity formed by omitting one hole (Fig. 2.2a) the evolution of the electric field is shown in Fig. 2.2b. The shape of field envelope is evidently due to superposition of several resonances giving the characteristic beating.

In Fig. 2.3 two fast Fourier transforms (FFT) are compared: the one including excitation pulse, the other one made from the field decay after turning off the source. From the first spectrum we are not able to predict the number of resonances and their wavelengths, while from Fig. 2.3b we can define two

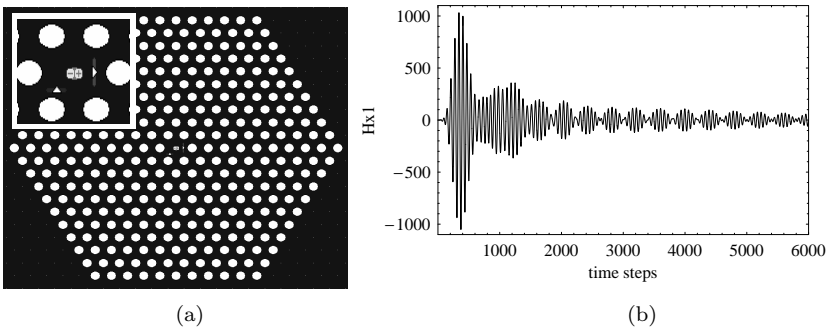


Figure 2.2: (a) One-missing-hole 2D-PhC microcavity. Dipole source polarized in perpendicular  $z$  direction is in the middle, two detectors shown as arrows. Lattice constant  $a = 254\text{nm}$ , air holes radius  $r = 0.3a$ ,  $n = 3.6$ . Square grid discretization is 10 nm. (b) Field evolution in the case of broad-band excitation recorded on the right vertical detector in Fig. 2.2a.

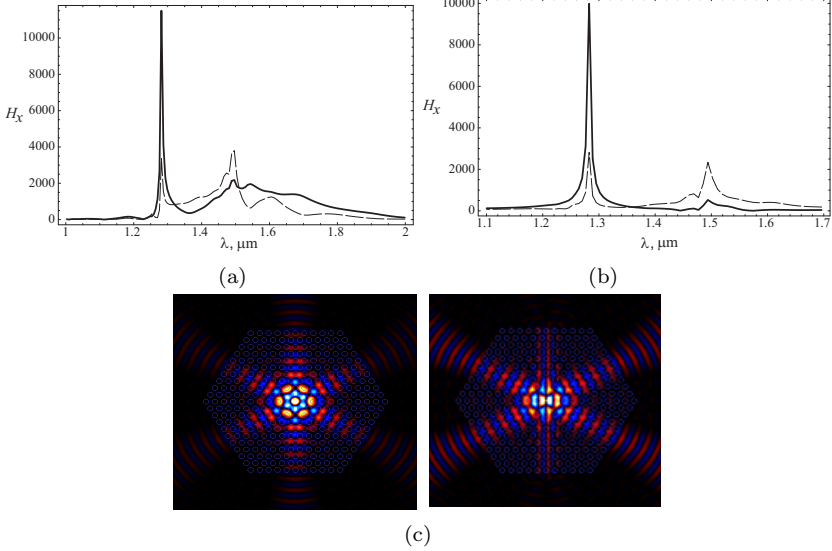


Figure 2.3: (a) Wavelength dependence of the field on two detectors, when FFT was made for the whole time (excitation + decay). (b) Wavelength dependence of the field on two detectors, when FFT was made only for field decay (after turning off the source). (c) Snapshot of  $E_z$  (left) and  $H_x$  (right) field component in a one-missing-hole membrane from Fig. 2.2a.

resonance wavelengths corresponding to two cavity modes. If excitation pulse is included into FFT then normalization of obtained cavity spectrum to FFT of the source should be made to extract the  $Q$ -factor and resonance wavelength of the mode correctly.

The duration, polarization and position of the source can play an important role in the excitation of a single resonance. To excite only one mode at  $\lambda = 1.28\mu\text{m}$ , we need to tune the source bandwidth so narrow as to do not overlap with the second resonance at  $\lambda = 1.5\mu\text{m}$ . With use of modulation theorem [121] we can approximately estimate the position of resonances if excitation signal is modulated. In Fig. 2.3c the distribution of the fields was detected at a some moment in time after turning off the source. Besides appropriate choice of excitation pulse, much care should be taken to assure the computational domain is large enough. Our simulations of low- $Q$  photonic crystal membrane cavities ( $Q$  around 100–200) using the FDTD-based Crystal Wave solver [85] gave stable results when the air cladding above the resonator was of about one wavelength wide.

The capabilities of the FDTD method to calculate high  $Q$ -factors are reflected in its wide usage for designing photonic crystal based cavities [53–56, 122, 123]. In these works featuring resonators with the highest reported  $Q$

factors, the  $Q$  extraction methods are based on the simplest approaches: the lorentzian fit after the FFT, tracing of electromagnetic field components ring down, sometimes together with direct definition of  $Q$  through Eq. 1.6. Knowing the resonance frequency  $\omega_0$ , the  $Q$ -factor can be defined with just one electromagnetic field oscillation period being traced. However, this ultra-fast procedure is usually accompanied by other methods of extraction which require vigorous postprocessing additionally to long execution time [56, 124, 125]. Thus in a proposed huge variety of cavity designs based on structural modifications in photonic crystals many alternative state-of-the art methods to calculate  $Q$  [55, 126, 126–129] are left unexploited at all. The possible reason for that is a lack of comparison of different extraction methods with almost no cross-references between articles developing alternative techniques what complicates the choice of most suitable approach for the user.

## 2.2.2 Sphere benchmark: field components or energy density?

In spherical coordinates, it is possible to investigate free oscillations of the electromagnetic field in the sphere analytically. The quality factor is extracted from the imaginary part of resonance frequency. It depends on the dimensionless parameter  $\omega_0 a/c$  (see §9.22 in [130]), where  $\omega_0$  is the angular resonance frequency,  $a$  the radius of the sphere and  $c$  the vacuum speed of light. Consider the dipole mode TE<sub>101</sub> for the sphere of refractive index  $n_{\text{sphere}} = 6$  embedded in air. Its analytical  $Q$ -factor is  $Q = 43.17$  at  $\omega_0 a/c = 0.512$  [131]. The resonant wavelength for the radius  $a = 0.16 \mu\text{m}$  is  $\lambda = 1.963 \mu\text{m}$ ; it is used as a

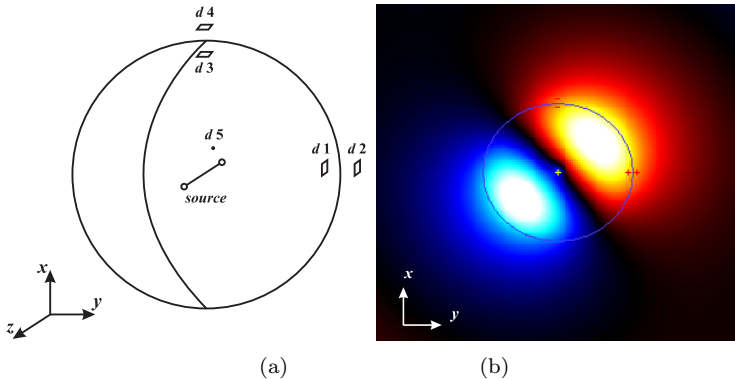


Figure 2.4: (a) Positions of a current source (close to the center) and detectors ( $d_1$ – $d_5$ ) in the nanosphere of radius  $a = 0.16 \mu\text{m}$  and refractive index  $n = 6$  in air. Dimensions of the computational domain are  $(0.8 \mu\text{m})^3$ , the grid resolution is 5 nm, PMLs width is 8 grid points. (b) Snapshot of electric field in the dielectric nanosphere after turning off the source.

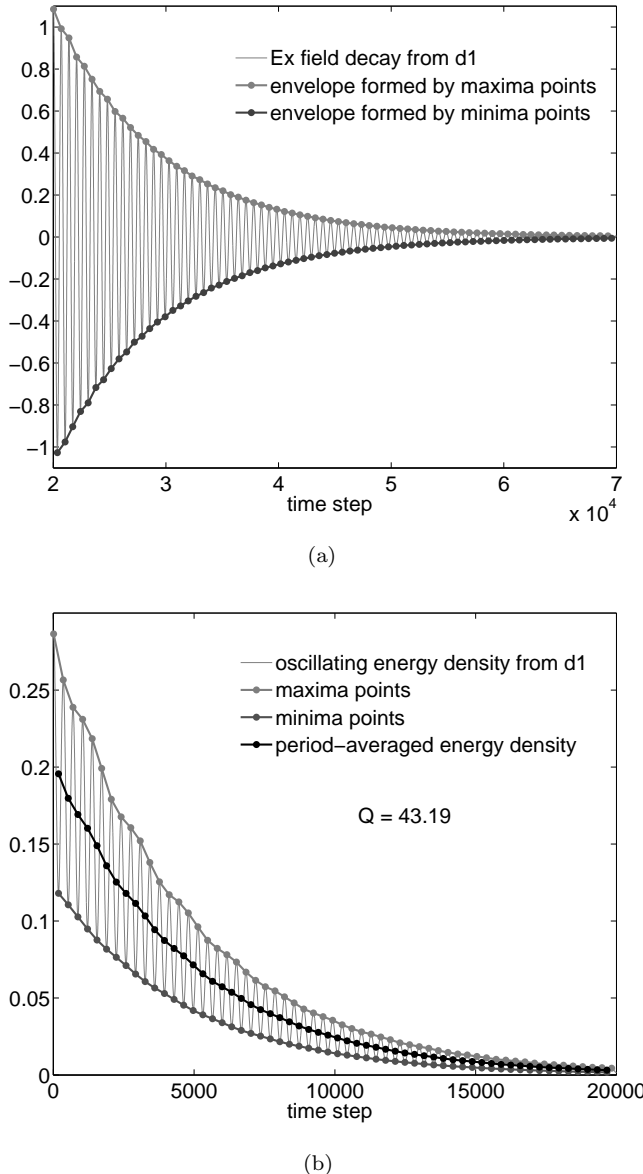


Figure 2.5: Analysis of field evolution in the case of the dipole mode excitation in the sphere from Fig. 2.4a. (a) Evolution of the  $E_x$  field component with positive and negative envelopes. (b) Oscillating and period-averaged energy densities.

central wavelength of a narrow-band signal to excite the sphere. The source is positioned in close proximity to the center of the sphere and five point detectors are located at different points inside and outside the sphere as shown in Fig. 2.4a. We made the FDTD calculations with use of the commercial package Crystal Wave [85]. By plotting the  $E_x$ -field distribution (Fig. 2.4b) we see that it is indeed a dipole mode.

According to Eq. (1.1) the  $Q$ -factor of a mode characterizes the cavity when there is no any influence from a source. Therefore, excitation pulses of finite duration are used. The field decay is analyzed to find  $Q$  and  $\omega_0$  after the pulse is switched off [132].  $Q$  and  $\omega_0$  are obtained from the evolution of electromagnetic field components: a lorentzian fit to the squared absolute value of the Fourier transformation  $A(\omega) = \mathcal{FT}[A(t)]$ , and an exponential fit to the envelope of  $A(t)$  formed by the minima or maxima points of an oscillating electromagnetic field,

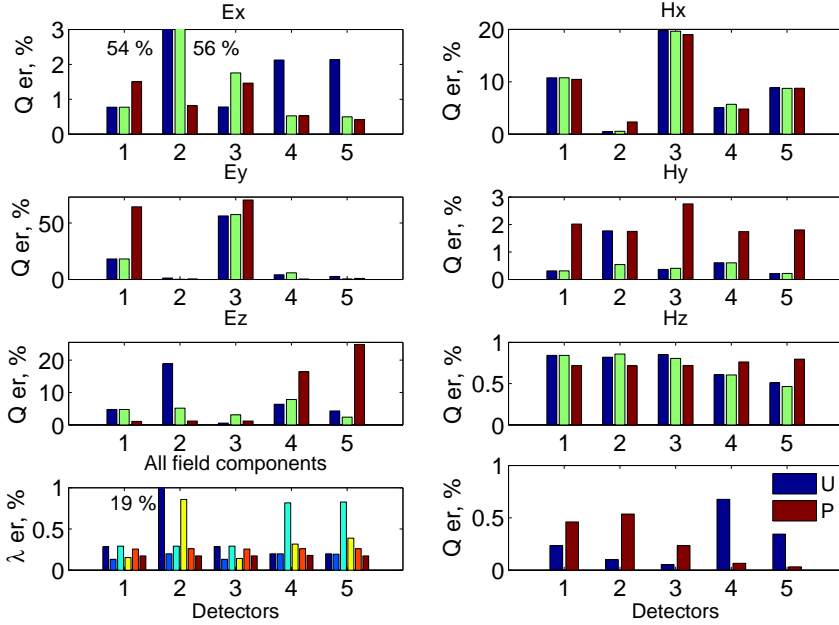


Figure 2.6: Top six graphs for each of the electromagnetic field components illustrate a  $Q$ -factor error given by the three methods: black bars— the exponential fit to the envelope of the field formed by maxima points in the time domain, grey—the same but with the minima points, white—the lorentzian fit in the frequency domain. Bottom left: wavelength error from the lorentzian fit in the frequency domain to all six field components. Bottom right:  $Q$ -factor error from the exponential fit to the period-averaged energy density  $U$  and Poynting vector  $P$ . Numbers on horizontal axis in all figures correspond to five different detectors.

Fig. 2.5a. Here  $A(t)$  designates any of the field components, which in the FDTD calculations are normally kept as real values. The oscillating energy density  $w$  evaluated directly through computed field components is a time-oscillating function. In order to get an exponential decay and to define the  $Q$ -factor it is period-averaged as shown in Fig. 2.5b.

Comparing time periods of signals straightforwardly from Fig. 2.5a and Fig. 2.5b, we can find that evolution of energy density is described by the FDTD algorithm with better maintenance of periodicity (counted directly in time steps) than for a single electromagnetic component: if for energy density inaccuracy in period comprises no more than one time step, for some field components it might reach several time steps. Thus energy density calculation balance simulation errors given by all field components in such a natural way that they are reduced compared to a simple averaging procedure.

The diagram in Fig. 2.6 shows relative  $Q$ -factor and resonance wavelength errors given by different methods. While fitting in the time domain as shown in Fig. 2.5, the angular frequency  $\omega_0$  was taken equal to its analytical value, so no additional error is introduced by inaccuracy in  $\omega_0$ . Nevertheless, single electric or magnetic field components give unstable  $Q$ -factor with unexpectedly high relative errors in some cases, while the energy density fitting has an error below 0.8%. So we conclude that the most accurate and robust way to define quality factor is via the exponential fit to the time-averaged energy density. In this case there is no need to collect information through the whole domain and it is enough to use only one point detector, placed arbitrarily inside or outside the sphere. In the case of multiple resonances, the period-averaged energy density will not be a single-exponential function anymore and we are forced to return to the analysis of single field components. This should be done with care; averaging of calculated results for  $Q$ -factor over the whole domain and for all field components is recommended.

## 2.3 Transfer to the frequency domain: motivation

Among numerical tools to determine cavity mode characteristics, one of the most widely used is the finite-difference time-domain (FDTD) method. In this chapter we compared the most robust extraction methods for analytical example of a sphere. It was shown that the obtained  $Q$ -factor values differ significantly from one extraction method to another and the electromagnetic field component being analyzed. The reliability of the single field component extraction method is put under doubt, and energy density analysis is found to be clearly advantageous. Yet many extraction methods rely on the analysis of single field components and some authors report severe problems with the FDTD technique for finding resonances with  $Q$  higher than  $10^3$  [133]. Going a bit ahead in Table 2.1 we list FDTD computational domain and cycle parameters together with some extraction methods, and compare them with the

	Time domain	Frequency domain
Post-processing	ring-down of fields; Harminv; Lorentzian fit; energy loss per cycle; Pade approximation; Prony's algorithm; pencil-of-function method	not needed
Adjacent eigenmodes	mixed	naturally separated
Air buffer layers	thick	moderate
Memory usage	moderate	high
Typical run time	day	hour

Table 2.1: Table comparing extraction methods, computational and user efforts for defining resonator characteristics with the time- and frequency-domain finite-difference algorithms.

features of the frequency-domain simulation tools. We see strong motivation to develop the frequency-domain counterparts of FDTD approaches what is done in the next chapters of the thesis. For the user of the numerical method a great advantage of the frequency domain technique over the time domain analogues is elimination of postprocessing steps in some tasks, e.g., no need to go through the analysis of time-domain signals to extract the  $Q$ -factor of a cavity mode, besides in many tasks the run time is greatly reduced as well. And if we are interested in field distribution in the structure illuminated by the plane wave of certain frequency, frequency-domain method is also the tool of natural choice.

# Chapter 3

## Finite-difference frequency-domain method

As an alternative to the time-domain modeling, we employ the 3D finite-difference frequency-domain (FDFD) method with the perfectly matched layers (PMLs) and free space squeezing. The algorithm can be formulated with ease for solution of a multitude of problems, for example, those involving arbitrarily dispersive materials and periodic media or modeling transmitted and reflected electromagnetic fields in the presence of monochromatic light sources. The quality factor and resonance frequency in the frequency domain appear straightforwardly, require no post-processing and do not depend on a choice of a specific fitting procedure. A typical FDFD run takes minutes while an FDTD simulation runs up to several hours for a comparable system and hardware. The FDFD technique applied to a particular system manipulates entire arrays representing electromagnetic field components and material permittivity and permeability on a structured grid, thus it is not so cumbersome and dependent on the mesh generation subroutines as the finite-element method [134].

From the early 1980's, three-dimensional finite-difference and finite-integral techniques in the frequency domain were applied to modeling of closed cavities and metal structures [135–140]. Today 3D frequency-domain method is used widely in microwave cavity analysis [114, 141, 142] and, to a lesser extent, in photonic bandgap computations where Bloch-periodic boundary eigenproblem is solved [143, 144]. Analysis of open photonic resonators with the 3D FDFD method was problematic, in contrast to photonic band calculations, for two main reasons: first, much larger, i.e., multiple-lattice-constant pieces of PhC matrices must be considered; second, nontrivial absorbing boundaries like the perfectly matched layers placed at sufficient distance from the modeled resonator are to be used instead of simple Bloch-periodic walls. These issues are specifically addressed when formulating and using the FDFD method in the current and subsequent chapters.

## 3.1 Two variations

### 3.1.1 Monochromatic wave transmission analysis

Maxwell's curl equations (1.20a) for the fields  $\mathbf{E}$ ,  $\mathbf{H}$  can be written in the frequency domain, after substituting  $\partial_t = -i\omega$ , as

$$\nabla \times \mathbf{E} = i\omega\mu\mathbf{H}, \quad (3.1a)$$

$$\nabla \times \mathbf{H} = -i\omega\epsilon\mathbf{E} + \mathbf{J}, \quad (3.1b)$$

where  $\mathbf{J}$  is the amplitude of electric current playing the role of a source for harmonic (monochromatic) light of frequency  $\omega$ . These equations can be viewed as a linear system which, at a given excitation  $\mathbf{J}$  and frequency parameter  $\omega$ , can be solved to obtain the 'joint' vector  $(\mathbf{E}, \mathbf{H})^T$ :

$$\begin{bmatrix} \nabla \times & -i\omega\mu \\ i\omega\epsilon & \nabla \times \end{bmatrix} \begin{bmatrix} \mathbf{E} \\ \mathbf{H} \end{bmatrix} = \begin{bmatrix} 0 \\ \mathbf{J} \end{bmatrix}. \quad (3.2)$$

Yet it would be better to reduce this system by combining the two equations from (3.1a) to arrive at

$$(\mu^{-1}\nabla \times \epsilon^{-1}\nabla \times -\omega^2 I) \mathbf{H} = \mathbf{S}. \quad (3.3)$$

with the source term  $\mathbf{S} = \mu^{-1}\nabla \times \epsilon^{-1}\mathbf{J}$  on the right hand side. To excite a plane wave, we can specify the amplitude of excitation current  $\mathbf{J}$  along some plane in the computational domain, with Bloch-periodic boundaries in the directions of that plane.

For better numerical performance of some linear algebra algorithms it would be advantageous to have the system matrix symmetrized; this can be actually done easily by scaling the coordinates so that  $\tilde{\mathbf{H}} = \sqrt{\mu}\mathbf{H}$ ,  $\tilde{\mathbf{S}} = \sqrt{\mu}\mathbf{S}$ , and

$$\left( \sqrt{\mu^{-1}} \nabla \times \epsilon^{-1} \nabla \times \sqrt{\mu^{-1}} - \omega^2 I \right) \tilde{\mathbf{H}} = \tilde{\mathbf{S}}. \quad (3.4)$$

To solve (3.4) directly, one can factorize the equation matrix

$$\mathcal{M} = \sqrt{\mu^{-1}} \nabla \times \epsilon^{-1} \nabla \times \sqrt{\mu^{-1}} - \omega^2 I. \quad (3.5)$$

After (3.4) being solved for the normalized magnetic field  $\tilde{\mathbf{H}}$ , one can easily restore all the electromagnetic fields and other quantities, for example, the Poynting vector in order to calculate reflection and transmission energy coefficients.

### 3.1.2 Eigenmode analysis

Omitting the current source term in Maxwell's curl equations (3.1a) we have

$$\nabla \times \mathbf{E} = i\omega\mu\mathbf{H} \quad (3.6a)$$

$$\nabla \times \mathbf{H} = -i\omega\epsilon\mathbf{E}. \quad (3.6b)$$

Again, already at this stage this Maxwell's system can be seen as an eigenproblem in  $\omega$  and the 'joint' field  $(\mathbf{E}, \mathbf{H})^T$ :

$$\begin{bmatrix} 0 & -\frac{1}{i\epsilon} \nabla \times \\ \frac{1}{i\mu} \nabla \times & 0 \end{bmatrix} \begin{bmatrix} \mathbf{E} \\ \mathbf{H} \end{bmatrix} = \omega \begin{bmatrix} \mathbf{E} \\ \mathbf{H} \end{bmatrix}. \quad (3.7)$$

This is not a good setting for further numerical solving however, because although the eigenmatrix in (3.7) is certainly very sparse, its dimensionality can be halved by combining (3.6a) and (3.6b) into the system of second-order differential equations, for example

$$\mu^{-1} \nabla \times \epsilon^{-1} \nabla \times \mathbf{H} = \omega^2 \mathbf{H}. \quad (3.8)$$

This can be further symmetrized upon the substitution  $\tilde{\mathbf{H}} \equiv \sqrt{\mu} \mathbf{H}$ :

$$\sqrt{\mu^{-1}} \nabla \times \epsilon^{-1} \nabla \times \sqrt{\mu^{-1}} \tilde{\mathbf{H}} = \omega^2 \tilde{\mathbf{H}}. \quad (3.9)$$

Although the eigenmatrix in (3.9) differs from  $\mathcal{M}$  (3.5), if we resort to the shift-and-invert method to solve the eigenproblem (3.9) iteratively for only a few frequencies around some target frequency  $\omega_{tgt}$  then we need, again, the recipe to calculate  $\mathcal{M} \setminus \mathbf{H}$  repeatedly during the iteration process. The way which is robust and fast (but memory consuming) is to factorize  $\mathcal{M} = LU$  — that is, to do exactly the same step which we can employ for solving (3.4) in the monochromatic wave propagation modeling.

Due to the presence of the PMLs the eigenmatrix  $\Theta = \sqrt{\mu^{-1}} \nabla \times \epsilon^{-1} \nabla \times \sqrt{\mu^{-1}}$  in (3.9) is complex nonhermitian even if the constitutive materials are non-absorptive. Such nonhermitian problem leads to complex eigenfrequencies  $\omega = \omega' + i\omega''$  with their real parts giving the resonance frequencies and the imaginary parts directly connected to the  $Q$ -factors:

$$\omega_0 = \omega', \quad Q = \frac{\omega'}{2\omega''}. \quad (3.10)$$

For a sufficiently good resonator we always have  $\omega' \gg \omega''$ , so that in numerical modeling, comparable absolute errors in  $\omega'$  and  $\omega''$ ,  $\delta\omega' \approx \delta\omega''$ , lead to much higher relative errors in the  $Q$ -factor values:  $\delta\omega'/\omega' \ll \delta\omega''/\omega''$ . This is exactly what we will see in the numeric examples below. Furthermore, the  $Q$ -factor is more sensitive to the PML parameters (their placement, absorption profile, etc.) as it arises entirely due to the introduction of artificial imaginary parts in  $\epsilon$  and  $\mu$  within the PMLs, while for the eigenwavelength the PMLs can be seen as just a perturbation.

Additional complication arises through the frequency dependence of material tensors  $\epsilon$  and/or  $\mu$  and hence the eigenmatrix  $\Theta$ . When resonator contains metal components or any other materials whose dispersion should accurately be taken into account, one can start with some guess  $\omega_0$  for the eigenfrequency and attempt repetitive solving of the linearized eigenproblem with  $\Theta = \Theta(\omega_0)$

for the eigenfrequency  $\omega_1$ , then with  $\Theta = \Theta(\omega_1)$  for  $\omega_2$  etc., until a convergence criterion  $|\omega_i - \omega_{i-1}| < \Delta\omega$  is met. But, unlike material dispersion, the PML dispersion is a mathematical artifact inessential to the user of a numerical tool and, due to certain robustness of PML performance with respect to the values of PML conductivity, the PML dispersion can be ignored in the frequency domain by putting  $\Theta = \Theta(\omega_0)$  in the eigenproblem. If this  $\omega_0$  used to define the PML maximum conductivity is not too far from the exact eigenfrequency, one can expect that an error introduced by non-optimal PML conductivity is negligible.

## 3.2 Discretization matters

### 3.2.1 Discretization of computational domain interior

In the discretized form Eq. (3.9) reads

$$\begin{aligned} \omega^2 \begin{bmatrix} \tilde{H}_x \\ \tilde{H}_y \\ \tilde{H}_z \end{bmatrix} &= \sqrt{\mu^{-1}} \begin{bmatrix} 0 & -\mathcal{F}_z & \mathcal{F}_y \\ \mathcal{F}_z & 0 & -\mathcal{F}_x \\ -\mathcal{F}_y & \mathcal{F}_x & 0 \end{bmatrix} \epsilon^{-1} \\ &\times \begin{bmatrix} 0 & -\mathcal{B}_z & \mathcal{B}_y \\ \mathcal{B}_z & 0 & -\mathcal{B}_x \\ -\mathcal{B}_y & \mathcal{B}_x & 0 \end{bmatrix} \sqrt{\mu^{-1}} \begin{bmatrix} \tilde{H}_x \\ \tilde{H}_y \\ \tilde{H}_z \end{bmatrix} \end{aligned} \quad (3.11)$$

where  $\tilde{H}_{x,y,z}$  are column-vectors of length  $n_{\text{tot}}$  each,  $n_{\text{tot}} = n_x n_y n_z$  is the total number of grid nodes in the domain. It is assumed that  $\mu$  is represented by a diagonal matrix (which is not always true for  $\epsilon$  upon its polarization-sensitive averaging at material boundaries, see Ref. [145]) so that  $\mu^{-1}$  can be split in its square roots trivially in order to get symmetrized eigenmatrix  $\Theta = \sqrt{\mu^{-1}} \nabla \times \epsilon^{-1} \nabla \times \sqrt{\mu^{-1}}$ . We define 1D forward difference matrix  $f_{n_x}$  of size  $n_x \times n_x$  acting along  $x$  on the electric field component normal to  $x$ , for example  $E_y$ :

$$f_{n_x} \begin{bmatrix} E_y^1 \\ \vdots \\ E_y^{n_x-1} \\ E_y^{n_x} \end{bmatrix} = \frac{1}{\Delta x} \begin{bmatrix} -1 & 1 & & \\ & \ddots & \ddots & \\ & & -1 & 1 \\ & & & -1 \end{bmatrix} \begin{bmatrix} E_y^1 \\ \vdots \\ E_y^{n_x-1} \\ E_y^{n_x} \end{bmatrix} \quad (3.12)$$

with  $\Delta x$  being the grid step (which is constant in computational space but may vary in physical coordinates). The matrices  $\mathcal{F}_{x,y,z}$  of the size  $n_{\text{tot}} \times n_{\text{tot}}$  are:

$$\begin{aligned} \mathcal{F}_x &= I_{n_z} \otimes I_{n_y} \otimes f_{n_x}, \\ \mathcal{F}_y &= I_{n_z} \otimes f_{n_y} \otimes I_{n_x}, \\ \mathcal{F}_z &= f_{n_z} \otimes I_{n_y} \otimes I_{n_x}, \end{aligned} \quad (3.13)$$

where  $I_{n_j}$  is the unit diagonal matrix of the size  $n_j \times n_j$ ,  $\otimes$  is the Kronecker product. Backward-difference matrices  $\mathcal{B}_{x,y,z}$  are equal to the negative  $\mathcal{F}_{x,y,z}$  transposed. Thus, the final size of the eigenvalue matrix  $\Theta$  is  $3n_{\text{tot}} \times 3n_{\text{tot}}$ . The combination of forward and backward differentials acting on the Yee-staggered electric and magnetic fields allows second-order-accurate discretization of (3.9), at least locally. Numerical accuracy of the FDFD solution for various Cartesian discretization meshes was analyzed by Smith [146, 147]; in particular, different offsets in location of field components within the primary cell were discussed with conclusion that the most accurate is the classical Yee staggering [120]. Besides, Smith showed that the deviation of numerically determined wavenumbers from analytic ones is small only far below the Nyquist wavenumbers. That is, the roughest sampling should be at least  $\lambda/10$  to get reliable simulation results.

The chosen arrangement of electric and magnetic field components assumes placing of the perfect magnetic conductor (PMC) boundary at the beginning and the perfect electric conductor (PEC) boundary at the end of each of the domain extensions, as shown in Fig. 3.1. This is very convenient in modeling open symmetric systems: by centering such system in an appropriate corner of computational domain, we cut the system by a combination of the PMC and PEC planes according to the expected mode symmetry while covering three

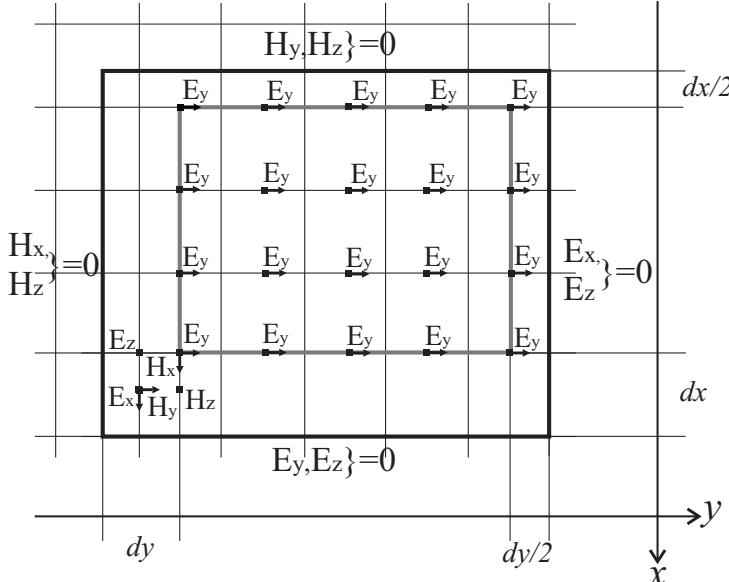


Figure 3.1:  $xy$ -cut of the Yee mesh with locations of the  $E_y$  nodes shown relative to the computational domain boundaries (depicted with bold black lines). The meshes for other components are obtained through linear shifts by half cell steps along the different coordinate axes.

remaining domain walls with absorbing boundary layers.

Figure 3.1 is a guide for understanding how the field component grids are located inside the computational domain with respect to each other and the domain boundaries. We see that the gray frame representing the starting and ending planes of the nonzero  $E_y$  components grid has dimensions that do not coincide with the real domain size but are smaller. Shifts of this gray frame with  $E_y$  pixels by half or whole grid step size along different axes give meshes for all other field components with the same total number of nodes in the result. Note that Maxwell's equations are local, i.e. they connect only the neighboring electric and magnetic field components; hence to reduce the bandwidth of the eigenmatrix it can be defined such that the field components are arranged as  $[E_{x_{111}}, E_{y_{111}}, E_{z_{111}}, E_{x_{211}}, E_{y_{211}}, E_{z_{211}}, \dots]^T$  instead of  $[E_{x_{111}}, E_{x_{211}}, \dots, E_{y_{111}}, E_{y_{211}}, \dots, E_{z_{111}}, E_{z_{211}}, \dots]^T$ . The former case leads to a significant decrease of the matrix bandwidth and, hence, to much lesser memory requirements when performing LU factorization.

In Appendix B we compare the FDFD and FEM efficiencies for solution of Helmholtz equation for rectangular 2D PEC cavity. The sampling and size of the cavity were kept the same for both methods. In general, the FDFD technique has performance comparable with the FEM method what makes much simpler FDFD structured formulation perspective. Of course, this is just an initial estimation and detailed comparison is needed for more complicated geometries and boundary settings.

### Non-equidistant mesh

Non-equidistant grid can be introduced if transformation function  $f(x_{\text{comp}})$  from computational  $x_{\text{comp}}$  to physical  $x_{\text{phys}}$  coordinates is known:

$$x_{\text{phys}} = f(x_{\text{comp}}) \quad (3.14)$$

Discretization of the domain is first done in computational coordinates to obtain strictly equidistant mesh and then physical mesh nodes are calculated. Physical mesh is defined in any orthogonal system of coordinates, i.e. cartesian, spherical, cylindrical, etc. An example of algorithm to incorporate non-equidistant physical grid within the logically cartesian code may look like:

1. Find domain size in computational coordinates,  $x_{\text{comp}}^{\text{end}}$ , by solving Eq. 3.14 for  $x_{\text{comp}}$ :  $x_{\text{comp}}^{\text{end}} = f^{-1}(x_{\text{phys}}^{\text{end}})$
2. Discretize the domain in computational coordinates with equidistant grid and find the corresponding physical mesh node coordinates through Eq. 3.14
3. In physical non-equidistant orthogonal coordinates do the permittivity averaging at material boundaries
4. Using the jacobian  $[J] = \frac{\partial x_{\text{comp}}}{\partial x_{\text{phys}}} = \frac{1}{f'(x_{\text{comp}})}$  and Eq. 1.23 (with substitution  $x' \rightarrow x_{\text{comp}}$ ,  $x \rightarrow x_{\text{phys}}$ ) compute  $\epsilon_{\text{comp}}$  and  $\mu_{\text{comp}}$

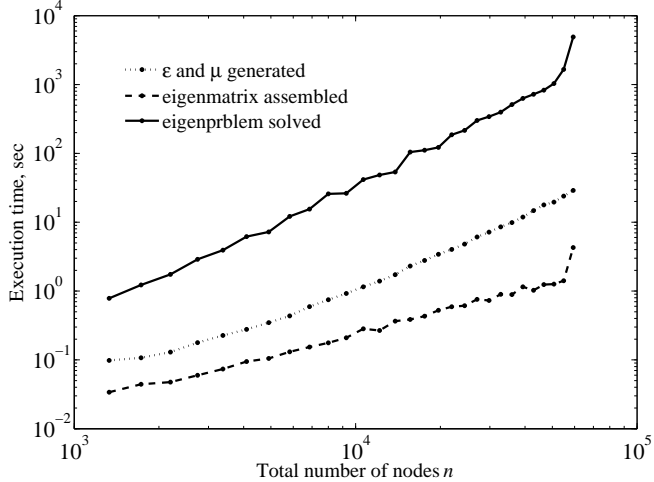


Figure 3.2: Execution time of three major FDFD algorithm blocks: (i) generation of  $\epsilon$  and  $\mu$  arrays representing material distribution within the domain and, if necessary, PMLs and STLs; (ii) assembling sparse eigenmatrix to be solved; (iii) solving the eigenmatrix with Matlab’s `eigs` function. Simulations were performed on a 16 Gb station for the dipole mode in the spherical resonator from Section 2.2.2.

5. After the FDFD run, physical field components  $F_{phys}$  are found as  $F_{phys} = [J]F_{comp}$

Notice that  $f(x_{comp})$  is usually a nonlinear function and deriving explicit analytic expression for the inverse,  $f^{-1}(x_{phys}) = x_{comp}$ , is often impossible. Thus in the first stage listed above, to find  $x_{phys}$  from the given  $x_{comp}$ , transcendental Eq. 3.14 is typically solved. This might be computationally and time demanding and it is preferable to do it only for a few nodes, not the whole mesh. This is also the reason why we start by specifying analytic form of  $f(x_{comp})$  but not  $f^{-1}(x_{phys})$  because in the latter case transcendental equation should be solved for all mesh nodes to calculate physical coordinates.

### Time consumption

Time consumption given by discretization and simulation of a square domain on a 16 Gb machine is shown in Fig. 3.2 on the example of the dipole mode in the spherical resonator (exact parameters can be found in Section 2.2.2). Generating permittivity and permeability arrays and construction of a total eigenvalue matrix normally takes seconds or minutes at most. The eigenmatrix assembly time is linear with  $n_{tot} = n_x n_y n_z$  while the  $\epsilon$  array generation time scales in 3D as linear measure squared,  $n_{tot}^{2/3}$ , because its major overhead is treating

grid cells crossed by material boundaries. We pass the assembled eigenmatrix to the Matlab function `eigs` which provides an interface to the Fortran-based ARPACK [148] library for solving sparse eigenvalue problems iteratively; however, we use direct LU factorization at the shift-and-invert step. This is much more memory-consuming but also more reliable and universal than iterative algebraic methods which require very careful and problem-dependent preconditioning. The solution time and the maximal resolution for the given memory limit depend strongly on the structure of the eigenmatrix. Thus, elongated cavities give eigenmatrices with much smaller bandwidth and hence essentially larger maximal total number of grid nodes  $n_{\text{tot}}$  than structures requiring a cubic domain. Characteristic run time in 3D modeling is about an hour or two if you are close to the memory limit on a 16 Gb machine.

### 3.2.2 Boundary conditions and domain reduction

#### Zero boundaries

The chosen arrangement of electric and magnetic field components assumes placing of the perfect magnetic conductor (PMC) boundary at the beginning and the perfect electric conductor (PEC) boundary at the end of each of the domain extensions, as shown in Fig. 3.1. Expressions for the elementary forward and backward differentials:

$$f = \frac{1}{\Delta h} \begin{bmatrix} -1 & 1 & & \\ & \ddots & & \\ & & -1 & 1 \\ & & & -1 \end{bmatrix}, \quad b = \frac{1}{\Delta h} \begin{bmatrix} 1 & & & \\ -1 & 1 & & \\ & & \ddots & \\ & & & -1 & 1 \end{bmatrix} \quad (3.15)$$

show that we get zero values at the interfaces of the computational domain for some field components. For example, the last row in the matrix  $f_{n_x}$  gives differential of the electric field at the end point proportional to  $0 - E_y^{n_x}$  implying the  $y$ -directed electric field component vanishes at the  $n_x + 1$  point. Thus in all Yee-mesh cells located at the  $n_x + 1$  plane we have a perfect electric conductor (PEC) boundary with nullified tangential components  $E_y = 0, E_z = 0$ . If we are going to consider this PEC boundary as a plane of symmetry then at the  $x = n_x + 1$  plane the tangential electric and normal magnetic components have zero values; all the rest normal electric and tangential magnetic components preserve the same values as at the  $x = n_x$  plane, being symmetrically reflected at the PEC-boundary. For the virtual  $x = n_x + 2$  plane we have negative reflection for all antisymmetric components, and positive reflection for the symmetric ones.

From Eqs. (3.12) we see that the forward curl operator  $\nabla_e$  acting on the electric field leads to absence of its tangential components at the top borders of the domain, that is the upper and the most right planes in Fig. 2.1b, Fig. 3.1. Corresponding PEC boundary condition planes are shown schematically in the figure. The curl operator  $\nabla_h$  acting on magnetic field is composed from backward differences matrices  $V_{x,y,z}$ . The latter nullify magnetic tangential compo-

nents at the bottom plane interfaces passing through the origin of the domain, i.e. most left and bottom borders, see Fig. 2.1b and Fig. 3.1. The perfect magnetic conductor (PMC) boundary conditions are also depicted there. This automatical fulfilment of boundary conditions without additional changes in eigenmatrix is very convenient also for memory savings as we in general do not take into account nodes lying at the edges of the domain.

The position of PEC and PMC planes are directly connected with our formulation of finite-differences matrices and it is important that numbering of all arrays should start from the bottom left corner and finish in the top right corner. This rule should be followed while discretizing structure to get  $\epsilon$  and  $\mu$  profiles.

### Domain reduction with PEC and PMC planes

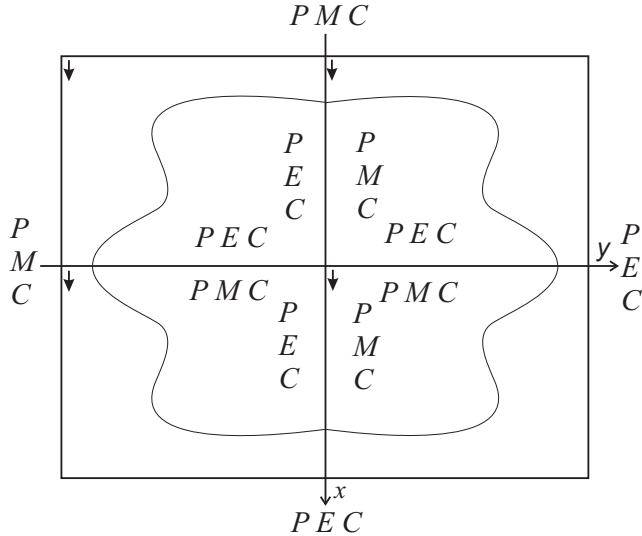


Figure 3.3: Boundary conditions arising from reduction of the domain showed in  $xy$ -cut. Arrows in the corners indicate points to start indexing.

Most of the optical systems used as resonators have symmetrical form, therefore it is computationally favorable to discretize not a whole domain but only its part thus increasing maximum possible resolution at least twice. The alternating boundary conditions surrounding the domain in Fig. 3.1 turn out to be very convenient, when we want to exploit planes of symmetry. Indeed, we do not need to put any additional efforts to implement PEC or PMC conditions in the code. Just by discretization different pieces of symmetric systems while covering remaining domain walls with absorbing boundary layers, we can consider optical structures with various number of mirror-symmetrical planes and

solve the eigenvalue problem for modes with diverse symmetries.

If an origin of coordinates coincides with the center of symmetry of a resonator the easiest way to make domain reduction within the same code is to consider only positive or negative half-axis for each coordinate thus allowing PEC or PMC planes to cut away unnecessary symmetric parts of the structure. It is illustrated in Fig. 3.3 on the example of  $x - y$  plane passing through the center of computational domain. Thus, for objects with three perpendicular planes of symmetry we specify only one of the eight coordinate octants to be sampled and simulated.

### Periodic boundaries

Treatment of structures with periodicity is one of the essential advantages of the frequency domain technique. Bloch periodicity along some axis  $x$ :  $H(x + P) = e^{ik_x P} H(x)$ , where  $k_x$  is the wave vector, can be incorporated into 1D differential by substituting zeros in Eq. 3.15:

$$f = \frac{1}{\Delta h} \begin{bmatrix} -1 & 1 & & \\ & \ddots & & \\ & & -1 & 1 \\ \boxed{e^{ikP}} & & & -1 \end{bmatrix}, \quad b = \frac{1}{\Delta h} \begin{bmatrix} 1 & & & \boxed{-e^{-ikP}} \\ -1 & 1 & & \\ & \ddots & & \\ & & -1 & 1 \end{bmatrix}, \quad (3.16)$$

Note, that for periodic boundaries discretization scheme in Fig. 3.1 is not suitable. In particular, the boundaries of computational domain should coincide with mesh nodes for one of the field components to enforce strictly periodic boundary conditions, i.e. half Yee cell offset is not required.

### Open boundaries

Construction of efficient absorbing boundaries for modeling open photonic systems is not a trivial task. Profound research was done on optimizing the PMLs — their thickness, conductivity profile, and frequency dispersion — for better absorption of oscillatory waves. In many real-life simulations however, one deals routinely with an admixture of evanescent field spreading from a photonic structure; it is this evanescent field that prevents PMLs be constructed starting immediately from the boundaries of the structure. This is bad news since increased computation domain size amounts to increased computer memory consumption, especially in 3D modeling. To squeeze the buffer physical space into the interval  $[a_0, b]$  (where  $a_0$  is the most extended point of the modeled object and  $b$  the computational domain boundary) most efficiently, we combine standard PMLs with free space mapping, so that the wavelength-dependent buffer “stretch function” in  $x$  (and similarly  $y$  and  $z$ ) direction is

$$s(x_{\text{comp}}, \lambda) = \zeta(x_{\text{comp}}) - i\sigma_{\max}(\lambda) \eta(x_{\text{comp}}). \quad (3.17)$$

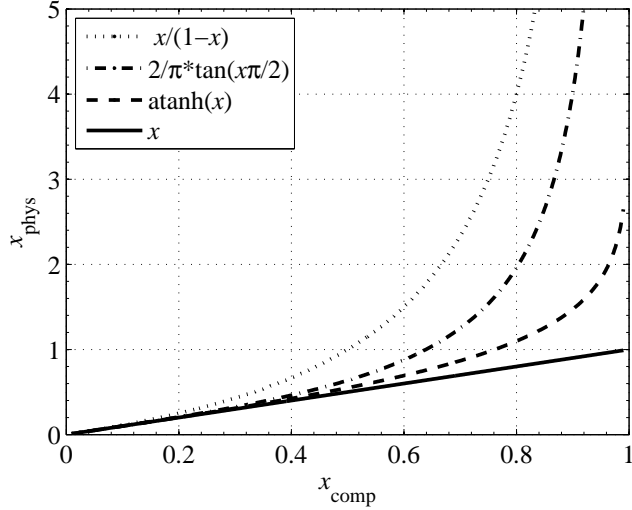


Figure 3.4: Examples of the mapping function  $x_{\text{phys}} = x_{\text{phys}}(x_{\text{comp}})$  compared to the identity line  $x_{\text{phys}} = x_{\text{comp}}$  (plotted in bold).

Here  $\zeta(x_{\text{comp}}) = \partial x_{\text{comp}} / \partial x_{\text{phys}}$  is the derivative of the chosen real space squeezing function; the normalized maximum conductivity

$$\sigma_{\max}(\lambda) = R \frac{p+1}{4\pi} \frac{\lambda}{b - a_1}, \quad (3.18)$$

where the PML starts from the coordinate  $x_{\text{comp}} = a_1 > a_0$ , the logarithmic damping  $R$  by an idealized (continuous) PML can be taken equal to 20, and  $\lambda$  is the wavelength; the conductivity profile function  $\eta(x_{\text{comp}})$  is zero everywhere except inside the PML,  $a_1 < |x_{\text{comp}}| < b$ :

$$\eta(x_{\text{comp}}) = \left( \frac{|x_{\text{comp}}| - a_1}{b - a_1} \right)^p, \quad (3.19)$$

where  $p$  is the PML conductivity profile order, 2 being a common choice. We found that the choice of a space squeezing function (see Fig. 3.4 for a few examples) does matter in real life simulations; we stick to the  $x_{\text{phys}} = x_{\text{comp}}/(1 - x_{\text{comp}})$  function which allows to represent on a give computational coordinate interval  $[0, x_{\text{comp}}]$  a considerably wider physical interval  $[0, x_{\text{phys}}]$ : for example,  $0.5_{\text{comp}}$  translates to  $1.0_{\text{phys}}$ , which means that if the PMLs cover half of the squeezed free space buffer in computational space, the actual “physical” distance between the PMLs and the modeled object is double that. More precisely, our mapping function is  $x_{\text{phys}} = x_{\text{comp}}$  on  $|x_{\text{comp}}| < a_0$  while on

$$a_0 < |x_{\text{comp}}| < b$$

$$x_{\text{phys}} = \frac{x_{\text{comp}}}{|x_{\text{comp}}|} \left[ a_0 + (b - a_0) \frac{|x_{\text{comp}}| - a_0}{b - |x_{\text{comp}}|} \right] \quad (3.20)$$

and thus in (3.17) we put

$$\zeta(x_{\text{comp}}) = \frac{(b - |x_{\text{comp}}|)^2}{(b - a_0)^2} \quad (3.21)$$

for  $a_0 < |x_{\text{comp}}| < b$  and 1 otherwise. A steeper mapping function might be not a good option however, since upon discretization with equidistant steps in the computational domain space, the physical coordinates rapidly become too poorly sampled to represent outcoming oscillatory waves adequately.

### 3.3 Modeling of a sphere

#### 3.3.1 Adjusting parameters

In this Section 3.3.1 we will consider the same dipole mode in the sphere as in Section 2.2.2. To find an optimal width of the PMLs as well as to estimate the minimal admissible sphere-to-PMLs distance, we analyzed how the relative errors in  $Q$  and  $\lambda$  change with variation of these parameters.

##### Sensitivity to the PML width

Fig. 3.5 shows the FDFD algorithm convergence in the case of a very small sphere-to-PMLs distance of 4 grid points. Surprisingly but even at the both PMLs and spehere-to-PMLs lengths as small as 4 grid cells we get admissible mistake of 4% only. higher  $Q$  bigger air distance should be chosen for correct modeling.

In Fig. 3.5 for all considered resolutions the relative error in  $Q$  is less than 0.5% starting from the PMLs of at least 5 grid points in thickness. So 5 grid points is a threshold value, after which accuracy of  $Q$  calculation becomes much better for the dipole mode in the sphere. The thinner PMLs do not absorb outgoing radiation efficiently.

The insert in Fig. 3.5 represents precision of the resonance wavelength calculation with the air layer as thin as 4 grid cells. Refinement of the grid greatly minimizes the relative  $\lambda$  error, while the PMLs extension reveals no significant improvement. Similar figures plotted for the air increment (from 4 to 8 voxels also nearly does not change the dependencies depicted in Fig. 3.5: the axis range for  $\lambda$  error remains the same, bounded by the maximum value of 0.3%. An interesting conclusion arises here. For this example of a sphere, precision of the resonance wavelength calculation depends mostly on sampling, hence the domain size should be kept reasonably small to lessen the  $\lambda$  error due to good discretization.

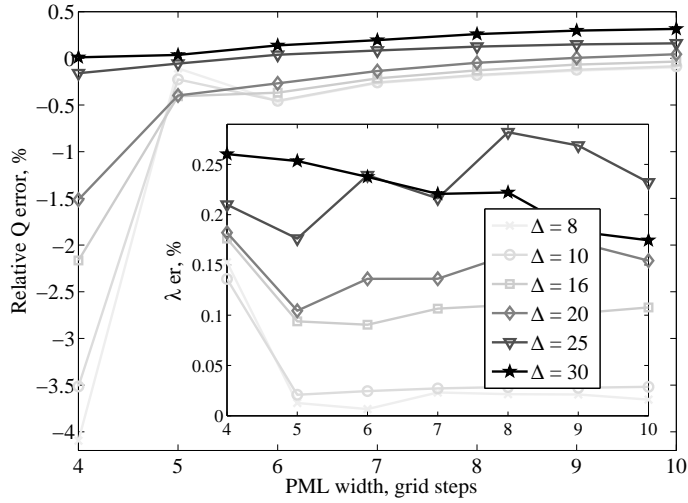


Figure 3.5: The relative  $Q$  and  $\lambda$  error with increase of the PMLs width for various cubic grid step size  $\Delta$  listed in the legend in nm. Simulations are done for the dipole mode in the sphere from Section 2.2.2 with the sphere-to-PMLs distance being 4 grid points everywhere.

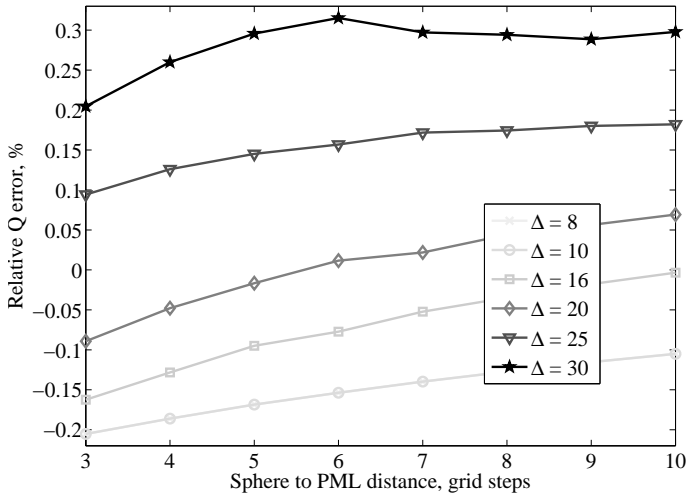


Figure 3.6: The relative  $Q$  and  $\lambda$  error versus sphere-to-PMLs distance for various samplings  $\Delta$  in nm. Simulations are done for the dipole mode in the sphere from Section 2.2.2 with the PML width being 8 grid cells everywhere.

### Sensitivity to the sphere-to-PML distance

An attempt to look at the problem from another angle is to vary the sphere-to-PML distance while keeping the PML width fixed. As an example we plot here Fig. 3.6 where PMLs are 8-cell thick. All curves are slowly varying functions without any threshold.

As it should be expected from previous discussion, starting from 5-cell thick PMLs, an error for all considered resolutions is lowered, what is reflected in Table 3.1. The second row represents the approximate  $\lambda$ -error spread given by six samplings. For PMLs thicker than 5 cells, the upper bound error does not exceed the positive value of 0.3%. In other words, for rough resolution the relative error almost does not minimize with the air or PMLs prolongation.

An approach to the analytic  $Q$  from the opposite, negative relative errors side, is much faster and corresponds to the smallest voxel size. This reduction of the negative error absolute value is reflected in the second row of Table 3.1 characterizing FDFD performance for different PML sizes. Thus, overall, the  $Q$  error diminishes due to three factors: resolution improvement and enlargement of the number of grid cells for both the air and PMLs regions. The slopes of curves in Figs. 3.5 and 3.6 are very similar, so the best way to plot convergence curve is to fix domain size in physical units and improve resolution.

A virtual independence of  $\lambda$  error on the PML width looks pretty much as in insert in Fig. 3.5, so all conclusions here remain the same. This behavior — when the accuracy of the eigenwavelength evaluation depends primarily on object sampling with no change while lengthening buffer layer — will be also noticed in the analysis of other cavities.

### Adjusting parameters: Optimal domain size

PMLs size, grid cells	4	5	6	8	10
$Q$ error range, %	$-4.5 \div 0.5$	$-0.5 \div 0.3$	$-0.5 \div 0.3$	$-0.2 \div 0.3$	$-0.1 \div 0.3$
cell size giving 0 $Q$ er., nm	30	25	$25 \div 20$	20	16

Table 3.1: From analysis of Figs. similar to Fig. 3.6 with other PML width.

The analysis of Figs. 3.5 and 3.6 shows that for the different configurations of a computational domain, that is, the air and PMLs thicknesses and the resolution, we get either positive or negative error in  $Q$ . This behavior agrees with oscillating type of convergence usually obtained in  $Q$ ,  $\lambda$  vs discretization plots. The last row in Table 3.1 gives the cell size providing the smallest  $Q$  error for the given PML buffers. With decrease of the grid cell size more cells

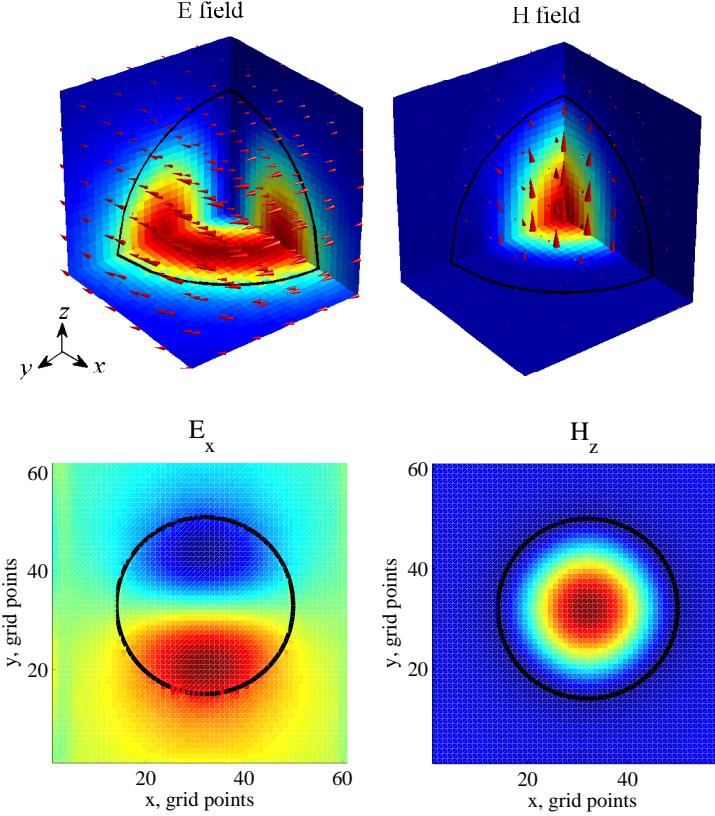


Figure 3.7: (Color online) Electric and magnetic vector field distributions of the TE<sub>101</sub> (“TE<sub>1</sub>”) mode in an octant of the sphere (above), and  $z = 0$  cuts of the  $E_x$  and  $H_z$  components restored over the extended domain (below).

should be added to PMLs, what means keeping the domain size the same in physical units.

We conclude that there exists an optimal minimal computational domain size for intermediate resolutions going above which does not improve simulation result essentially anymore. Thus there is no sense to choose too big domain, a favor should better be given to improvement of discretization at the domain size fixed around the optimal value.

### 3.3.2 Convergence studies

For the sphere of relatively high refractive index  $n = \sqrt{\epsilon} = 6$  in the air [145] we consider two lowest TE modes, a dipole one (we label it as TE<sub>1</sub>) having the

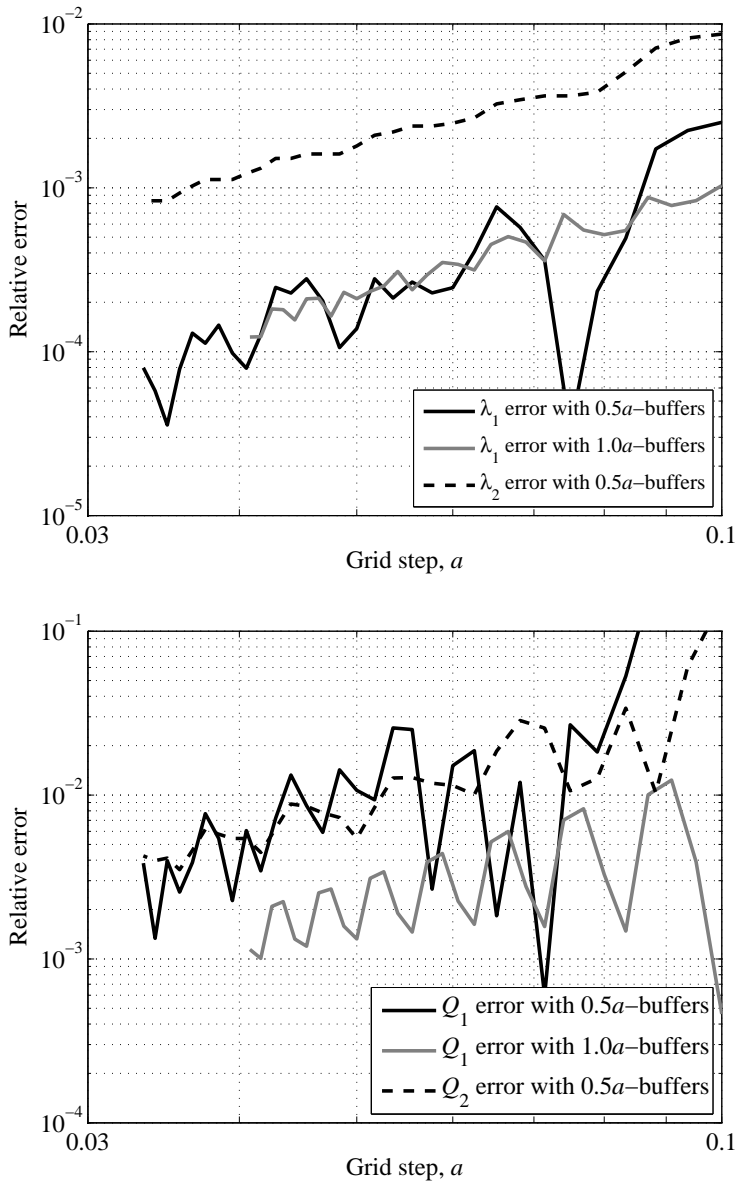


Figure 3.8: Relative errors in  $\lambda$  (above) and  $Q$  (below) for the TE<sub>1</sub> and TE<sub>2</sub> modes of a sphere of radius  $a$ , centered in the corner of a cubic computational domain of size  $1.5a$  or  $2.0a$ , thus giving the squeezed-space buffers of  $0.5a$  or  $1.0a$ , in computational coordinates. Half of each buffer layer is covered with the PML. The sphere is discretized uniformly:  $\Delta x = \Delta y = \Delta z$ .

eigenwavelength  $\lambda_1 = 12.270\,896\,a$  and the quality factor  $Q_1 = 43.168\,603$ , and the next one ( $TE_2$ ) with a comparable quality factor  $Q_2 = 35.1927$  but nearly twice smaller eigenwavelength  $\lambda_2 = 6.082\,110\,a$ . The boundary conditions corresponding to the symmetry of these modes are: one PMC and two PEC planes dissecting the sphere. The dipole mode is sketched in Fig. 3.7: the dominant components are  $E_x$ ,  $E_y$  and  $H_z$ , which corresponds to the TE polarization of this mode. We see that the electric field forms a toroid near the sphere border and the magnetic field flows round this toroid having its maximum at the very center of the resonator.

The convergence of numerically computed  $\lambda$  and  $Q$  to their analytic values is shown in Fig. 3.8. All the curves demonstrate second order convergence rate in  $\Delta x$ . In Ref. [145] it is shown that polarization sensitive averaging which is used in our calculations helps preserving second order accuracy of the FDFD algorithm what is not always true if simple staircasing is employed instead. As expected from  $\omega'/\omega'' \approx 86$  or 70 for the modes considered, the relative errors in  $\lambda$  are an order of magnitude lower than the relative  $Q$ -factor errors — note the difference in the  $y$ -scales in the upper and lower plots in the figure. From the upper plot we see that the  $\lambda_1$  values (black and gray curves) are largely insensitive to varying buffer thickness; this is what we generally observe for any modes and structures calculated with the FDFD method. At a grid resolution of 10 voxels per  $a$  ( $\Delta x/a = 0.1$ ) the relative  $\lambda_1$  error stays within 0.25% accuracy, while the  $\lambda_2$  error is just below 1%. The reason is that the resolution of 10 voxels per  $a$  amounts to the impressive 120 voxels per  $\lambda_1$  while it translates to around 60 voxels per  $\lambda_2$ . With the second-order method, this ratio of 120/60=2 would account for the four-times poorer results in both  $Q_2$  and  $\lambda_2$  numerical values than those we have for  $Q_1$  and  $\lambda_1$ .

From the lower plot in Fig. 3.8 we can see the effect of the computational domain size on the  $Q$ -factor accuracy. Note that the widths of squeezed-space buffer layers are given in computational coordinates, which are translated to the physical coordinates via Eq. (3.20) with  $a_0 = a$  and  $b = 1.5a$  or  $2a$ : thus, the sphere-to-PML distance with the narrower ( $0.5a_{\text{comp}}$ ) buffer is  $0.25a_{\text{comp}} = 0.5a_{\text{phys}}$ , and with the wider ( $1.0a_{\text{comp}}$ ) buffer it is  $0.5a_{\text{comp}} = 1.0a_{\text{phys}}$ . The difference between the two  $Q_1$  curves in the plot is huge: the narrower buffer is clearly inadequate for the  $TE_1$  mode  $Q$ -factor simulations, while the  $1.0a_{\text{phys}}$  sphere-to-PML distance is a good choice for the  $TE_1$  mode in a sense that further increasing this distance gives only marginal improvement to the  $Q_1$  accuracy, and the sphere-to-PML distance in excess of  $2.0a_{\text{phys}}$  makes no sense. For the  $TE_2$  mode the  $Q_2$  curve is already smooth for the sphere-to-PML distance of  $0.5a_{\text{phys}}$  (for which it is plotted) yet a safer choice appears to be  $1.0a_{\text{phys}}$ . Thus for both modes, the safe buffer size equals  $\lambda/n$ . By modeling spheres of other refractive indices we found that this  $\lambda/n$  rule holds quite generally for this geometry; in the following Chapter we will see that this rule is also helpful in modeling of an entirely different, PhC membrane based resonator.



## Chapter 4

# Ultra-high- $Q$ nanophotonic resonators

In Chapter 2 we illustrated some complications of the FDTD method in treatment of photonic resonators: its long computational time in some approaches, the need of postprocessing to extract the  $Q$ -factor, and finally, the necessity of single-mode excitation for the most reliable determination of the  $Q$ -factor through the analysis of energy density. In this chapter the FDFD method is used to handle nanophotonic cavities: a photonic-crystal (PhC) membrane-based resonator and an elongated PhC nanobeam cavity.

Dielectric nanobeams can serve as waveguides in integrated photonic structures offering the benefits of strong light localization. A photonic crystal nanobeam cavity created by perforating the waveguide with a row of holes reaches a  $Q$ -factor comparable to that of a photonic crystal membrane resonator while being much more compact and easier in fabrication [62]. Even for a nanobeam cavity in a low refractive index material like  $\text{SiO}_2$ , fairly high  $Q$ -factors of several thousands were measured experimentally [149]. Recently, all-optical logical switching [150] and quantum dot laser [60] have been demonstrated in nanobeam cavities.

The FDFD method is only at a very initial stage of employment for open resonator simulations, but it holds big promise owing to its convenience for optimization of the cavities in 2D and 3D; treatment of several spectrally close resonances within single run with finding all the mode parameters: field maps, wavelengths,  $Q$ -factors; possibility to analyze degenerate modes. In this chapter the accent is put on the practical aspects of the FDFD modeling of open PhC resonators. The important issues discussed are the minimal widths of the PMLs and squeezed-space buffer layers, and the use of non-equidistant meshes. It is shown that the method can give stable estimates of the  $Q$ -factor of membrane nanophotonic resonator on a personal laptop within ten minutes in 3D.

## 4.1 PhC membrane cavity

### 4.1.1 Equidistant mesh and arctanh squeezing function

Here we take a high- $Q$  PhC membrane cavity as a simulation object. Hot spots of fields in high- $Q$  resonators usually imply the presence of intensive evanescent fields. Squeeze-transform layers (STLs) are applied in all our simulations to compress the evanescent tails spreading from a PhC cavity to the air. The STLs, covering all the air and PMLs, together with symmetry domain reduction, help to partly mitigate the problem of numerically large eigenmatrix. An optimal size of these buffer STLs including the PMLs is around  $1a$ , where  $a$  is the PhC lattice constant. At the beginning let take hyperbolic arctangent  $\text{atanh}(x)$  for the STLs from Fig. 3.4. For this most placid stretching function the PMLs are chosen to cover  $1/3$  of the whole buffer what gives smoother  $Q$  convergence curves than, for example,  $1/2$ -wide PMLs. The typical for a PhC numerous interfaces between dielectric and air holes are again treated with the polarization-sensitive dielectric tensor averaging [145].

Consider a high- $Q$  PhC membrane cavity shown in Fig. 4.1a: in a slab of refractive index  $n = 3.4$ , thickness  $h = 0.5a$ , with the hexagonal array of air holes of diameter  $0.7a$  ( $a$  is the lattice constant), a defect is formed by excluding

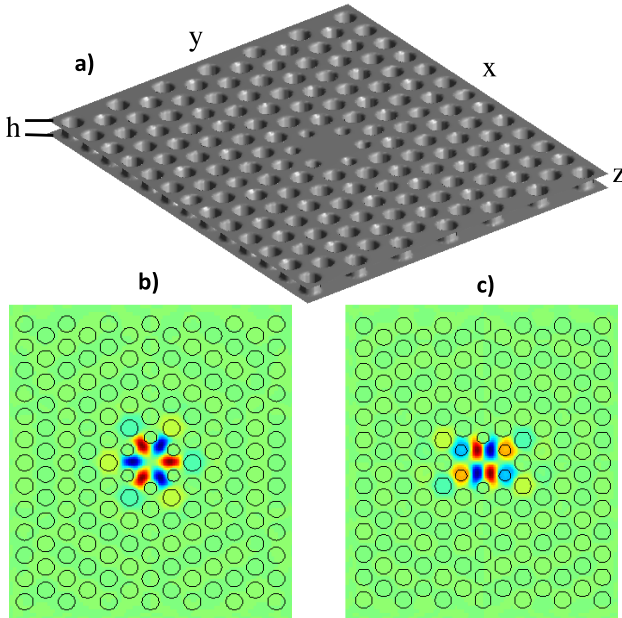


Figure 4.1: (a) A PhC membrane cavity. (b) The  $H_z$  field distribution of the hexapole mode. (c) The  $H_z$  field distribution of the quadrupole mode.

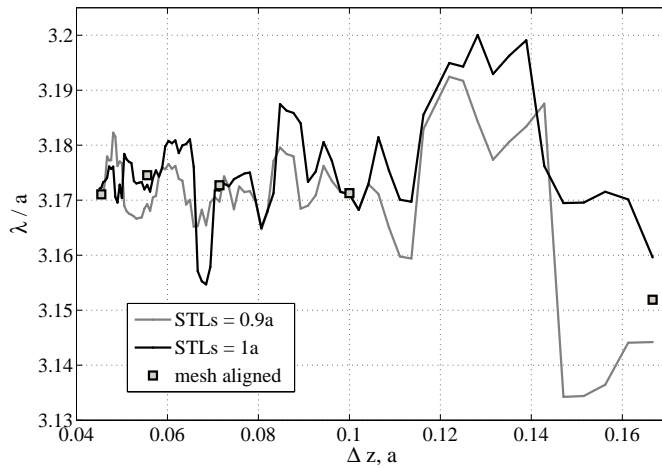


Figure 4.2: The resonance wavelength versus  $\Delta z$  for the narrower and wider domains. The PML width in  $x$  direction is 3 grid cells. The corresponding width of free-space buffer is shown in the legend. Bullets mark  $\lambda$ -values obtained with the nodes of  $H_z$  discretization mesh being aligned with flat membrane boundary.

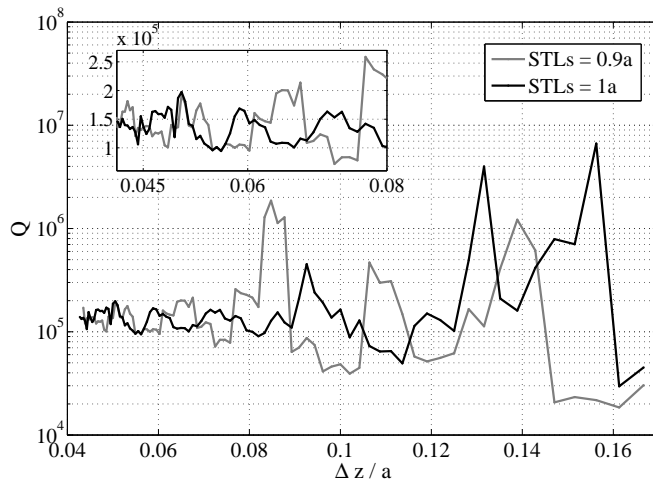


Figure 4.3: Same as Fig. 4.2 but for the  $Q$  factor convergence. The inset shows  $Q$  convergence on a linear scale.

one central hole and shifting the six holes next to it by  $0.1a$  from the center while shrinking their diameters by  $0.2a$ . The hexapole mode in this membrane cavity was reported having the quality factor  $Q = 1.68 \cdot 10^5$  and the wavelength  $\lambda = 3.1756 a$  [151]. Figure 4.1b represents standing wave pattern of this mode. For actual computations the structure can be cut though its center by the PEC wall at  $x = 0$ , and the PMC planes at  $y = 0$  and  $z = 0$ , so that an octant of what is shown in Fig. 4.1 has to be modeled.

From Fig. 4.2 we find that our calculations are consistent with the FDTD results [151], the discrepancy in  $\lambda$  being around 1%. The  $Q$  values lie between  $1 \cdot 10^5$  to  $2 \cdot 10^5$ , Fig. 4.3. For these plots cubic mesh for rough resolutions ( $\Delta z > 0.7a$ ) was used. Finer resolutions along  $z$  were attained by gradual stretching of grid cells, so that at the smallest  $\Delta z$  the grid along  $z$  becomes three times denser than in  $x$  and  $y$ ,  $\Delta x$  and  $\Delta y$  being approximately equal. The convergence for both  $Q$  and  $\lambda$  has an oscillating character and the PMLs of about 1/3 of these STLs demonstrate good performance. We also point out to a crucial role of the polarization sensitive dielectric tensor averaging in correct calculation of  $\lambda$  for the PhC membrane cavity.

#### 4.1.2 Non-equidistant mesh and $x/(1-x)$ squeezing

To resolve mode features better in the area of field hot spots while avoiding extra-fine sampling in low-intensity region, physically nonuniform mesh can be introduced. To retain mesh orthogonality, each direction should be resampled independently. We use the tanh function that allows building of plateaus of different but roughly equidistant meshing, connected through transition region with faster variation of sampling. With the ratio  $s$  between grid steps on the two plateaus, the width  $w$  and the center  $c$  of the transition region, the nonuniform grid step  $\Delta x'(x)$  as a function of grid coordinate  $x$  is defined via

$$\frac{\Delta x'}{\Delta x} = s + \frac{s-1}{2} \left[ \tanh\left(\frac{x-c}{w}\right) - \tanh\left(\frac{x+c}{w}\right) \right]. \quad (4.1)$$

At  $x = 0$  we have  $\Delta x' \simeq \Delta x$ , provided sufficiently narrow width  $w$  and sufficiently distant  $c$ . Physically nonuniform coordinates of grid nodes are

$$x' = \int_0^x \frac{\Delta x'}{\Delta x} dx = sx + \frac{s-1}{2} w \ln \left[ \frac{\cosh\left(\frac{x-c}{w}\right)}{\cosh\left(\frac{x+c}{w}\right)} \right]. \quad (4.2)$$

The black curves in Fig. 4.4 are plotted for stretch ratio  $s = 2$  in Eq. (4.1), i.e. the mesh is nearly twice coarser at the outskirts than in the center; the gray curves are for  $s = 3$ . Two sets of transition region parameters are considered:  $w = 2a$ ,  $c = 5a$  giving relatively slow transfer to a sparser mesh (solid curves); and  $w = 4a/3$ ,  $c = 4a$  with a faster jump to a coarser gridding (dotted curves) so that larger membrane area is covered with a rough mesh. Note that the grid metric information can be transferred to  $\epsilon$  and  $\mu$  via the standard

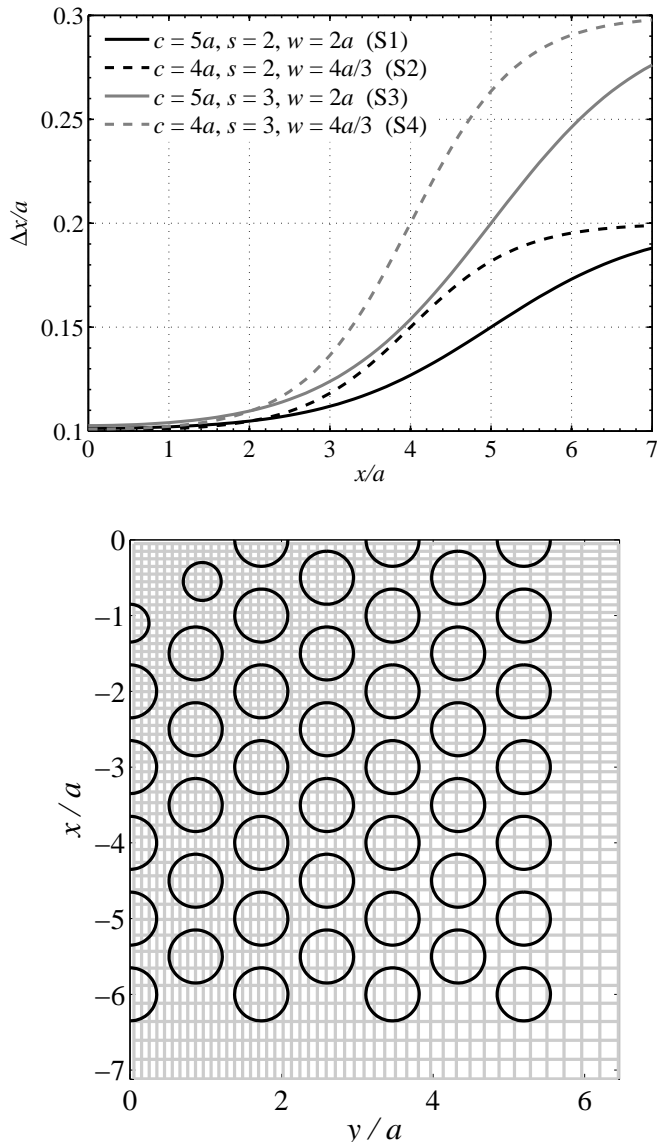


Figure 4.4: Above: Versions of Eq. (4.1) plotted for the start grid step  $\Delta x = 0.1a$ . Below:  $xy$  grid obtained via s4 stretch of  $x$  and  $y$ .

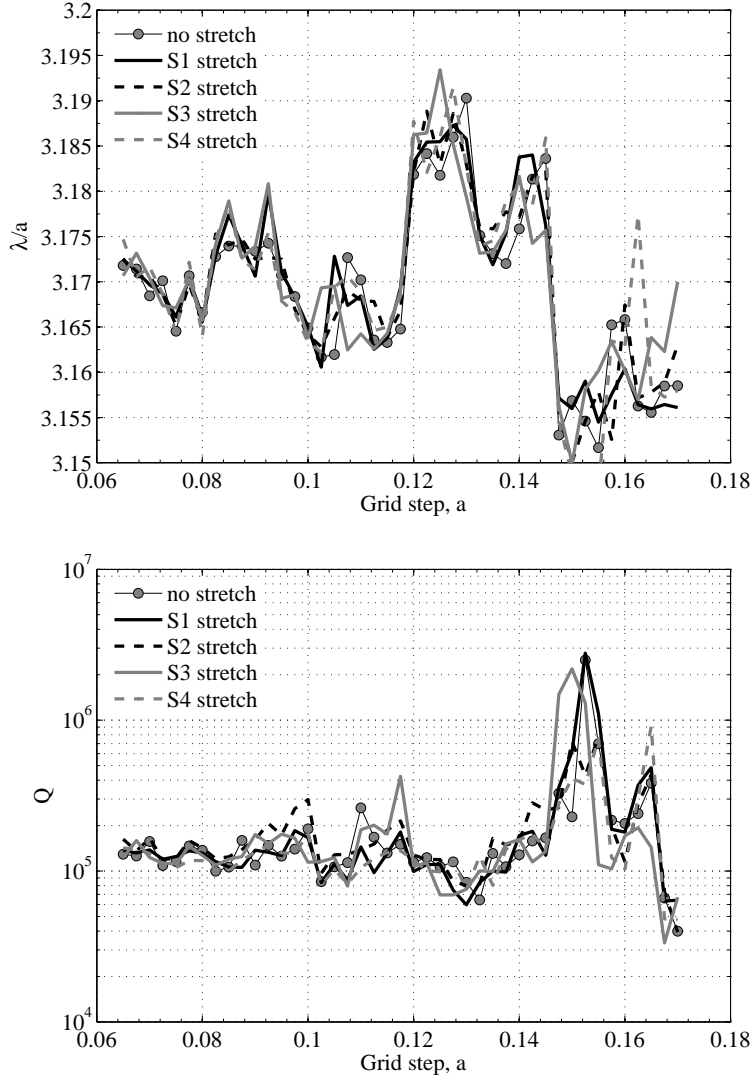


Figure 4.5: The eigenwavelength  $\lambda$  (upper plot) and quality factor  $Q$  (lower plot) of the hexapole mode versus computational grid step, calculated with 1.0a-wide squeezed-space buffer layers (half covered by PMLs). The PMLs in  $x$  and  $y$  directions extend over three grid cells. Solid black curves are obtained with the physically cubic grid ( $\Delta x = \Delta y = \Delta z$ ) while the other curves with nonuniform meshes in the  $xy$  plane like shown in Fig. 4.4.

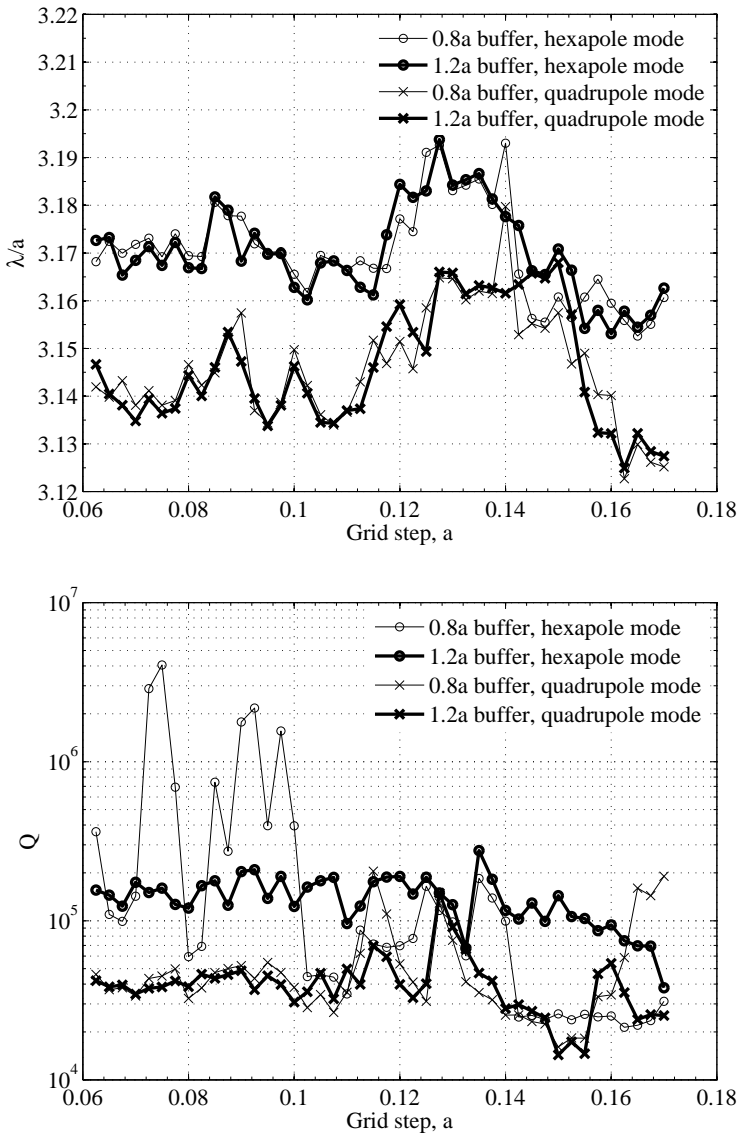


Figure 4.6: The eigenwavelength  $\lambda$  (upper plot) and quality factor  $Q$  (lower plot) of the hexapole mode (curves with circles) and quadrupole mode (curves with crosses) versus computational grid step, calculated with either  $0.8a$ - or  $1.2a$ -wide buffer layers in  $z$  (half covered by PMLs). The PMLs in  $x$  and  $y$  directions extend over three grid cells. All the results are obtained with nonuniform s4-stretched grid as shown in Fig. 4.4.

ideology of generally covariant electrodynamics, hence we can still use simple matrices (3.12),(3.13) for logically equidistant grid.

In Fig. 4.5 we see how  $\lambda$  and  $Q$  depend on the grid step size in the case of physically uniform grid ( $\Delta x = \Delta y = \Delta z$  everywhere within the membrane) compared to the grids stretched in  $x$  and  $y$  such that at the center  $\Delta x'$  and  $\Delta y'$  equal  $\Delta z$  but towards periphery they gradually increase as in Fig. 4.4. The values obtained are consistent with the FDTD results [151], provided the grid step is smaller than  $0.1a$  (thus the PMLs comprise 5 or more grid steps). Prominently, smooth non-equidistant discretization gives results very similar to those obtained on the uniform grid while the reduction in the total number of grid nodes  $n_{\text{tot}}$  is almost twofold for the s4 stretch. Thus, applying S4 function in  $x$  and  $y$  with  $\Delta z = 0.1a$  gives the total number of grid nodes  $n_{\text{tot}} \approx 3.0 \cdot 10^4$ , the eigenwavelength  $\lambda = 3.163a$  and the quality factor  $Q = 1.77 \cdot 10^5$ ; and the run time on a laptop with 4 Gb of RAM and 2.2 GHz CPU frequency is ten minutes. A slightly different function with  $c = 3a$  gives  $n_{\text{tot}} \approx 2.3 \cdot 10^4$ ,  $\lambda = 3.164a$  and  $Q = 1.59 \cdot 10^5$  in a two minutes run time.

In all these calculations we used  $a$ -thick squeezed-space buffer layer (half of which is covered by the PML) in  $z$  direction, in line with the proposed  $\lambda/n$  rule. To see how sensitive to the  $z$ -buffer thickness the results are, we chose a wider and a smaller domain and calculated the eigenwavelength (upper plot in Fig. 4.6) and  $Q$ -factor convergence (lower plot in Fig. 4.6) of the same hexapole mode and of the quadrupole mode reported having  $\lambda = 3.1456a$  and  $Q = 45\,000$  [151]. While  $\lambda$  curves are seen to be little affected by changing the domain size, there is a striking contrast between the  $Q$  curves of the hexapole mode calculated with  $1.2a$  and  $0.8a$  buffers, the latter giving clearly erroneous results. The quadrupole mode  $Q$ -factor is also problematic to define correctly at low resolution when using the  $0.8a$  buffers. On the other hand, if the buffer layers are thick enough, an order-of-magnitude accuracy in  $Q$  is achieved already at a very rough resolution of 8 grid points per  $a$ . Thus, as in the previous example of a sphere, the eigenwavelength accuracy is primarily limited here by the grid step while the  $Q$ -factor is mostly affected by the overall thickness of buffer layers no matter what the actual grid cell size is. Note that  $a$ -wide squeezed space buffers is a reasonable choice also for other modes of interest in this membrane, and generally for most PhC resonators who typically have band gaps with the defect modes around  $\lambda = na$ .

## 4.2 Nanobeam cavity

### 4.2.1 2D modeling: high- $Q$ design

At the beginning we tailor nanobeam cavity design in 2D to get high  $Q$  for the TE-mode. Fig. 4.7 shows basic nanobeam sketch used to consider various cavity designs: a nanowire of refractive index 3.4 is suspended in air and has 20 holes in its half. Fig. 4.7 also illustrates an example of sampling mesh with

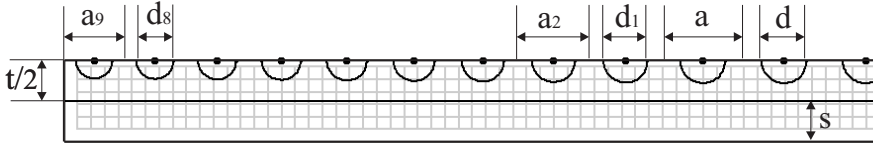


Figure 4.7: Part of nanobeam quarter with Hz component mesh location,  $x$ -direction is pointing along the nanobeam perforation,  $y$ -direction is along the nanobeam width.

	Design 1	Design 2	Design 3
Mirror: hole diameters	$d = 0.54a$	$d = 0.6a$	$d = 0.55a$
Defect: number of holes	$n = 1 \dots 9$	$n = 1 \dots 9$	$n = 1 \dots 9$
Defect: hole diameter	$d_n = \frac{d}{\sqrt[10]{n}}$	$d_n = 0.6a_n$	$d_n = d - 0.012na$
Defect: lattice constant	$a_n = \frac{d_n}{0.6}$ $a_1 = 0.8a$	$r_1 = \frac{1}{0.843a}, r_2 = \frac{1}{a}$ $a_n = \frac{1}{r_1 + \frac{r_2 - r_1}{9}n}$	$a_n = \frac{d_n}{0.6}$

Table 4.1: Different designs of the nanobeam cavity sketched in Fig. 4.7.

the half or whole grid step offset from computational domain boundaries in accordance with Fig. 3.3. In the reflecting part the lattice constant is  $a$  and the hole diameters are  $d$ , total width of a nanobeam  $t = 1a$ . In the defect region the modified hole diameters are  $d_n$  and the modified lattice constants are  $a_n$ , where  $n$  numbers a segment in the defect part of the cavity.

Intuitive variation of the defect region parameters — holes radii  $d_n$  and lattice constant  $a_n$  — in order to maximize  $Q$ -factor led us to the following conclusions. First of all, when both parameters are constant but differ from those in the reflecting part, the  $Q$ -factor can approach  $10^5$ . Second, if one of the parameters slowly decreases in the defect region towards the center,  $Q$  rises to  $10^6 \div 10^7$ . Third, only if both  $a_n$  and  $b_n$  gradually decrease from the periphery to the center of the cavity,  $Q$  reaches the highest value around  $10^8 \div 10^9$  in 2D. In 3D it is usually one to two orders of magnitude less.

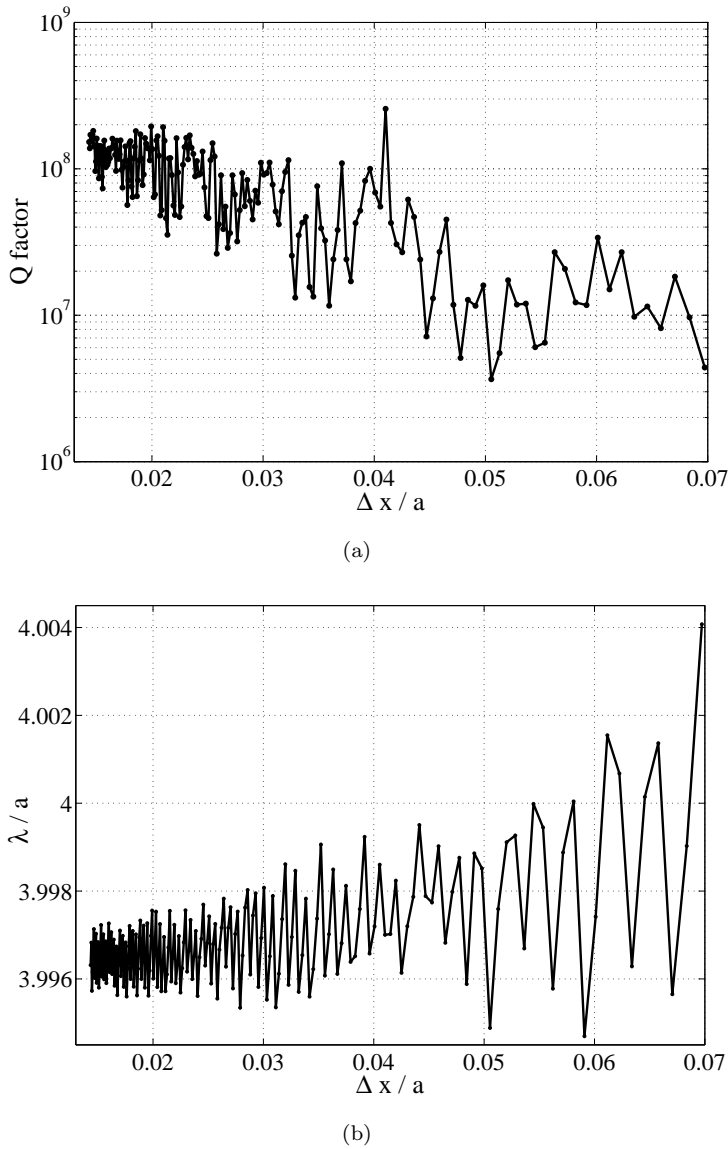


Figure 4.8: 2D (a)  $Q$  and (b)  $\lambda$  convergence for the third design from Table 4.1. Buffer layers are  $1a$ -wide with *arctanh* free-space squeezing, covered on  $1/3$  by the PMLs,  $x$ -PMLs comprising 3 grid cells,  $\Delta x = \Delta y$ .

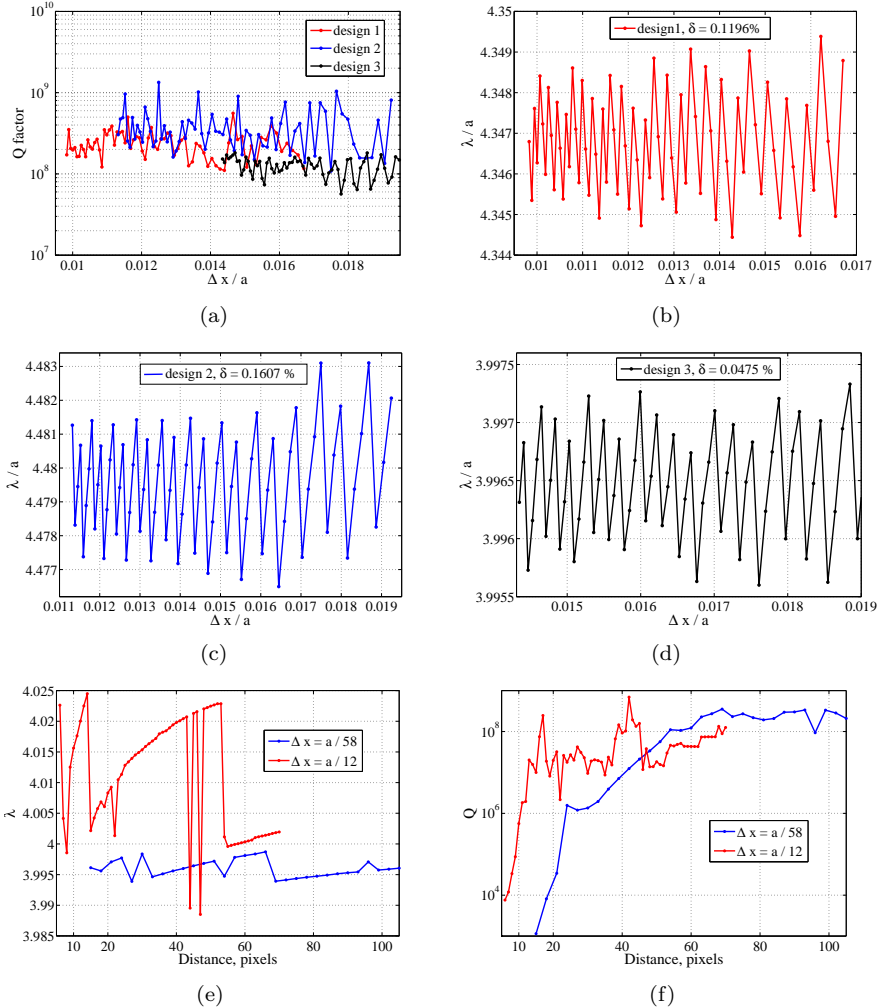


Figure 4.9: 2D simulations with  $\Delta x = \Delta y$ , free-space squeezing is done with the hyperbolic arctangent function, buffer layers are covered on 1/3 by the PMLs,  $x$ -PMLs comprising 3 grid cells. (a)  $Q$ -factor and (b)-(d)  $\lambda$  convergence for the three designs in the region of fine resolutions with estimation of spread  $\delta$  shown in the legend. Buffer layers are  $1a$ -wide. (e) Eigenwavelength and (f)  $Q$ -factor evolution for the third design with the domain size increase (i.e. with increase of the distance  $s$  shown in Fig. 4.7); two grid cell sizes considered are as shown in the legend.

Having established that  $a_n$  and  $d_n$  should vary somehow we investigated several ways to that. Following the mode-matching approach to high- $Q$  nanobeam cavities [65, 152] perforation should consist of two regions: a long periodic part acting as a Bragg reflector and a chirped, mode matched defect region. Several laws to tailor the nanobeam design have been compared. Among them are  $1/\sqrt[10]{n}$  multiplier to decrease both  $a_n$  and  $d_n$  (design 1); cavity formation similar to [62] when hole diameter and lattice constant vary linearly in the reciprocal space (design 2); and linear decrement of  $a_n$  and  $d_n$  towards the middle of nanobeam [65]. With all mentioned designs we were able to rise the  $Q$ -factor to the order of  $10^8$  simply by playing with parameters. Table 4.1 summarize details of different nanobeam cavity designs. For the first and third designs we start by defining modified hole diameter  $d_n$  and modified segment size  $a_n$  is calculated afterwards. For the design three calculation of modified lattice constant  $a_n$  precedes evaluation of the defect hole diameters.

In Fig. 4.8 an example of the  $Q$  and  $\lambda$  convergence curves for the design three is plotted starting from a quite coarse resolution, while Fig. 4.9a–d allows to do more detailed comparison between different designs in the region of fine resolutions. Special attention to this is required because the convergence of the nanobeam cavity is worst than for the membrane resonators, which is seen already in 2D simulations, Fig. 4.9a. Indeed, 1D PhC basis for the nanobeam cavity somewhat less reflecting than 2D stop band utilized in the membrane resonators. It leads to less  $Q$  stability when fabricated nanobeam design or its finite difference description has imperfections.

All of the designs from Table 4.1 have similar  $Q$ -factor values, Fig. 4.9a, the design three revealing faster convergence than others. In Fig. 4.9b–d the resonance wavelength convergence is plotted for the three designs in the same  $\Delta x$  range as in Fig. 4.9a. To estimate the convergence rate, relative spread  $\Delta\lambda$  of convergence curves around a central wavelength  $\lambda_0$  can be introduced:  $\delta = \frac{\Delta\lambda}{\lambda_0} 100\%$ . The design three has  $\delta$  one order less than the designs one and two even at rougher resolutions. Thus we came to the modification according to the linear law as better converging numerically. The design three will be used in all further nanobeam cavity simulations with hope that better numerical stability can lead also to better potential stability with respect to the design perturbations.

Figure 4.9e,f elucidates the influence of the domain size on  $Q$  and  $\lambda$  calculation. A distance  $s$  from the nanobeam frontier to the end of the computational domain, see Fig. 4.7, is increased incrementally by adding more grid cells. Red lines correspond to the grid cell of  $a/12$  which clearly gives strongly overestimated resonance wavelength in Fig. 4.9e because of too rough discretization. Refining of the sampling (to 58 points per lattice constant  $a$ ) significantly minimizes the relative error in  $\lambda$ -evaluation and most interestingly, this error stays the same irrespective of the actual domain size so that even for as small buffer as  $15 \cdot a/58 \approx 0.26a$  correct  $\lambda$ -calculation takes place. It means that eigenwavelength computation is not that sensitive to the buffer layers extension as to the choice of good sampling, what is in agreement with the sphere considerations before.

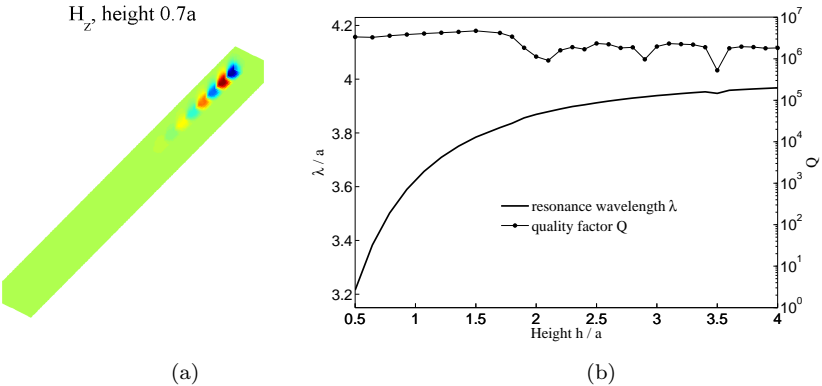


Figure 4.10: (a) 3D field patterns of the TE mode in the nanobeam cavity of the height  $0.7a$ . (b) Resonance wavelength  $\lambda$  and  $Q$ -factor dependence on the nanobeam height  $h$ . The grid cell is cubic,  $\text{arctanh}$ -buffer layers are of  $a$  size along both  $y$  and  $z$ -directions,  $a/3$  distance goes for the PMLs,  $x$ -PMLs are 3 cells wide.

Minimal optimal domain size when  $Q$ -factor calculation saturates and does not improve anymore with the domain size prolongation shows up in Fig. 4.9f. This minimal domain size, that is already enough for the most accurate  $Q$  evaluation at the given meshing, can be estimated as  $\sim 12 \cdot a/12 = 58 \cdot a/58 = 1a$ . Thus for the nanophotonic cavity we see the direct analogy of the FDFD method performance observed before for the simple spherical resonator.

## 4.2.2 3D modeling

### Nanobeam height variation

In the 3D modeling a defect region in the nanobeam cavity is perforated according to the design three from Table 4.1. Fig. 4.10 shows dropping of the resonance wavelength of the TE-mode in the nanobeam cavity with the reduction of the nanobeam height  $h$  along the third  $z$ -direction. Decreasing of the nanobeam height also greatly minimizes mode volume, so that for the height  $h = 0.5a$  it is equal to  $0.86 (\lambda/n)^3$ . We use these nanobeam height in the following convergence studies and for the modeling of the coupled cavity structures.

### Equidistant mesh, arctanh squeezing function

Figure 4.11 demonstrate the  $Q$  and  $\lambda$  convergence for the two domain sizes when buffer squeezing function is arctangent based and thus relatively flat, i.e. the grid step is just slowly increased in physical space behind the nanobeam border. This relatively weak and slow squeezing requires long enough distance left from the nanobeam frontier to the PML start. Thus the PMLs occupying

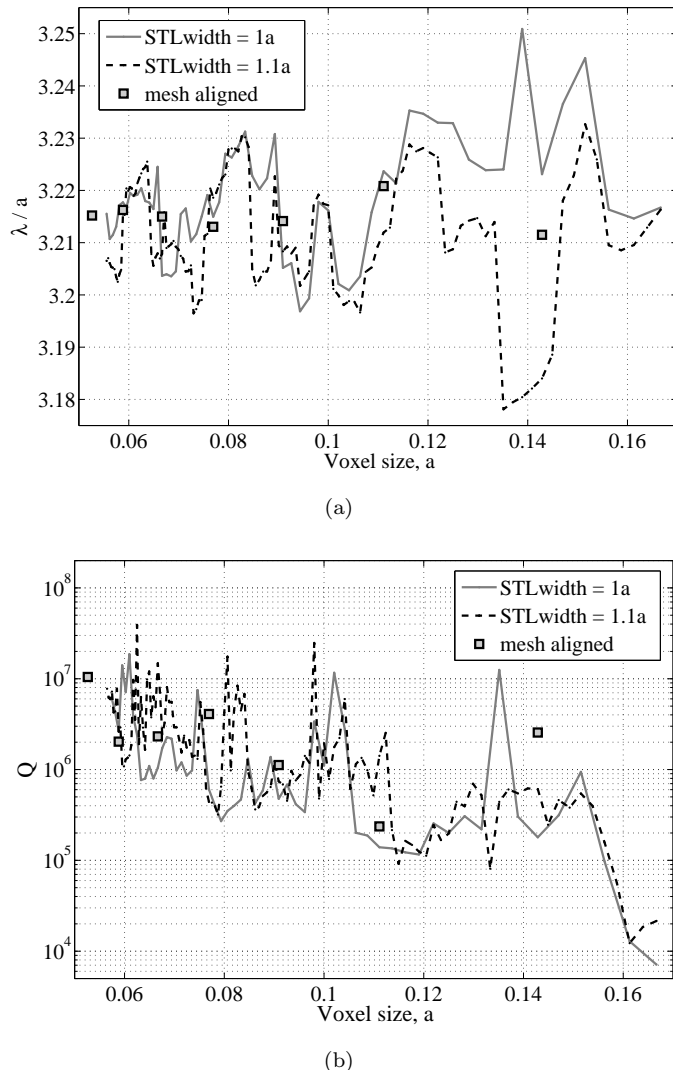


Figure 4.11: (a) The resonance wavelength and (b) the  $Q$ -factor versus grid size for the two STL widths. The PMLs width in x direction is 3 grid cells.

third part of the buffer is an optimal choice here. The Yee cell is cubic here in the whole range of voxel sizes.

The resonance wavelength calculation has uncertainty less than 1%. Evaluation of the resonance wavelength can be improved by using, for example,  $H_z$  mesh aligned with respect to the flat nanobeam surfaces. In this case the averaging procedure does not depend on the finite number of subpixels used to make polarization-sensitive averaging and finite-difference description of the permittivity become better what should improve also simulation results. Indeed, when  $H_z$  mesh nodes coincide with the slab-air interface (square points in Fig. 4.11a, better stability for the  $\lambda$  calculation is achieved, although less sampling points might be plugged into the mesh-aligned convergence curve.  $Q$ -values given by the aligned mesh seems to lie on the nonaligned mesh convergence curve close to the average value of  $\lambda$  oscillations.

There is no visible difference between the non-aligned and aligned  $Q$ -factor values, Fig. 4.11b. In general, precision of the  $Q$  computation does not depend significantly on a particular grid step and on the averaging procedure used to find finite-difference array for permittivity. Thus this is reasonable result that aligning of the mesh does not influence the  $Q$ -evaluation. The  $Q$  convergence is not that good for both meshes, what is related to 1D-like structure for the nanobeam cavity.

### Non-equidistant mesh, $x/(1-x)$ squeezing

Now we consider the steepest squeezing function from Fig. 3.4, which allows to start the PMLs in the computational space closer than at  $2a/3$  distance from the nanobeam surface for the buffer size being  $1a$ . The PML size of half the buffer should improve simulation results because the nanobeam-to-PMLs distance stays of the same size in physical space as it was with the arctangent function before. From Fig. 4.12a we see that the results for  $\lambda$  attain improvement compared to those in Fig. 4.11, the relative uncertainty in  $\lambda$  is reduced more than twice. The  $Q$ -factor evaluation is so unstable that both Fig. 4.11b and Fig. 4.12b show similar convergence behavior. We can remind here that low accuracy of the  $Q$ -factor evaluation reflects high sensitivity of the  $Q$ -factors of 1D photonic-crystal-based structures to imperfections in their finite-difference description. Small perturbations in wavevectors caused by imperfections strongly effect the efficiency of coupling with leaky modes lying inside the light cone. Due to the 1D nanobeam geometry this perturbations are more pronounced than in the case of 2D photonic crystals resonators. This leads to considerable variations in the nanobeam cavity  $Q$ -factor, whereas resonance wavelengths remain stable. Nevertheless, the obtained  $Q$ -factor values give a reliable order-of-magnitude estimate. The nonuniform mesh (blue curves in Fig. 4.12) applied along  $x$ -direction,  $\Delta y$  being equal  $\Delta z$ , greatly reduces memory requirements and computational time while preserving convergence properties similar to uniform mesh for both  $\lambda$  and  $Q$ .

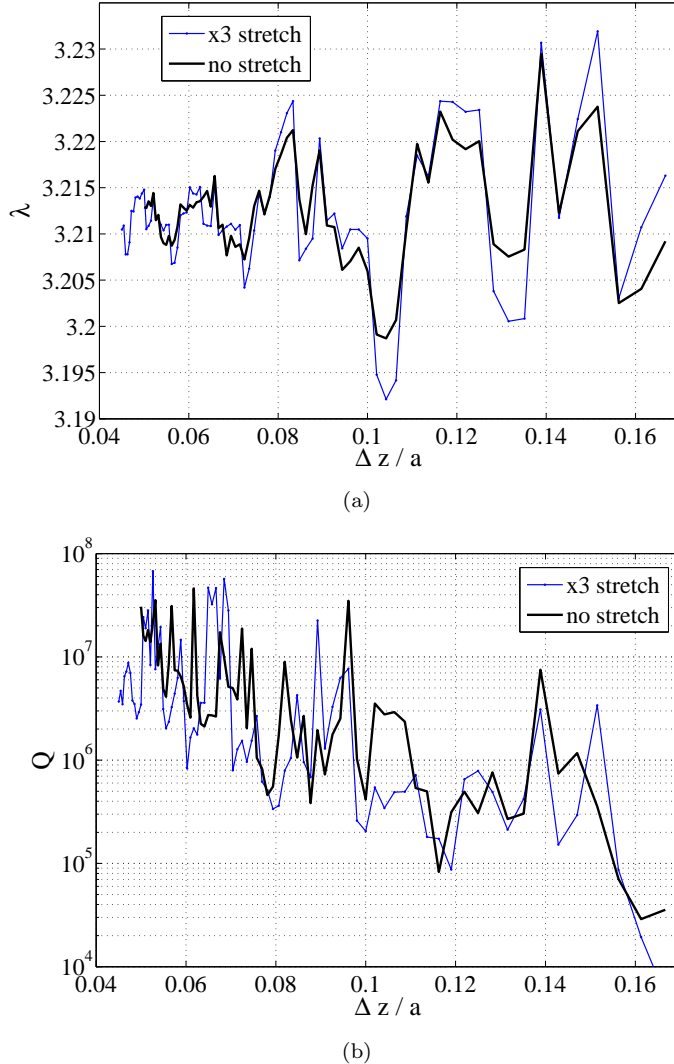


Figure 4.12: (a) The resonance wavelength and (b)  $Q$ -factor versus grid step for uniform ( $\Delta x = \Delta y = \Delta z$ ) and nonuniform S3  $x$ -mesh from 4.4. Buffer size along  $y$  and  $z$  directions is 1 $a$ -wide with 1/2 occupied by the PMLs, the PMLs width in  $x$ -direction being 3 grid cells.

# Chapter 5

## Coupled nanobeam cavities

Optical elements based on a coupled system possess rich functionality owing to additional degrees of freedom given by varying displacement of cavities and efficient frequency tuning. Change of coupling strength of the resonators with their rearrangement addresses the issue of parasitic interaction between components which is so important for integrated photonics. Side-coupled nanobeams [77,152,153] offer new possibilities for shaping optical fields at nanoscale, which is potentially beneficial for various applications including trapping and manipulation of particles [154], sensing and optical switching through optomechanical interactions with suspended nanobeams [63, 64]. Realization of flexible control over the mode coupling in arrays of nanocavities will also contribute to the development of on-chip quantum-optical interferometers [71] and quantum computers [155].

Spectral position of the supermodes formed in two cavities placed side by side can be analyzed with the FDTD technique. The problem is that if several modes are traced in the time domain within a single run, the accuracy of the  $Q$ -factor determination may degrade, and extraction of the separate mode field profiles requires Fourier transformation of field evolution stored for some space volume and time interval. If the two modes are degenerate, separating them one from the other with the FDTD method is even less trivial, especially if at the degeneracy point the coupled structure does not have a plane of symmetry allowing to split the two modes by the appropriate domain reduction. On the contrary, the FDFD technique grants an opportunity to get straightforwardly, in one run, the pictures of several modes, their eigenvalues and quality factors. Even when the modes in the coupled cavities are degenerate, we get an idea how they may look like — though the picture becomes now ambiguous. In this Chapter 5 the FDFD technique is used to analyze single and coupled photonic crystal nanobeam cavities.

## 5.1 Two coupled nanobeams

We suggested and show numerically that longitudinal shift in nanobeam cavities significantly alters coupling efficiency between multiple closely packed resonators. Whereas the concept of longitudinal offset between cavities has been previously developed for dielectric rod arrays at microwave frequencies [156] and micro-scale ring resonators at optical wavelengths [79], we demonstrate here new possibilities for light control at nanoscale. In particular, we show that for particular values of the longitudinal shift, the cavity modes become degenerate irrespective of the transverse shift between nanobeams.

When two identical cavities are positioned parallel to each other, their modes undergo hybridization. Supermodes possess symmetric or anti-symmetric profiles [153] and shift in frequency up and down from the former level. We will refer to this splitting as frequency detuning. The frequency detuning between the supermodes normally increases as the cavities are brought closer, and such sensitivity to separation can lead to pronounced optomechanical phenomena. This may have various applications, including mechanically-induced frequency conversion for optical waves [123]. Analogous effects of modes splitting occur in coupled periodic waveguides, where several channels can enrich the band structure of a single mode waveguide in a controllable way, e.g. in slow light modes positioning at the band edge on demand.

### 5.1.1 2D analysis of field profiles

First we analyze two side-coupled nanobeam cavities as in Fig. 5.1a where the right half of the structure is shown (the left half is symmetric). The individual identical nanobeams has design 3 from Table 4.1. This gives a linearly chirped array, while other designs are also possible; the general mode properties are usually similar for different chirp functions. The resonance wavelength of such single nanobeam in 2D is  $\lambda = 3.9964a$ ,  $Q = 1.5 \cdot 10^8$ , Fig 4.8. Two parameters describe the position of the second nanobeam cavity relative to the first one: the transverse separation  $p$  and the longitudinal shift  $s$ , Fig. 5.1a.

To make the computational work efficient all modeling is done at the beginning for 2D nanobeam geometries with main emphasis on field patterns redistribution as coupled resonators are rearranged. As we are interested in coupling effects between two nanobeam resonators when they are shifted longitudinally and transversally with respect to each other, we need to perform a new computational cycle each time the structure is modified by a small displacement. In the 2D case the execution time is several minutes even for huge resolutions such as  $n_{tot} = 6 \cdot 10^5$  grid nodes available with a 8Gb station.

Mode profiles in Fig. 5.1b,  $s = 0$ , shows formation of the symmetric and antisymmetric cavity modes when two nanobeam resonators are brought together. Magnetic field hot spots coincide with the location of holes. At the separation  $p = 1.5a$  we see only electric field in the air gap between the nanobeams. When one of the nanobeams is subjected to a longitudinal shift the system loses its

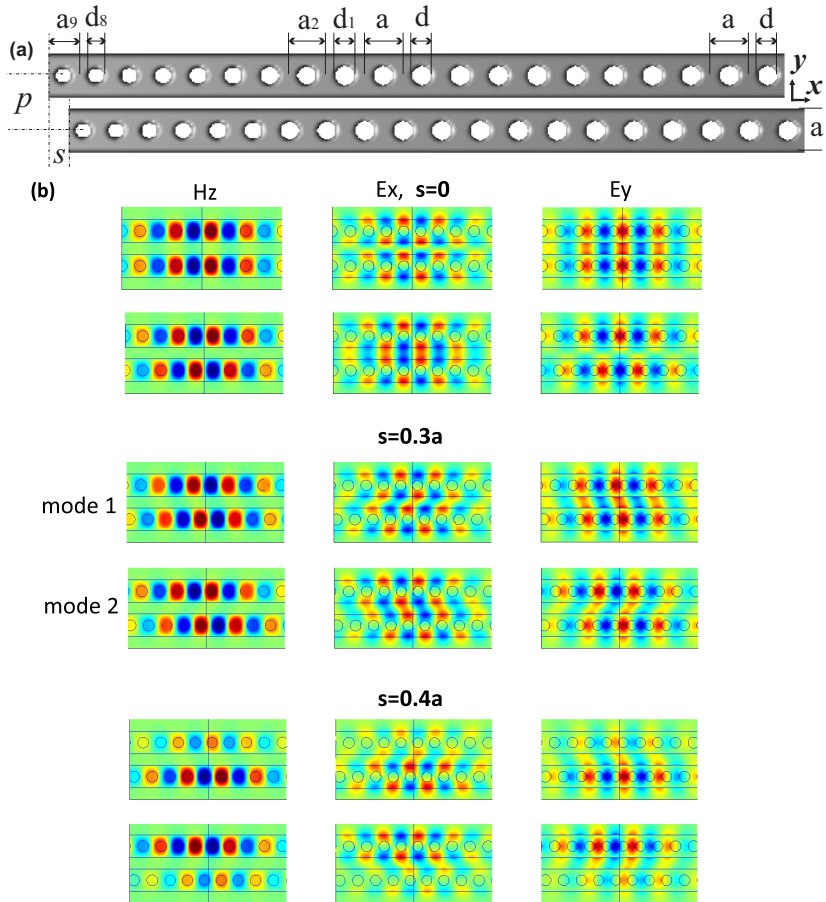


Figure 5.1: (a) Two nanobeams, each of width  $t = a$ , refractive index  $n = 3.4$  and drilled with 20 holes in each half, separated one from another by  $p$  and shifted longitudinally by  $s$ . (b) Field profiles for modes (labeled mode 1 and 2) in coupled cavities with zero,  $s = 0.3a$  and  $s = 0.4a$  longitudinal shifts when separation  $p = 1.5a$ , for each shift mode one being positioned at the top while mode two takes the bottom position.

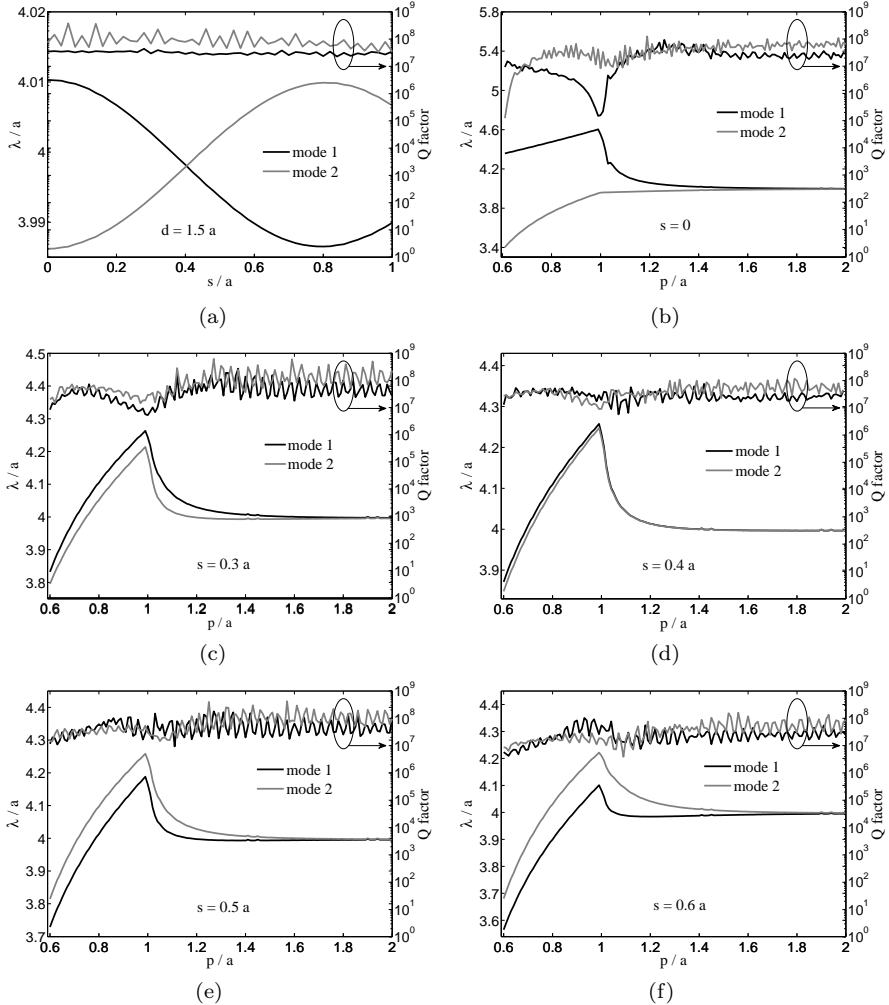


Figure 5.2: (a) Detuning of the mode one and mode two vs the longitudinal shift. Transverse separation between nanobeam axes is  $p = 1.5a$ . (b)-(f) Resonance wavelengths and  $Q$ -factors of eigenmodes in side-coupled nanobeam cavities vs. their transverse separation  $p$ . Results are presented for four different shifts: (b)  $s = 0.0a$ ; (c)  $0.3a$ ; (d)  $0.4a$ ; (e)  $0.5a$ , (f)  $0.6a$  as indicated by labels. Separation of  $1.0a$  and less corresponds to a single dielectric beam with two rows of holes.

symmetry and modes cannot be specified anymore as symmetric and antisymmetric. We will refer to notation mode 1 and mode 2 to call transformations of even and odd modes respectively with gradual shift starting from zero.

At zero longitudinal shift  $E_x$  component of mode 1 and  $E_y$  component of mode 2 has a node plane passing through the middle of the air gap between the nanobeams ( $y = 0$ ). For applications requiring high field intensities it would be preferable to avoid these zero-valued fields. It turns out that as nanobeams are gradually shifted from  $s = 0$  the node planes for both of these modes components are substituted by a plane with high field intensities, see Fig. 5.1b for  $s = 0.3a$ . At the same moment other electric field components ( $E_y$  for mode 1 and  $E_x$  for mode 2) still preserve quite high field values. Thus, small longitudinal shift helps in removing areas of zero fields in the air gap and makes electric field intensity more uniform through the gap between the two nanobeams. The field uniformity in shifted nanobeams can be further improved by moving nanobeams closer transversally.

From Fig. 5.2a it is evident that modes experience degeneracy at around  $0.4a$  shift. At the greater shifts eigenwavelength difference again grow up forming a periodic dependence of frequency detuning on the shift  $s$ . We also trace the effect of the transverse cavity separation  $p$  on the resonant wavelengths and Q-factors for different longitudinal shifts  $s$ . Results are presented in Figs. 5.2b–f. Almost exact degeneracy is observed at  $s = 0.4a$  for all transverse separations, Fig. 5.2d: the two principle eigenmodes are resolved in the FDFD numerical simulations with their frequency detuning being much smaller than for the other shifts.

Away from degeneracy point, each mode profile should support the  $180^\circ$  symmetry of the photonic structure around a central point ( $x = y = 0$ ) between two cavities, and specifically the magnetic field components should satisfy the relations  $H_z(x; y; z) = p H_z(-x; -y; z)$ , where  $p = +1$  or  $p = -1$  for the two fundamental modes of couple cavities [157]. These symmetries are visible for mode profiles shown in Fig. 5.1b and Fig. 5.3c,d. However we note that exactly at the degeneracy point, the field profiles of the eigenmodes are defined with certain ambiguity and do not have to satisfy the rotational symmetry, since any linear combination of two eigenmodes is an eigenmode as well. As shift starts approaching  $0.4a$  we see that field intensity in the air gap and in one of the nanobeams falls down, Fig. 5.1b for  $s = 0.4a$ . The connection between the modes weakens. As the result modes settle mostly in one or another nanobeam, Fig. 5.5b, bottom panel. At the degeneracy point field profiles of the eigenmodes are defined with certain ambiguity, since a linear combination of two given eigenmodes is an eigenmode as well. And we see this in the numerical experiment: alongside with field profiles as in Fig. 5.5b we often obtained the mode fields concentrated only in one nanobeam indicating weak coupling between the resonators. In more complicated structures, where cavities are tuned by infiltration, similar effects of anticrossing were registered experimentally [82] (there is always some perturbation present, which, strictly speaking, removes the degeneracy, thus in fact both terms — mode degeneracy

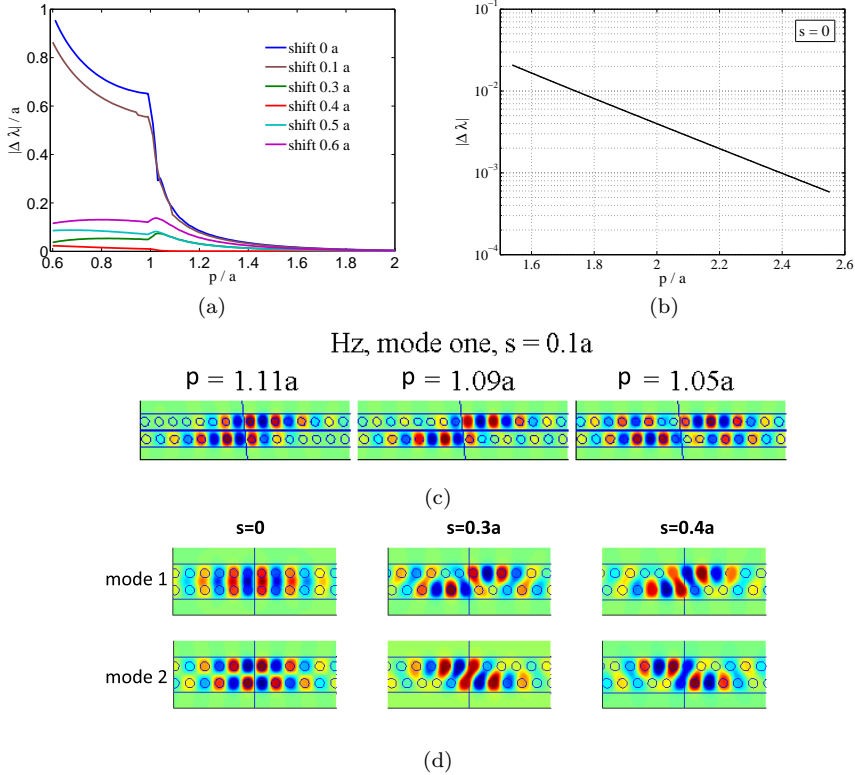


Figure 5.3: (a) Increase of eigenwavelength difference with shortening of transversal separation  $p$  between the nanobeams, different shifts are printed in the legend. (b)  $|\Delta\lambda|$  in logarithmic scale for nonshifted nanobeams. (d) Evolution of magnetic field  $H_z$  in two slightly shifted nanobeams ( $s=0.1a$ ) when closing the air gap between them, i.e. separation  $p$  is reduced from  $1.1a$  to  $1.05a$ . (c)  $H_z$  field distribution in two connected nanobeams with  $p = 0.9a$  at  $s = 0$ ,  $s = 0.3a$  and  $s = 0.4a$  shifts.

and anticrossing — can mean the same here).

In Fig. 5.3a the eigenwavelength difference is plotted showing the highest values for non-shifted resonators and significantly smaller  $|\Delta\lambda|$  for non-zero shifts. Due to symmetric positioning of  $0.3a$  and  $0.5a$  shift values around the degeneracy point, the wavelength difference given by these shifts are equal to each other for nanobeams separated by  $p > 1.1a$ . When nanobeams are far enough transversally and coupling strength is small,  $|\Delta\lambda|$  depends on  $s$  by order law seen in Fig. 5.3b. In Fig. 5.3b for illustration purpose the spectral splitting for non-shifted nanobeams is plotted in a logarithmic  $y$ -scale; the other nonzero shifts, except for the degeneracy point, also give similar straight lines in the  $|\Delta\lambda|$ -log scale if separation  $p$  is big enough to correspond to the weak

coupling regime.

When the resonators are moved transversally closer so that separation between them decreases, the interaction between the nanobeams intensifies, and all fields, including magnetic one, spread through the air gap. The picture of the mode profiles alters compared to  $p = 1.5a$ , see Fig. 5.3c,d. Eigenmode fields extend over the whole cavity even when the hole positions in upper and lower cavities are effectively shifted in the out-of-phase configuration, i.e.  $s = 0.4a$ . In Fig. 5.3c the evolution of mode 1 at small shift  $0.1a$  is shown when closing the air gap. Drastic changes occur with the mode 1 profile when connecting the nanobeams: yet very intensive field at  $p = 1.11a$  is strongly pushed out from the cavity center at  $p = 1.05a$ . Thus for nonlinear applications special care should be paid to the extremely thin slots between the nanobeams. Fig. 5.3d collects field patterns for both modes at different shifts when air-dielectric interfaces are absent and we actually have one cavity consisting of two chirped arrays. In Fig. 5.3d the mode 1 has quite complicated field distribution at  $s = 0.3a$ , however becoming symmetric to the mode 2 field profile at the degeneracy  $s = 0.4a$ . Note that although field maps in stitched nanobeams are really complex they are all  $180^\circ$  rotation symmetric relative to the center point between the nanobeams.

### 5.1.2 3D $Q$ and $\lambda$ dependence on the longitudinal shift

In 3D we consider the same nanobeam design from Fig. 5.1a and discuss more the development of the  $Q$  and  $\lambda$  curves with the rearrangement of the nanobeams. The 3D  $Q$ -factor of a single nanobeam cavity is around  $4 \cdot 10^6$  and the operating wavelength  $\lambda = 3.21a$  for the TE mode, Fig. 4.12. To achieve fine sampling in 3D problems symmetry domain reduction is applied were it is possible to satisfy memory requirements. The system of two nanobeam resonators with a longitudinal shift loses plane-reflection symmetry and the whole domain should be considered so benefits of stretched meshes is fully used here. Discretization in the cavity center is set to  $0.05a - 0.1a$  with sparser mesh in the rest of the structure. 3D  $Q$ -factor computations are done on a 48 Gb station with the maximum execution time approaching 2 hours per single run. Correct averaging is an important issue in 3D simulation where that fine resolution as in 2D cannot be achieved. As  $p \rightarrow 1$  a unit Yee cell might contain two boundaries from two closely spaced nanobeams and the averaging should be done only once taking into account both boundaries simultaneously.

Moving nanobeams closer to each other leads to stronger coupling and pronounced increase of the eigenwavelength difference between the doublet of supermodes, see Fig. 5.4a. At  $p = a$  the system is changed abruptly as the gap between the two nanobeams disappears, so the structure consists now of a single high-dielectric bar with two parallel rows of holes in it. That explains a characteristic peak in the wavelength dependence of the mode eigenfrequency plotted in Fig. 5.4a. Mode 1 (even) has higher wavelength than mode 2 (odd) for the whole range of separations  $p$  as can be easily seen from a simple per-

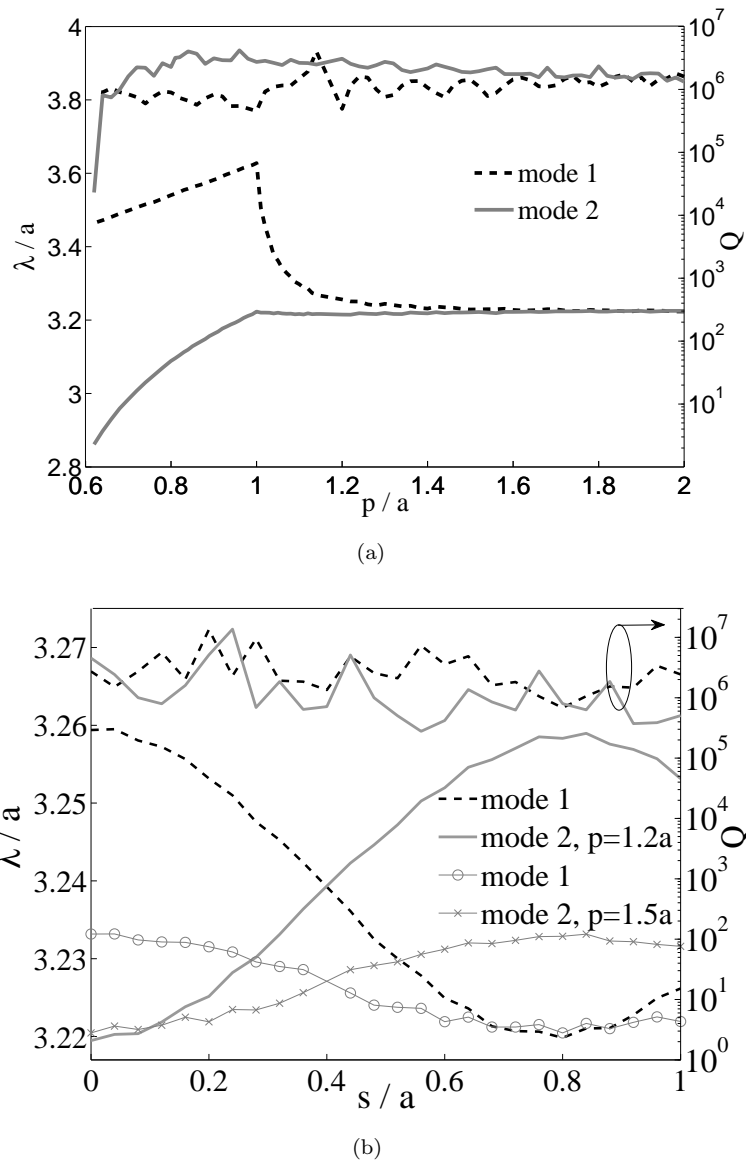


Figure 5.4: Tuning of resonance wavelengths of coupled modes by (a) changing separation between non-shifted ( $s = 0$ ) nanobeams; (b) changing the longitudinal shift  $s$  for two separations ( $p = 1.2a$  and  $p = 1.5a$  as indicated by labels). Right axis shows the 3D  $Q$ -factor values.

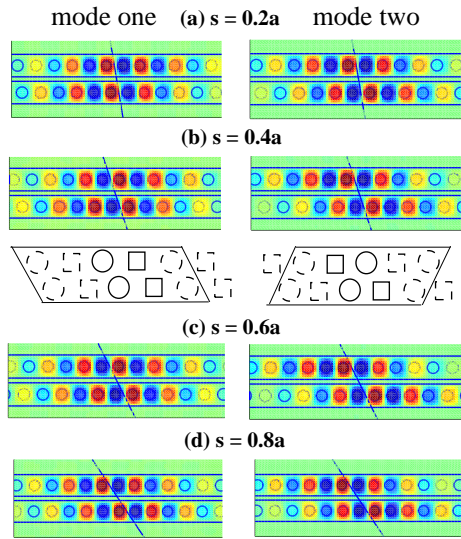


Figure 5.5: Magnetic field  $H_z$  of even and odd modes in coupled nanobeams for  $p = 1.2a$  at different longitudinal shifts.

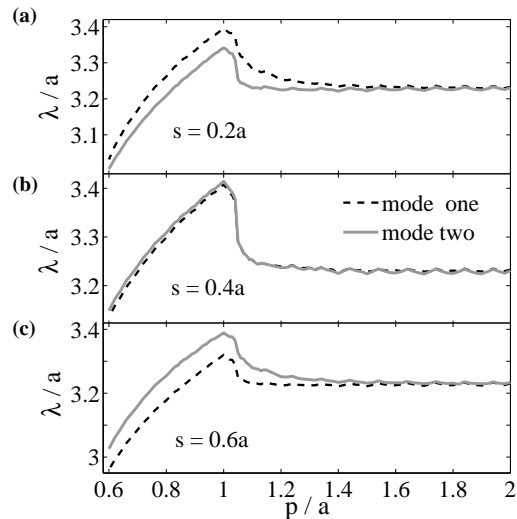


Figure 5.6: Splitting of resonance wavelengths of even and odd modes versus separation  $p$  for (a)  $s = 0.2a$ ; (b)  $s = 0.4a$ ; (c)  $s = 0.6a$ .

turbation theory [158]. When the gap between nanobeams is closed and the  $y$ -dimension is further reduced, the effective refractive index of the system and hence the eigenwavelengths are also decreased [41]. Remarkably, when varying the separation no significant variation in the  $Q$ -factor is seen. The  $Q$ -factor value is close to  $10^6$  for both even and odd modes, see Fig. 5.4a.

Now we analyze the effect of the longitudinal shift  $s$ . In Fig. 5.4b the wavelengths and  $Q$ -factors of the fundamental eigenmodes vs. shift  $s$  for separations  $p = 1.2a$  and  $p = 1.5a$  are plotted. As the shift starts growing from zero, mode detuning is reduced and, independent on separation  $p$ , the modes become degenerate at around  $s \simeq 0.4a$  what is in contrast to resonators with unmodified lattice constant [156] where the degeneracy shift was exactly  $0.5a$  independent on rod radii variation. Thus this is primarily variation of lattice constant that is responsible for the specific value of the degeneracy shift. Note that  $0.4a \simeq 0.5a_6$ , i.e. the shift at degeneracy point is approximately equal to half the average lattice constant in the cavity region.

In Fig. 5.5b for  $s = 0.4a$  we plot another picture at the degeneracy compared to Fig. 5.1b with the magnetic field nodes in one nanobeam opposing field lobes in another. These degenerate modes can be schematically sketched with diagrams in Fig. 5.5b. Standing wave profiles with slow spatial decay from the center of the cavity towards the periphery allow neglecting low-intensity outer regions and then central parts of the patterns are identical upon reflection, making the occurrence of the degeneracy point (geometrically, central parts of the defect regions for the two modes also satisfy reflection-symmetry if chirped hole diameters approximated to be the same in the middle). Had mode profiles less gradual changes in the succession of field minima and maxima along the nanobeams (as shown by bold circles and squares in the diagrams), the formation of the degeneracy would be hardly possible.

For the shifts larger than  $s = 0.4a$  the mode detuning is increased, reaching a maximum at around  $s \simeq 0.8a$  where eigenwavelength difference approaches the same value as at  $s = 0$ . The revival of coupling at  $s \simeq 0.8a$  is again due to the gradually chirped nanobeam design and field profiles extended along the nanobeams. Thus mode detuning depends on the shift almost periodically, and the cavity modes 1 and 2 are adiabatically transformed as the parameter  $s$  is varied from 0 to  $a$ , see Fig. 5.5d where it is shown that mode 1 and 2 exchange their parity going from  $s = 0$  to  $s = 0.8$ . Most important, the  $Q$ -factor values remain of the same order of magnitude as for a single cavity.

In Fig. 5.6 we compare the eigenmodes wavelength dependencies on separation  $p$  for three longitudinal shifts  $s = 0.2a, 0.4a, 0.6a$ . The upper panel shows the reduced spectral detuning of the modes for the intermediate shift  $s = 0.2a$ . The plot in Fig. 5.6b shows that for non-overlapping nanobeams the modes are almost exactly degenerate at  $s = 0.4a$  for any transverse separation  $p$ . After the degeneracy point, at  $s = 0.6a$  modes 1 and 2 swap their wavelengths.

By comparing Fig. 5.2 against Figs. 5.4 and 5.6 we see that 2D and 3D simulations give essentially similar dependencies for  $\lambda$  and  $Q$  on the longitudinal shift  $s$  and transversal separation  $p$  of the cavities, indicating the possibility to

design coupled nanobeam cavity systems in 2D successfully. This is because the physics of coupling of dielectric nanobeam cavities is relatively simpler than, for example, the coupling of metallic split-ring resonators where essentially three-dimensional interplay of magnetic and electric excitations is important.

## 5.2 Three coupled nanobeams

In multiple side-coupled nanobeam cavities the modes can also be tuned by longitudinal shifts with the degeneracy observed at certain shift. Degeneration of modes in structures containing many elements amounts to the absence of parasitic coupling between the neighboring units. Instead of increasing the distance between optical components usually used to minimize cross-talk, longitudinal shift can be proposed to create dense photonic integrated circuit. Moreover, by appropriate choice of transversal separation the degeneracy wavelength of coupled nanobeams (up to three resonators in our tests) can be tuned to a single nanobeam resonance wavelength. This potentially allows adjacent waveguiding components, all together, and each separately, to operate at the same wavelength. For example, compact single-wavelength switch matrix can be created on the basis of a nanobeam-switcher with nonlinearity [150]. Another field of application is building an array of nanobeam cavities to form a quantum optical network where many identical resonators should be placed closely one to another on a chip [155]. Additionally, by controlling the mode coupling it becomes possible to tailor the optical field across an array of multiple nanocavities for applications in particle trapping [154] and tailored optomechanical interactions [63, 64].

### 5.2.1 Weak coupling regime

We did 2D simulations (letting the nanocavities be infinitely high) to catch basic features of mode tunability. For three side-coupled nanobeam cavities their relative alignment can be characterized by separations  $p_2, p_3$  and longitudinal shifts  $s_2, s_3$  of the second and third cavities. As an example we consider equally spaced ( $p_2 = p_3 = p$ ) nanobeam cavities, only the middle one being shifted:  $s_2 = s, s_3 = 0$ . The dependence of mode wavelength detuning (relative to a single cavity) on the shift  $s$  is given in Fig. 5.7a for  $p = 2.3a$ . We observe behavior similar to the case of two nanobeams. Specifically, all three modes become degenerate at  $s \simeq 0.4a$ ; by varying  $p$  we can control the wavelength of the degenerate modes, and it coincides with the wavelength of a single cavity, Fig. 5.7a. Mode profiles for non-shifted system ( $s = 0$ ) are shown in Fig. 5.7b. Note that mode 3 is localized at the outer cavities, so its wavelength is not sensitive to the middle cavity shift as observed in Fig. 5.7a. There is a nice mechanical analogy with modes of three weakly coupled pendulums: in mode 1, all three pendulums are swinging in phase; in mode 2, two outward pendulums move forward while the middle one moves backward; in mode 3, the central

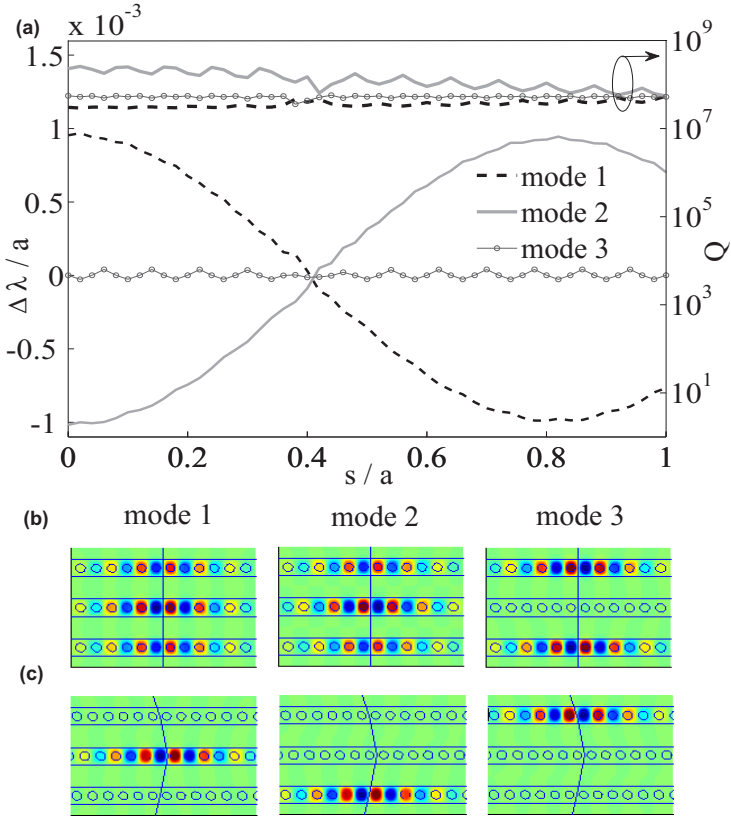


Figure 5.7: Modes in three side-coupled nanobeam cavities with transversal displacement between the neighboring nanobeams being equal to  $2.3a$ . The middle nanowire is longitudinally shifted, the other two being kept stationary. (a) Spectral detuning of the three modes from the single nanobeam cavity wavelength  $\lambda = 3.9965a$ . Right y-axis—the  $Q$ -factor of the three coupled modes (for an isolated nanobeam cavity,  $Q = 1.5 \cdot 10^8$ ).  $H_z$  profiles for the modes in the three (b) unshifted and shifted by (c)  $0.41a$  nanobeams.

pendulum is at rest and two others are moving oppositely.

At the degeneracy point ( $s \simeq 0.4a$ ) the eigenmode profiles can be primarily localized at individual cavities, see Fig. 5.7c. In Fig. 5.7c the mode profiles at  $s = 0.41a$  reveal complete vanishing of field in neighboring nanobeams whereas for two coupled nanobeams shift of  $s = 0.4a$  was more likeable to be called the exact degeneracy shift value. In fact, it is quite difficult to detect precise value of the degeneracy as it requires extremely fine step in  $s$  and long simulation times; besides, accuracy of computation is also limited by the finite-difference description. However small deviations from the exact degeneracy does not

change field mapping significantly as solutions to Maxwell's equations are all smooth functions.

Wavelength detuning is much less pronounced at  $p = 2.3a$  than at  $p = 1.5a$ ,  $p = 1.2a$  considered previously. The reason to choose the separation  $p = 2.3a$  is that coupling between the nanobeams is already weak and the energy splitting becomes symmetric relative to the initial energy level as follows from the standard perturbation approach. And the degeneracy wavelength of an array of nanobeams is the same as the isolated nanobeam eigenwavelength (this is not true for the case of strong coupling at  $p = 1.5a$ ).

Although we are in the weak coupling regime, spectral splitting corresponding to  $p = 2.3a$  is about 0.2%, which for telecom wavelength  $1.5\mu\text{m}$  amounts to 3 nm spread in wavelength. A comparable shift in resonance wavelength is induced by inclusion of nonlinearity in the nanobeam; this allows cavity operation as a switcher totally transmitting or suppressing the signal depending on turning on/off the nonlinearity [150]. Thus 0.2% energy difference for multiple nanobems placed at  $p = 2.3a$  on a photonic integrated chip introduces parasitic coupling hindering single-wavelength operation. The distance  $1.3a$  between nanobeam edges (corresponding to  $p = 2.3a$ ) is not that large in terms of interaction between the cavities.

If we further suppose the core of nanobeam cavity is nonlinear (e.g. taking into account refractive index increase due to nonlinearity), then the degenerate modes in the array of nonlinear cavities can be also tuned to a single resonator wavelength by  $p$  variation. A single-wavelength operating switching array can be build on the basis of such nanobeam cavities that will work equally well for single- or multiple-channel excitation applied. (In the case of the single-cavity nonlinear operation based on 0.03% change in refractive index, the frequency shift due to presence of neighboring 'passive' nanobeams is estimated to be around a negligible  $2 \cdot 10^{-4}\%$ ).

We have verified that mode degeneracy also occurs in four side-to-side coupled nanobeam cavities. Thus we expect mode degeneracy in multiple side-coupled cavities when they have staggered longitudinal shifts, such that neighboring nanowires are shifted longitudinally by  $s \simeq 0.4a$ . We also expect that the  $Q$ -factor in multi-cavity structure should remain of the same order of magnitude as that of a single nanocavity.

### 5.2.2 Strong coupling regime

Strong coupling regime is investigated by doing 3D simulations with symmetry planes being enforced through the domain reduction. For the three nanobeams dependence of mode detuning on a shift  $s$  of a middle nanobeam is given in Fig. 5.8a for  $p = 1.2a$ . Here three modes become degenerate at  $s \simeq 0.4a$  with wavelength  $\lambda \simeq 3.235a$  bigger than the isolated 3D nanobeam eigenwavelength  $3.21a$ . 3D  $Q$ -factors for three coupled cavities are found to remain of the same order as the longitudinal shift is varied, see Fig. 5.8a.

Mode profiles for non-shifted system ( $s = 0$ ) are shown in Fig. 5.8b. When

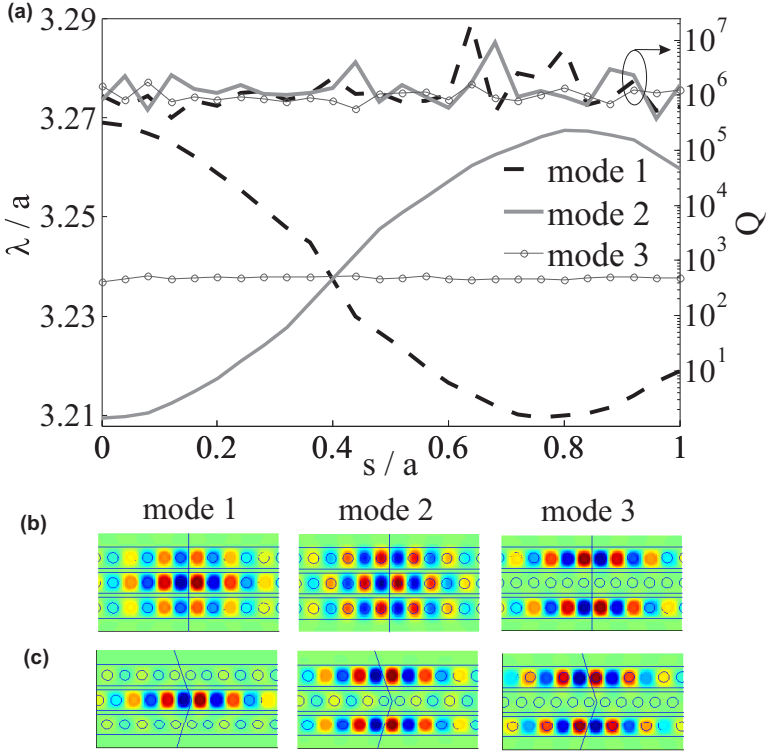


Figure 5.8: Modes in three side-coupled nanobeam cavities. The middle nanobeam is longitudinally shifted, the other two being kept stationary. Transverse separation between the neighboring nanobeams is  $p = 2.3a$ . (a)  $\lambda$  and  $Q$  of the three modes. (b)  $H_z$  profiles for the modes in the three non-shifted nanobeams. (c)  $H_z$  profiles of the degenerate modes at  $s = 0.4a$ .

symmetry planes are enforced the eigenmode profiles at the degeneracy point ( $s \simeq 0.4a$ ) look as in Fig. 5.8c. In general, in the degeneracy point we present the results of our numerical calculations based on the direct solution of Maxwell's equations and without taking linear combinations with data obtained. Our calculations for two and three nanobeams gave two variants of field maps at the degeneracy: 180° rotational (2 resonators) or reflection (3 resonators) symmetrical pictures, and profiles with field localization at individual resonators. Simulations enforcing PEC/PMC planes for the three nanobeam give degenerate modes strictly reflection-symmetrical; however we can guess that these pictures do not help in understanding physical reality better than do profiles with field localization in individual nanobeams implying complete vanishing of interaction between the cavities. And it is that characteristic degeneracy profile with field extinction in one of the cavities that is clearly

predominant in all 2D and 3D simulations for all range of separations and that should be more expectable in the experiments than other linear combination of the degenerate mode profiles.

In summary, we have shown that a longitudinal shift between side-coupled nanocavities enables flexible control of eigenmodes including the realization of exact degeneracy, a feature impossible in non-shifted resonators. The quality factor of coupled nanobeam cavities stays close to that of a single cavity, indicating good practical prospects for such structures.



# Chapter 6

## Metallic gratings

Metals exhibit a plethora of optical phenomena associated with their rich dispersion properties, and are widely used in the range from visible to GHz frequencies. Incorporating frequency-dependent permittivity for numerical modeling in the time domain is not trivial: auxiliary variables are to be introduced to account for dispersion, making transient-wave simulation of metals more complicated and memory-consuming compared to modeling of dielectric materials. Besides, time domain methods are bound to analytical description of material parameters while real-life metal permittivity might deviate significantly from that given by Drude or Drude-Lorentz expressions, so that using tabulated dispersion values becomes desirable. Finally, modeling inclined light incidence on periodic structures (gratings) is not straightforward in the time domain, and many nontrivial tricks have been proposed to work around that difficulty [119]. On the contrary, in the frequency domain no complications arise with introduction of metal dispersion, so the code preserves its same form for all types of media, and no difficulties occur for plane waves impinging on periodic structure at an arbitrary angle.

Metal-dielectric composites are intensively investigated in the optical domain, and many methods are adapted to consider various metallic geometries: from strictly analytical through hybrid semi-analytical to fully numerical finite-difference solutions. At the technologically important THz frequencies nanosstructured metals started to gain attention only recently. At extremely long wavelengths, frequency domain methods are expected to perform better than their time domain counterparts, Fig. 1.8, and in this section an emphasis is on a numerically challenging task of simulating field enhancement in single and multiple (periodic) slits in thin subwavelength films when the ratio of the grating period to the slit width reaches extremely high values of  $10^4$ . In this chapter we calculate energy transmission, reflection and absorption of gold slabs without or with perforation. At low frequencies the permittivity of gold can be defined by Eq. (1.16) with  $\epsilon_\infty = 1$ , plasma frequency  $\omega_p = 1.37 \times 10^4$  THz and  $\gamma = 40.7$  THz [159].

## 6.1 Planar metallic slab at THz frequencies

### 6.1.1 Analytic solution

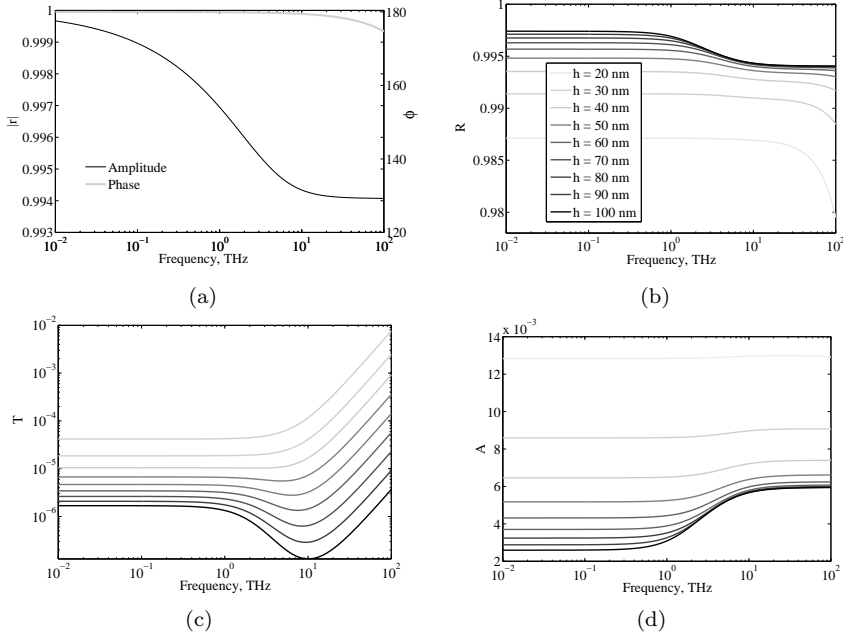


Figure 6.1: (a) Amplitude and phase of reflection at a single gold-dielectric interface; (b) reflectance, (c) transmittance and (d) absorption of gold slabs of different thickness  $h$  placed freely in the air.

Let us consider a plane subwavelength film in the THz range. Transmission, reflection and absorption of metal slab can be found through standard Fresnel's formulas with the complex permittivity of metal. The amplitude coefficient of reflection from a single interface at normal incidence is

$$r = \frac{n_1 - n_2}{n_1 + n_2}, \quad (6.1)$$

where  $n_{1,2}$  are the refractive indices of two media. From Eq. (6.1) we see that no matter from which side radiation is incident upon the boundary, the amplitude of reflected wave is the same but the phase is inverted ( $-1 = e^{i\pi}$ ). In a symmetric metal-dielectric sandwich, we have equal amplitudes of reflection from both interfaces. Figure 6.1a shows that at low frequencies single metal-dielectric interface has very high amplitude of reflection and phase shift about  $\pi$  in the whole range from  $10^{-2}$  up to  $10^2$  THz. Due to this half-period phase shift, electric field vector has the same amplitude but opposite sign upon reflection;

thus boundary conditions at the frontier of PEC and dielectric are satisfied strictly so that the radiation virtually does not enter the PEC-like metal.

We see no significant variation in reflectivity with frequency for subwavelength 20–100 nm slabs in Fig. 6.1b what is in line with Fig. 6.1a where coefficient of reflection at a single metal-dielectric interface is almost constant in the whole range of frequencies. No sign of interference effects is expected with increasing film thickness above 100 nm: they will be strongly suppressed due to such a high imaginary part of refractive index at low frequencies [160].

Even for very thin 20-nm-thick films reflectance stays very high while transmittance is suppressed, Fig. 6.1b,c. Taking into account that  $h = 20$  nm is deeply below the skin depth which is about 300–800 nm at THz (and increases very fast approaching  $\omega \rightarrow 0$ ), metal behavior similar to PEC having infinite conductivity and total reflectance irrespective of slab width is clearly seen. Utilization of skin depth at low frequencies to estimate tunneling through thin films in the same way as it is usually done at visible should be done with care. Thickness of the film should be deeply below the skin depth, just a few nanometers, for any noticeable transmission to be observed at THz.

In the visible part of spectrum the effect that very thin layers of metal can be more absorptive than bulk pieces is well known for metal-coated nanoparticles, which are intensively used in photovoltaics as providing higher absorbance than solid metal ellipsoids [92]. It turns out that not only in condition of plasmon excitation small quantities of metal can more intensively absorb radiation than bulk metal pieces: the absorption increase with reduction of slab thickness is seen in Fig. 6.1d.

Let's summarize our discussion. Huge real and imaginary parts of metal permittivity at low frequencies make perfect electric conductor description of metal nearly an ideal approximation. At THz frequencies a negligible part of radiation impinging on the metal penetrates inside. A small portion of THz wave energy passed inside the metal decays spatially slow due to skin depth increased by several times at low frequencies compared to the visible. It amounts to lower absorption per unit length experienced by non-uniform THz wave inside the metal whereas at higher frequencies significant amount of radiation tunnels effectively through the subwavelength films and can be absorbed at a higher rate. Thus at THz frequencies a 20–100 nm thick gold film becomes non-transparent and reflects most of radiation incident on it whereas, for example, 20 nm film under visible illumination can transmit up to 50% of light. Metal is indispensable material for THz range in this sense because, for example, VO<sub>2</sub> films of the same thickness experience only a 20% change in their transmission after dramatic change of refractive index from 1 to 10000 due to phase transition [161]. The ability of metal to effectively govern long-wavelength radiation on the length scale of nanometers with low absorption is of good use when we are interested in strong field concentration in air gaps in metals without sacrificing transmission.

### 6.1.2 FDFD testing

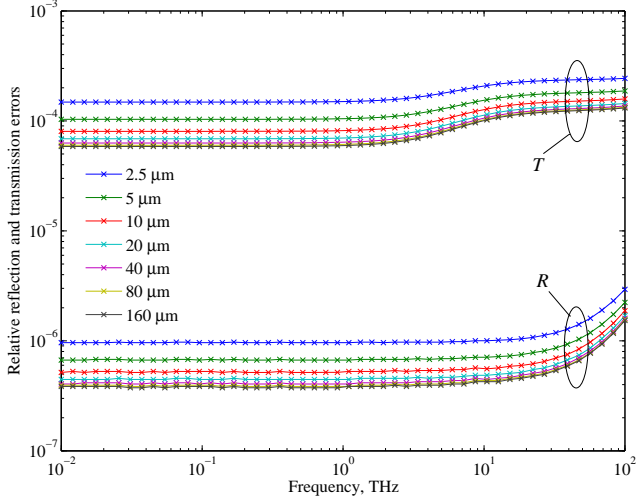


Figure 6.2: Relative error in transmission and reflection coefficients for electromagnetic radiation incident normally on the 20-nm-thick metal slab, plotted for different vertical dimensions (see the legend) of the computational domain.

Now proceed to testing of the FDFD numerical solution on the analytical problem of metallic membrane suspended in air. Figure 6.2 demonstrates the broadband accurate performance of our implementation, in particular the PMLs.

## 6.2 Single slit

Aperture films and metallic gratings have a long story of investigation in optics with well-known applications as color selective filters, photodetectors, collimators, for surface enhanced Raman scattering and fluorescence, detection of refractive index, etc. [99] Metallic nanostructures having micro- to nanometer-sized constitutive elements also have potential in lower frequencies, and homogenizable metal-dielectric composites with negative or any other desired index of refraction is not the only option here. For example, recently it was shown that a nanometer-wide single slit in a thin gold film provides strong nonresonant field enhancement at THz frequencies [159]. Metallic slabs featuring nanometer-sized perforation can be used both at visible and THz parts of spectrum what opens new prospects for these structures to be used as fast all-optical components where electromagnetic wave in one frequency range acts as a control pulse governing information signal from the other part of spectrum.

Transmission through single slits in metallic films can be strongly enhanced due to resonance effects, like cavity resonances [89, 90, 162–164] when thickness of metal film or slit width satisfy Fabry-Perot conditions. One of important aspects of these resonance effects is strong light concentration in air slits [89] that might be directly used for nonlinear applications [25]. Specially designed charge and current reservoirs can be employed for further increase of field intensities [165] where field enhancement up to 60 were achieved in the visible part of spectrum.

At THz frequencies [166] where metal behaves as PEC, enhancement due to cavity resonance effects was reported to reach the value of 430 [167]. Surprisingly high field enhancements of about  $10^3$  and higher are accumulated inside slits [159] in the regime when they act as tiny capacitors at low frequencies [168]. This regime is of particular interest in the rest of this Chapter 6. Due to capacitor model it is easier to find some laws for enhancement whereas dependencies for transmittance that does not have direct analogue in statics is somewhat more complicated to establish so the main issue is enhancement law for a single and periodic slit.

The  $p$ -polarized (i.e., electric field lies in the  $xy$  plane in the insert in Fig. 6.3) fundamental mode in the slit exists in the whole range of frequencies and thus field enhancement is possible at THz frequencies, whereas  $s$ -

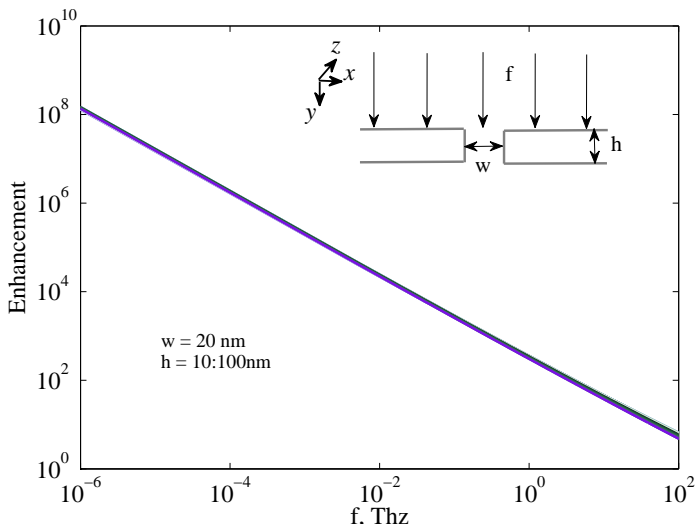


Figure 6.3: Enhancement in an isolated slit cut in slabs of different thickness taking values from 10 to 100 nm. The insert shows the geometry of the problem: single slit of width  $w$  in a gold slab of thickness  $h$  illuminated by  $p$ -polarized plane wave of frequency  $f$ . The center of coordinates lies in the center of the slit.

polarization has cut-off wavelength and at low frequencies light do not pass through the slit [99]. Here and later by enhancement we will understand the amplitude of electric field averaged over the central line of the slit (if the slit is symmetric and the film is sandwiched symmetrically, then only  $E_x$  component contributes to the enhancement thus defined) and normalized to the amplitude  $E_0$  of incident radiation:

$$\text{enhancement} = \frac{\langle E_x \rangle_{\text{slit}}|_{y=0}}{E_0} = \frac{\int_w E_x|_{y=0} dx}{w E_0} \quad (6.2)$$

This averaged  $E_x$  amplitude does not necessarily coincide with the field value in the very center of the slit, the difference being bigger for wider slits.

### 6.2.1 $1/f$ law for enhancement

We start from an isolated slit and investigate the dependence of enhancement on the slit width  $w$  and frequency  $f$ , and we compare this with the behavior of multiple slits later in this chapter. In Refs. [159, 168] it was shown theoretically and experimentally that single slit exhibits the  $1/f$  law for the field enhancement. This rule follows from a capacitor model in which field enhancement is directly proportional to the total charge accumulated on the slit edges. Thus  $1/f$  is immediately obtained as with wavelength  $\lambda$  growing, the larger part of metal is involved in gathering electrons near slit edges.

The question that now we are interested in is how good the capacitor model and the  $1/f$  law is, and how the enhancement depends on slab thickness and slit width in some reasonable bounds, i.e. before entering the regime of pronounced resonance behavior. We are also concerned with numerical method at hand: how high the enhancement can go while moving towards lower frequencies.

Figure 6.3 shows excellent fulfilment of  $1/f$  law in a broad range of frequencies; achievement of extremely high enhancements of  $10^8$  deeply below THz range, that is at MHz frequencies; and independence of the enhancement on slab thickness. In the paper [168] the authors observe some dropping of enhancement with increase of the slab width, however their enhancement is defined as a field in the center of quite large slit of 200 nm width at fixed wavelength what might explain these discrepancies in calculations.

In Fig. 6.3 at shorter wavelengths we can notice a slight spread in the development of the  $1/f$  curves for slabs of various heights. At higher frequencies possible stronger deviation from  $1/f$  law is related to shifting towards region of faster electromagnetic wave oscillations: static capacitor approximation breaks because slit dimensions become comparable to the wavelength. Thus at the frequency above  $10^2$  THz some influence of slab thickness on the enhancement might take place.

We established that enhancement is almost independent on film thickness when it is much less than the wavelength of light, and that capacitor model together with the FDFD method apparently have no limits in calculating very large field intensities in extra-narrow slits at low frequencies.

### 6.2.2 Enhancement dependence on the slit width

Field and charge accumulation can have  $1/w$  dependence on the slit width by analogy with statics [168]. In Fig. 6.4  $\lambda$ - and  $w$ -dependent enhancement is traced for several fixed slit widths. The slope of straight lines in log-log scale indicates nearly direct proportionality between the enhancement and the dimensionless parameter  $\lambda/w$  at sufficiently large ratios  $\lambda$  to  $w$  while for  $\lambda/w < 100$  the deviation from simple proportionality becomes more pronounced. Thus only in the regime when the parameters of the slit are deeply subwavelength we can talk about slit as a capacitor. More detailed inspection through curve fitting for  $\lambda/w > 10^4$  reveal that an order to which  $\lambda/w$  should be raised to give a law for the enhancement is about 0.93, i.e. very close to unity. And it appears that electrostatic approximation is not valid already for  $\lambda$  approaching hundreds of  $w$  when movement away from a straight line in Fig. 6.4 becomes visible by eye.

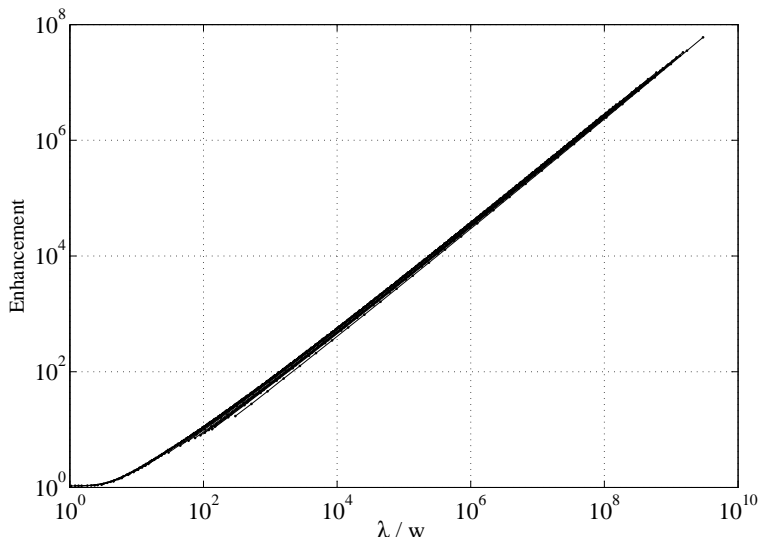


Figure 6.4: The dependence of enhancement on  $\lambda/w$  for a single slit in the 20-nm-thick gold slab. Each line is obtained by varying  $\lambda$  at some fixed slit width  $w$  so that 23 curves in total are plotted for a set of 23 slit width (taking values between  $2.9 \cdot 10^3$  nm to 10 nm). For all the curves the incident wavelength  $\lambda$  is changed from  $2.9 \cdot 10^{10}$  nm to  $2.9 \cdot 10^3$  nm corresponding to the frequency range between  $10^{-5}$  to  $10^2$  THz.

### Simulation details

For simulations of an isolated slit the buffer layers along the  $y$ -direction start right after the slab boundary and are squeezed with the  $x/(1 - x)$  function, Fig. 3.4, to computational size of  $2\text{--}3\ \mu\text{m}$ , to include more vortices of electromagnetic field around the slab, Fig. 1.4. One third of the total size of the squeeze transform layers is covered by PMLs. The same buffers are used also for the  $x$ -direction where squeezing layers include metallic plates and squeezing starts right after the slit edges. Grid steps near the slit are around  $0.1\text{--}0.4\ \text{nm}$ , being gradually stretched to reach 20 times of that for the rest of the structure, Fig. 6.5.

## 6.3 Periodic slits in metal film

Under condition of resonance excitation the transmission of light through perforated slab can be strongly prohibited [19] or, vice versa, enhanced, the former feature underpinning a well-known extraordinary optical transmission (EOT) phenomenon [95]. It turns out that for the lossless model of metal, for example the PEC model, by cutting neighboring slits around a single slit the transmission increases with increasing the number of slits, and infinite periodic structure can exhibit total transmission [88].

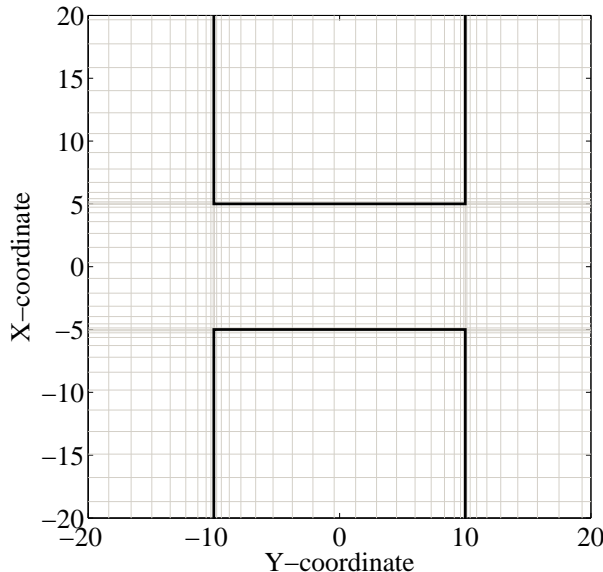


Figure 6.5: Refinement of the mesh near the metal-slit boundaries.

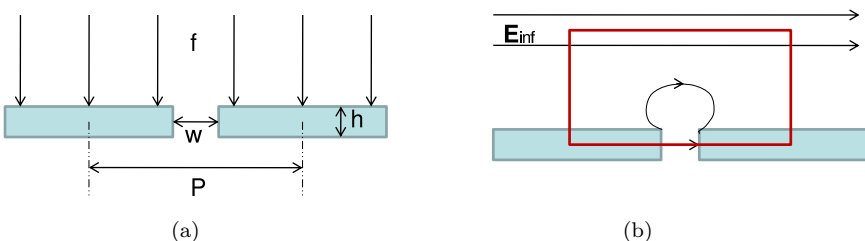


Figure 6.6: (a) Periodic grating of period  $P$  formed in gold film of thickness  $h = 20 \text{ nm}$  by perforating slits of width  $w$ . (b) Metal grating placed into static electric field; only top semi-space is shown, with external field  $E_0 = E_{\text{inf}}$  being unperturbed at infinity.

For a non-resonant case intuitive considerations let us assume that if the light is tunneled through a single slit at a certain wavelength, adding more slits might lead to higher transmittance. But what will be with the field enhancement in the slits? Will periodic structure be able to achieve the same extremely high intensities in its slits as an isolated slit does? From the capacitor model for a single slit we can estimate that the period  $P$  required to provide one of the slits in a periodic structure with charges to give the same capacitance as an isolated slit should be about or bigger than the wavelength of light [167]. But exactly at  $P = \lambda$  we have a condition for Fano resonance, which is already out of our interest. Thus we can expect that at  $\lambda < P$  condition the enhancement in the periodic structure will not exceed an isolated slit value.

In this section we consider the field enhancement in lamellar metallic gratings in the wavelength range when  $\lambda \gg h$  and  $\lambda > P$  and investigate the applicability of electrostatic approximation to propagating electromagnetic waves. Static model gives us a simple rule for electric field inside a slit as a ratio of grating period to slit width,  $P/w$ , relative to the amplitude of incident wave. It turns out that this rule can be satisfied quite generally for periodically perforated metal films starting from zero up to THz frequencies unless the grating period or film thickness becomes close to the wavelength of light, i.e. we step in the regime where resonance effects appear. In general, evolution of curves in the plots throughout this Chapter 6 is traced up till the first Rayleigh-Wood anomaly, i.e. till  $\lambda = P$ . Applicability of static model also implies total energy transfer from upper to lower half-space and thus total transmission not available in single apertures. Adding of periodic openings to metal membrane can drastically change its transmission from zero to one, what can be utilized for switching [161].

By doing numerical simulation we explore field enhancements up to  $10^4$  in a 10 nm air gap in periodic structures in 0–0.1 THz range. The combination of controllable field concentration given by simple law together with total transmission, both available in a broad range of frequencies, paves the way for usage

of metallic gratings for improvement of THz sources, detectors and sensors, as wavelength-independent polarizers and essentially for molecular absorption spectroscopy [169, 170].

### 6.3.1 10-nm-wide slit in gratings of different periods

#### Electrostatic model

As we are interested in translation of electrostatic solution to our case of transient incident fields, the width of the slab is chosen to be quite thin, i.e.  $h = 20 \text{ nm}$  everywhere in the Section 6.3. The geometry of a periodic grating is shown in Fig. 6.6a, whereas Fig. 6.6b illustrates static variant of the problem: metallic grating placed into the infinite homogeneous electric field. Let us consider this static version first. Knowing that work done by electric forces to move a test charge along closed contour in a potential field gives zero we can use this to find field in the slit by integrating along the red line in Fig. 6.6b. Periodicity requires that the field on the two red lines perpendicular to the slab spaced by  $P$  has the same vector values, what nullifies total contribution of the forces along these lines. From the rest two lines, one passing through the middle of the slab, the other one along the homogeneous field at infinity, the enhancement is derived as:

$$PE_0 - w \langle E_x \rangle_{\text{slit}} = 0 \quad (6.3a)$$

$$\langle E_x \rangle_{\text{slit}} = \frac{P}{w} E_0 \quad (6.3b)$$

Thus enhancement in periodic structures depends on the period of the grating and the size of the opening while slab thickness does not play any role in quasistatic regime. Recalling now about single slit that can be considered in Fig. 6.6b with a limiting case  $P \rightarrow \infty$  we find out that independence of single slit enhancement on the height of the slab  $h$  is a reasonable and quite expected behavior.

#### Flat enhancement

Concluding the static model, we expect to have some regime where transmittance will be unity and enhancement will obey Eq. (6.3) as follows from the static limit. Let see how this agrees with the precise numerical calculations. In Fig. 6.7 the enhancement and transmittance are plotted for gratings of varying period  $P = (2 : 1 : 10) \cdot 10^{1:1:4}$  when slit width is fixed to 10 nm. Fig. 6.7a shows that there exist broad frequency range for each of considered periods where static model conclusions work perfectly well. Enhancement equality to  $P/w$  is fulfilled with high precision for any  $P/w$  from 2 up to extreme  $10^4$ .

Threshold frequency for exiting flat enhancement region is connected with reaching  $\lambda = P$  condition. Quick dropping of enhancement curves near their ends in Fig. 6.7a signalizes about entering the region of asymmetric Fano resonance shape. For example, the period corresponding to the enhancement 10

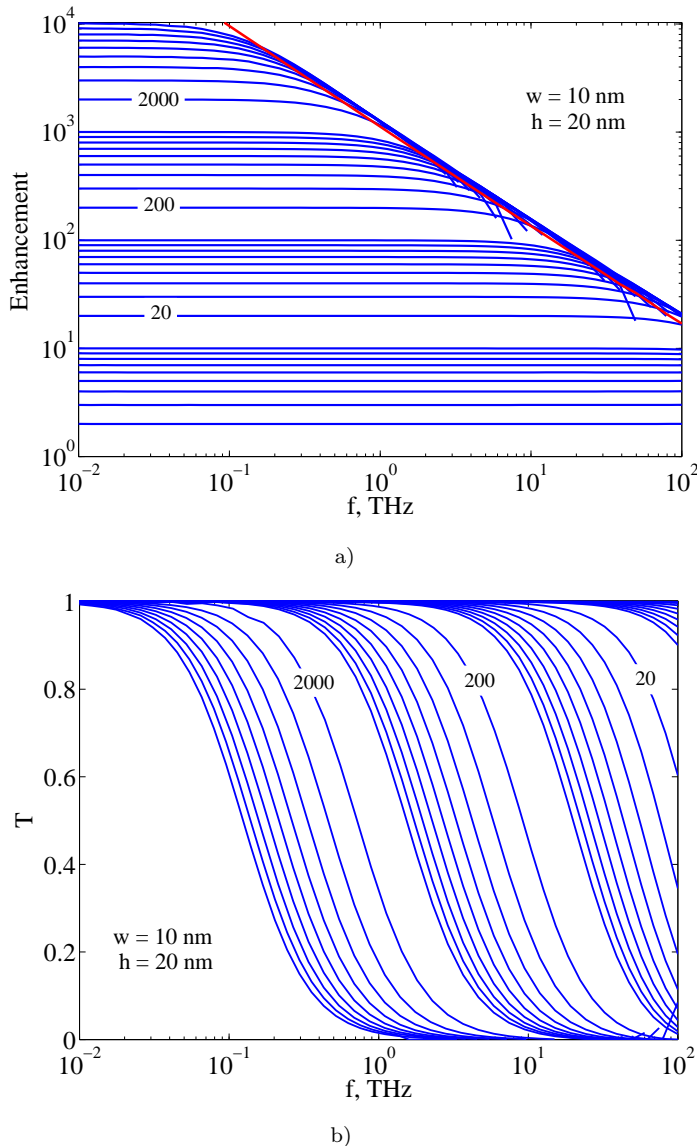


Figure 6.7: (a) Field enhancement and (b) transmittance of a 10-nm-wide slits cut in a 20-nm-thick film versus frequency for different grating periods  $P$ . The enhancements in quasi-static limit are chosen to be  $\langle E_x \rangle_{\text{slit}} / E_0 = (2 : 1 : 10) \cdot 10^{1:1:3}$ , the corresponding period of grating is  $P = w \langle E_x \rangle_{\text{slit}} / E_0$ .

is  $P = 10 \cdot w = 100$  nm what gives Rayleigh-Wood condition  $\lambda = P$  translating to  $f_{R-W} \sim 10^3$  THz and approximately one frequency order, from  $10^2$  to  $10^3$  THz, takes for the enhancement to vanish completely. From Fig. 6.7b we notice that threshold condition for transmittance is more severe, i.e. transmission dropping starts two frequency orders before the Rayleigh-Wood condition. In another example with very large enhancement of  $2 \cdot 10^3$ ,  $f_{R-W} \sim 10^1$  THz and again roughly one order less, i.e. at 1 THz, enhancement plateau regime breaks, the transmittance starting decreasing at a much smaller frequency of  $10^{-1}$  THz.

Thus by appropriate choice of geometry parameters the region with some desired enhancement and transmittance of unity can be selected. In such a zone with flat enhancement, THz pulses of short duration can be fully transmitted with all their spectral constituents experiencing the same enhancement in the near field of the gratings. As regards extremely high enhancements, for that periodic structures require very long periods and narrow slits. For many applications demanding strong field, like change of refractive index due to nonlinearity, high transmission is inessential and can be sacrificed in favor of extended frequency range of high field intensities.

### Comparison with a single-slit film

The question which system, an isolated slit or a periodic grating, can propose higher field concentrations is addressed by plotting enhancement curve for a single slit of width  $w = 10$  nm with a red line in Fig. 6.7a. As it was expected, at a fixed frequency periodic structure in general cannot accumulate bigger charge and stronger field than an isolated slit. We see an amazing correlation in behavior of the two systems: an envelope formed by enhancements in periodic structures almost coincide with single slit curve. It appears that for periodic structure we have two regimes of operation:  $\lambda \ll P$  is in deep electrostatic approximation with total transmission and flat enhancement zone obeying  $P/w$  ratio when all slits work cooperatively; if  $\lambda \rightarrow P$  cooperative action of slits splits and each slit interacts with light rather as a separate scatterer so that the enhancement in multiple slits follows the curve for isolated-slit structure. In fact even in the second regime we can anticipate that periodic grating can still preserve some coherent interaction between neighboring slits as envelope in blue color in Fig. 6.7a lies slightly higher than the red line.

In general, at a fixed incident wavelength, single or periodic apertures with a given opening width give the same highest possible enhancement and addition of more perforations with certain periodicity to a single slit can improve only total transmission.

### Threshold frequency

In general, the frequency  $f_0$  at which zone of flat enhancement ends can be approximately found from intersection of  $P/w$  horizontal with  $(\lambda/w)^{0.93 \div 1}$  line

describing a single slit. This gives very weak dependence of  $f_0$  on  $w$  while the period of the grating  $P$  essentially determines the size of enhancement plateau along the frequency axis. Because we keep slit width fixed and the period varied in a broad range of values,  $f_0$  strongly differs from curve to curve in Fig. 6.7a. If the period is close to  $P_0 \simeq c/f_0$  the enhancement in the grating becomes equal to the enhancement given by a single slit and scanning towards frequencies below  $f_0$  keeps field intensity in the grating on the same level, however further reducing the distance between neighboring slits below  $P_0$  leads to decreasing of enhancement.

### Field maps

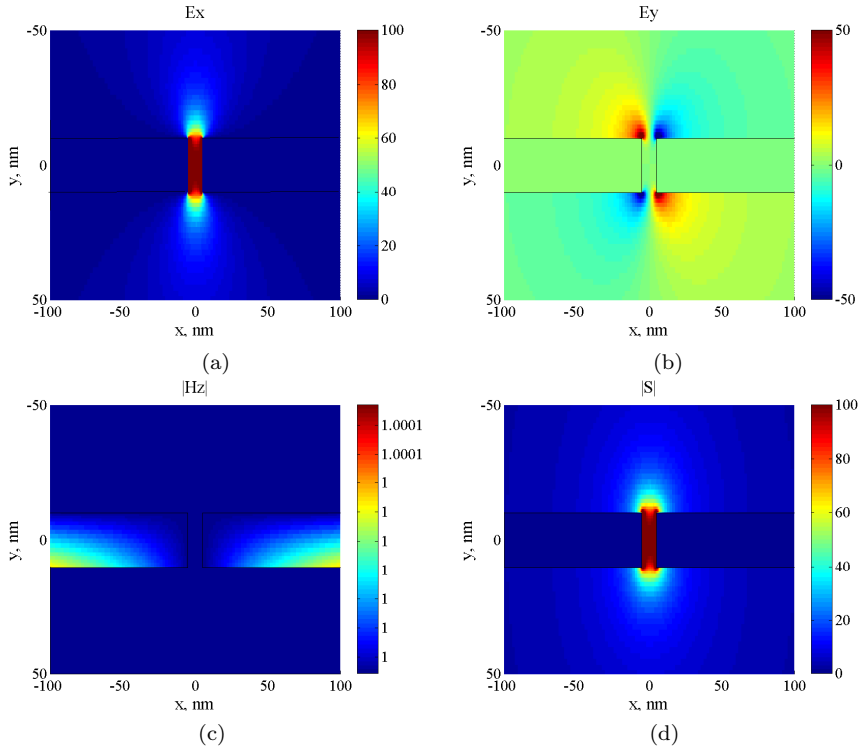


Figure 6.8: Field (a)  $E_x$ , (b)  $E_y$ , (c) modulus of  $H_z$  components and (d) modulus of Poynting vector  $\mathbf{S}$  nearby the 10-nm-wide slit in gold grating of period  $1\mu\text{m}$  at  $f = 10^{-2}\text{ THz}$ . Bounds for color maps are chosen so to show better peculiarities of field distribution.

In Fig. 6.8 spatial distributions of field components and Poynting vector characteristic for plateau zone are plotted. The  $E_x$  component (Fig. 6.8a) is strongly enhanced inside the slit with maximal amplitude reaching 200 near

the slit sharp edges. The  $E_y$  component (Fig. 6.8b) has a node at  $x = 0$  plane and antisymmetric field distribution around the node plane with strong concentration at metal corners. From intensity maps for electric components and Poynting vector it is seen that radiation couples inside the slit mainly through metallic corners. Thus the wave upon incidence on the slit passes through quite essential spatial transformations in the near field of the slit before being fully transmitted to the far field zone.

By looking at the  $H_z$  component (Fig. 6.8c) we see that magnetic field almost does not participate in electromagnetic field shaping process; its unit value through all the domain means that  $S_x = E_y \cdot H_z \simeq E_y$  and  $S_y = -E_x \cdot H_z \simeq -E_x$  thus intensity maps for Poynting vector components look similar to the electric field distributions. As seen from Fig. 6.8d, the  $S_y$  component prevails in total energy flow so that  $|\mathbf{S}|$  looks very similar to  $E_x$  field distribution.

### Simulation details

For periodic gratings in the same way as for a single slit, stretching of the finite-difference mesh reaches a ratio of 20 in most of simulations. When calculating extra-narrow slits, e.g.  $w = 10\text{ nm}$  considered in this section, integration of the field along the air gap was substituted by a point value of the field in the very center of the aperture. This is fully justified as the field along central line appears to be highly uniform in narrow slits, however grid points lying at the slit edges with zero  $E_x$  amplitude should not be included into the integral. Avoiding inclusion of such points while integrating is difficult to automate as just a few points come on the aperture.

As in the case of FDFD application to PhC resonators where calculation of  $Q$  and  $\lambda$  gave the best convergence on computational domains organized in two different ways, i.e. in the first case for better quality factor accuracy, larger domain is used even if resolution is coarse and in the second case for eigenwavelength calculations, good sampling is more important than actual domain size; for metal gratings similar different approaches can be used for calculations of transmission and enhancement. As pointed out in introduction, vortices and evanescent tails of electromagnetic field spread far away around the grating, thus correct reconstruction of energy flow and correct simulation of transmission relies heavily on big enough computational domain. In our transmittance calculations the air buffer superposed with space squeezing were taken around 2 to  $10\text{ }\mu\text{m}$ , the biggest size being utilized for extremely high enhancements generating strong evanescent fields. At the same moment calculations of enhancement are based on fine discretization and the domain can be reduced further down to  $1.5\text{ }\mu\text{m}$  in favor of sub-nanometer grid step in the region of metal-dielectric frontiers and hot spots of electromagnetic energy.

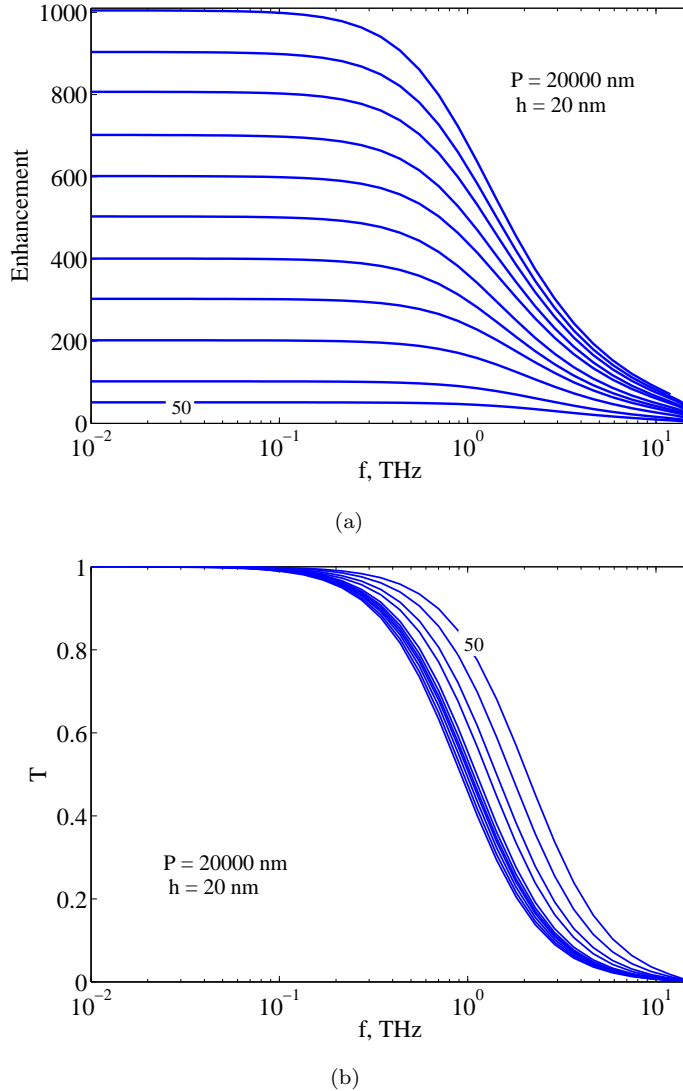


Figure 6.9: (a) Enhancement and (b) transmittance in gratings from Fig. 6.6a with unchangeable periodicity  $20 \mu\text{m}$  but with alternation of slit width according to the following approximate set of numbers: [400 200 100 67 50 40 33 29 25 22 20] which correspondingly give enhancements [50 100:100:1000] within the plateau zone.

### 6.3.2 Changing slit width when the period is fixed

In previous Section 6.3.1 we considered extra-narrow slit and going further we would like to know whether the same flat enhancement behavior holds for wider apertures. Let us now fix gold grating period  $P = 20 \mu\text{m}$  and scan over different aperture widths; because  $P$  is always kept constant Rayleigh-Wood anomaly is expected at the same frequency for different slit widths. Fig. 6.9 demonstrates that electrostatic approximation with enhancement given by  $P/w$  again works very well for broad range of slit widths, besides our additional calculations revealed that even for very wide apertures with  $w = 10 \mu\text{m}$  the enhancement factor of 2 is stably obtained. As in previous Fig. 6.7, here for narrow slits the end of enhancement plateau appears roughly one frequency order before the  $\lambda = P$  condition, with transmission falling down one more order earlier.

#### Threshold frequency

For strong field focusing, slit width should preferably be chosen quite small with the period reaching dozens or hundreds of  $\mu\text{m}$  what additionally weakens the dependence of  $f_0$  on  $w$  as compared to its dependence on  $P$ . In Fig. 6.9 threshold frequency only slightly changes from curve to curve, especially for smallest widths, in contrast to Fig. 6.7 which gives an argument for prevailing influence of  $P$  on threshold frequency. Thus if higher enhancement is required without significant reduction of plateau size, it should be better done through decrease of aperture size but not the period increase.

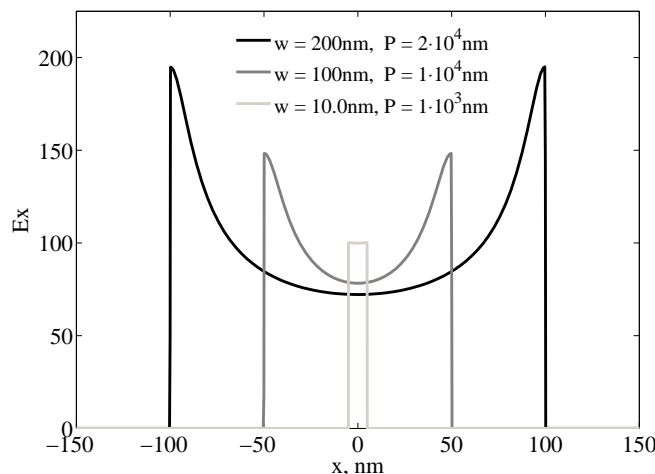


Figure 6.10: Profiles of electric field component  $E_x$ , all giving enhancements of 100, as calculated by averaging inside the slit along the  $y = 0$  line. Parameters of different gratings giving the same enhancement are shown in the legend.

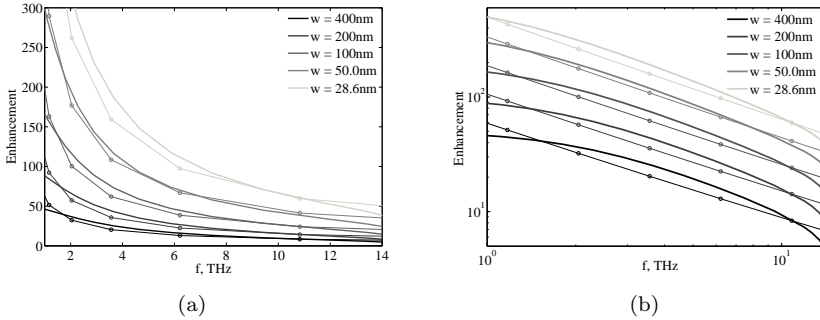


Figure 6.11: Detalization of several curves from Fig. 6.9a with linear scale (a) and logarithmic scale (b) for the enhancement, lines with circles correspond to the isolated slit and are plotted for the comparison.

### Field profiles for different slit width

To know the distribution of  $E_x$  field component along the middle line of the aperture, Fig. 6.10 compares three slit widths providing the same enhancement of one hundred calculated via Eq. 6.3. Only in the case of extremely narrow 10-nm-wide slit we see really uniform field, while opening of aperture leads to dropping of field amplitude well below the value of 100 in the central region of the slit. Thus small apertures are advantageous not only as effective energy concentrators but also for creation of uniform field.

### Comparison with a single-slit film

In Fig. 6.7 the alignment of envelopes given by single and coupled slits of different periods were obtained. In Fig. 6.11 we have a closer look at the transition region from the flat enhancement to the Rayleigh-Wood anomaly. At first glance on Fig. 6.11a, similar behavior of the two systems can be suggested; however when plotted in log-log scale, different laws for the enhancement clearly show up. Though passing in close proximity to each other, the enhancement curves for isolated and periodic slits are governed by essentially different laws. The enhancement in grating is higher in transition frequency region what can be explained by some constructive interaction of coupled slits with each other.

### Discussion

The results shown in this chapter for aperture films can be reproduced by employing the PEC model for metal instead of gold. Because of no dispersion in the PEC permittivity model and because we are interested in comparing isolated and coupled slit systems, use of  $w$ -normalized  $\lambda$ ,  $h$ ,  $P$  and a figure similar to Fig. 6.7 would be enough for complete analysis. However, both

Figs. 6.9 and 6.7 are useful for illustrative purpose so real units were preferred to dimensionless ones in our analysis.

As it was mentioned, *s*-polarized incident wave has cutoff wavelength and at low frequencies its transmission is strongly suppressed. However, additional cuts perpendicular to the slit can drastically change *s*-wave transmission [171] what makes current research also relevant for polarization other than *p*. Thus, the enhancement induced by *s*-polarized light might also be possible when metal film is perforated in a special way.

Additionally to the static model used to explain flat enhancement, we do not completely exclude the possibility that some plasmonic effects contribute to the enhancement in slits of metal gratings at long wavelengths. Although Zenneck waves, i.e. SPPs at  $f \rightarrow 0$ , are difficult to excite and detect experimentally [172], SPPs dispersion relation lies in close proximity to the light line at low frequencies, and coupling of incident radiation with electron excitation in perforated films is possible. Also, PEC model was shown to emulate plasmonic behavior: surface bound modes [99] or in other terminology spoof plasmons [173] were shown to contribute to the EOT phenomena in perforated PEC films. Because metal at long wavelengths can be described as nothing but dispersionless perfect conductor, condition for excitation of some surface bound modes is the same in the wide range of frequencies giving flat enhancement.

# Chapter 7

## Conclusion

This thesis presents the development of the finite-difference frequency-domain (FDFD) method for rigorous numerical modeling of three-dimensional nanophotonic structures. Simulation examples presented include the eigenfrequency and the  $Q$ -factor analysis of a very-high- $Q$  photonic-crystal membrane cavity, a single and coupled nanobeam resonators, and modeling of light passing through ultra-narrow slits in subwavelength metal films. Of physical significance are the following results:

(A) Coupled modes of two nanobeam cavities placed side-by-side appear to have pronounced frequency dependence on their positioning (the longitudinal shift and transversal separation), while the  $Q$ -factor of the coupled modes preserves the same order of magnitude as that of a single nanobeam. Frequency detuning of coupled modes depends nontrivially on the longitudinal shift of cavities, in particular the modes become degenerate for a certain shift. At this shift of about half the averaged lattice constant in the defect region, the magnetic field nodes in one nanobeam oppose the field lobes in the other. The degeneracy occurs for a broad range of separations between two or multiple side-coupled cavities.

(B) Lamellar metal gratings in extremely subwavelength regime exhibit total transmission of incident  $p$ -polarized radiation and strong electric field enhancement in the nanometer sized slits. With very high accuracy the enhancement equals the ratio of the grating period to the slit width, independent of the wavelength and of metal thickness if they are smaller than the wavelength of incident light. The frequency range of flat enhancement is limited by the first-order Rayleigh-Wood anomaly condition. With the period approaching but not equal to the incident wavelength, enhancement in slits of periodic gratings becomes close to that exhibited by an isolated slit.

For getting reliable  $Q$ -factors of nanophotonic resonators or transmission characteristics of metal-dielectric gratings, we addressed the minimum thickness of free space buffer layers; the possibility to further squeeze those buffer layers onto a tighter computational domain; and the nonuniform meshing

within the structure. We found that:

(I) For a given eigenmode in an open cavity a reasonable estimate for the optimal cavity-to-PML distance (in physical space) is  $\lambda/n$  — the ratio between the (expected) wavelength  $\lambda$  of that eigenmode and the refractive index contrast  $n$  between cavity material and the surrounding medium. This  $\lambda/n$  rule-of-thumb is convenient to use for automated construction of absorbing buffer layers in the finite-difference or finite-element based software.

(II) To further squeeze the cavity-to-PML distance in the computational domain, the  $x_{\text{comp}} = x_{\text{phys}}/(1 + x_{\text{phys}})$  mapping can be used. With the PMLs covering one half of the squeezed-space buffer layer (the cavity-to-PML distance in physical coordinates thus being equal to the total squeezed-space buffer size in the computational space) and comprising at least 5 grid cell sublayers, this gives robust and efficient absorbing buffers for the finite-difference simulations.

(III) Building an orthogonal, nonuniform grid of continuously varying density retains stable convergence for both  $\lambda$  and  $Q$ -factor in the eigenmode calculations, and reliable transmission and reflection coefficients when modeling extremely subwavelength metal gratings while saving computer memory and calculation time a lot. Grids with the ratios in the step size reaching 1:10 and more were investigated.

Applying these findings to real-life modeling leads to considerable computation time and memory savings. For example, squeezing the outer free space reduces the computational domain size, roughly, twofold along each of the squeezed coordinates. For metal-dielectric structures, nonuniform grid is essential to describe material interfaces, especially sharp metal edges and field singularities around them, more precisely. For ultra-high- $Q$  photonic-crystal cavities, at a quite coarse sampling of 30 pixels per  $\lambda$  in the region of high field intensity, the error in the eigenwavelength is well below 0.5% and the  $Q$ -factor order of magnitude can easily be obtained on a laptop computer with 4 Gb of RAM and 2.2 GHz CPU frequency in about 5 to 10 minutes.

# Appendix A

## Fourier transformation

### A.1 Continuous Fourier transformation

Let us start from the continuous Fourier transformation (FT). Frequency spectrum of a mode in a fixed point is given by the Fourier transformation of a time-dependent signal:

$$A(\omega) = \int_0^{+\infty} A_0 e^{-\frac{\omega_0 t}{2Q}} e^{-i\omega_0 t} e^{-i\omega t} dt = \int_0^{+\infty} y(t) dt \quad (\text{A.1})$$

For a signal represented by a complex value we will get well known lorentzian. However, if the signal is written as purely real then its FT differs from lorentzian. In Table A.1 there are examples of FT of different signals: complex and real (with different starting phase  $\varphi_0$ ) according to [174]. In Fig. A.1 we check the difference in normalized on maximum FT of these signals and find that it is insignificant was expected. However note, that there are still small difference in position of peaks for  $|f_{cos}|^2$  and  $|f_{sin}|^2$ . Besides, lorentzian fitting by least square procedures in MatLab (lsqcurvefit) and Mathematica (FindFit, NonlinearFit) is very dependent and sensitive to number of points involved and guess

function	FT
$y_{exp}(t < 0) = 0$ $y_{exp}(t > 0) = e^{i\omega_0 t} e^{-at}$	$f_{exp}(\omega) = \frac{1}{i(\omega - \omega_0) + a}$
$y_{cos}(t < 0) = 0$ $y_{cos}(t > 0) = \cos(\omega_0 t) e^{-at}$	$f_{cos}(\omega) = \frac{a(a^2 + \omega^2 + \omega_0^2) - i\omega(a^2 + \omega^2 - \omega_0^2)}{(a^2 + \omega_0^2 - \omega^2)^2 + 4a^2\omega^2}$
$y_{sin}(t < 0) = 0$ $y_{sin}(t > 0) = \sin(\omega_0 t) e^{-at}$	$f_{sin}(\omega) = \frac{\omega_0}{(a^2 + \omega_0^2 - \omega^2) + i2a\omega}$

Table A.1: Fourier transformation of some signals [174].

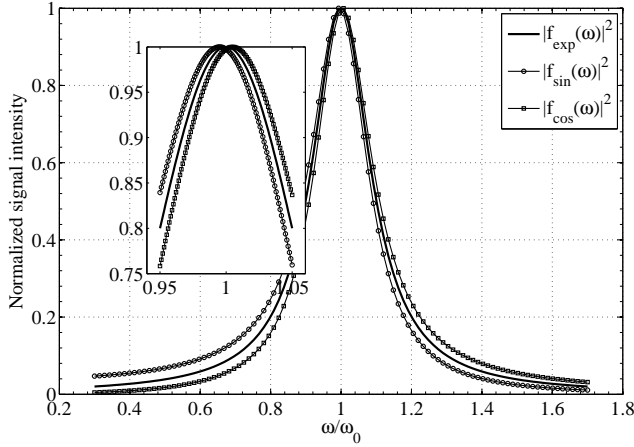


Figure A.1: Normalized to the maximum squared absolute values of functions in the right column of table A.1.

parameters to make fit. This simple consideration supports the fact that it is common to talk about approximate value of the  $Q$ -factor.

## A.2 Discrete Fourier transformation

The discrete Fourier transformation (DFT) is defined as follows:

$$f(\omega_k) = \sum_{n=0}^{N-1} y(t_n) e^{-i\omega_k t_n}, \quad k = 0, 1, 2, \dots, N - 1 \quad (\text{A.2})$$

where  $y(t_n)$  discretized with step  $\Delta t$ , total signal length in time domain is  $N\Delta t$ ,  $f(\omega_n)$  - signal in the frequency domain after DFT of signal, step in frequency  $2\pi/N\delta t$ . Then frequency points are defined as

$$\omega_k = k \frac{2\pi}{N\delta t}, \quad k = 0, 1, 2, \dots, N - 1 \quad (\text{A.3})$$

In Mathematica Eq. A.3 can be used to find resonance frequency, while in Matlab frequency sampling is shifted on one step backwards, i.e. DFT and inverse DFT are initially summed starting from unity in Eq. A.2. Then the frequency points in Matlab are:

$$\omega_k = (k - 1) \frac{2\pi}{N\delta t}, \quad k = 1, 2, \dots, N \quad (\text{A.4})$$

## Appendix B

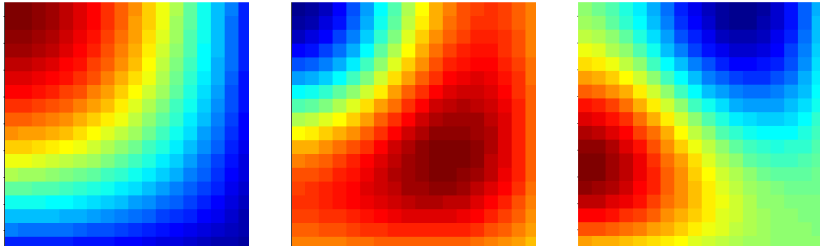
# Fabry-Perot resonator: FEM versus FDFD performance

The eigenwavelength of a rectangular metallic cavity of the lateral size  $a$  and  $b$  can be written as:

$$\lambda = \frac{2}{\sqrt{\left(\frac{m}{a}\right)^2 + \left(\frac{n}{b}\right)^2}} \quad (\text{B.1})$$

FEM is a direct competitor of the FDFD technique. We compare results of the 2D in-house Fortran-based FEM and Matlab-based FDFD methods in Table B.1 for  $a = b = 10$  where a quarter of the cavity (of size  $5 \times 5$ ) is discretized with quite rough resolution of  $19 \times 19$  rectangular cells in both cases, Fig. B.1a. The iterative procedure to find eigenvalues is home-made with maximal number of iteration being fixed to 500; the iteration cycle finishes before reaching 500 loops if norma of the eigenvalues difference between current and previous iteration is less or equal to the residual  $10^{-12}$ .

From the Table B.1 we see that convergence rate (i.e. maximal number of iterations) for both methods are similar. The FDFD mistake for the first fundamental modes is found to be twice larger than that for the FEM calculations, however for modes of higher orders FDFD and FEM performance become similar. The home-made formulation of the FEM gives discrepancy between the eigenvalues of the degenerate modes (commercial software Ansoft [175] does not have this problem; in general it gives relative errors comparable with our home-made FEM realization) while the FDFD degenerate eigenvalues coincide with accuracy up to 5<sup>th</sup> digit. FEM-solution time is longer because of necessity of many-loops cycles to operate with each element when doing matrix multiplication to solve generalized eigenvalue problem.



(a)

			[19x19] elements		[19x19] Yee cells	
	(l,m)	analytic $\lambda$	FEM/ error %	iterations/ residual	FDFD/ error %	iterations/ residual
1	(1,1)	14.1421	14.1447	18	14.1460	18
			<b>0.0179</b>	$4.7 \times 10^{-13}$	<b>0.0270</b>	$5.3 \times 10^{-13}$
2	(1,3)	6.3246	6.3158	500	6.3386	45
			<b>-0.1381</b>	$1.6 \times 10^{-12}$	<b>0.2220</b>	$6.2 \times 10^{-13}$
3	(3,1)	6.3246	6.3099	79	6.3386	101
			<b>-0.2325</b>	$1.0 \times 10^{-12}$	<b>0.2220</b>	$6.9 \times 10^{-13}$
4	(3,3)	4.7140	4.7044	75	4.7255	78
			<b>-0.2056</b>	$6.9 \times 10^{-13}$	<b>0.2437</b>	$7.2 \times 10^{-13}$
5	(1,5)	3.9223	3.8996	500	3.9480	94
			<b>-0.5804</b>	$6.1 \times 10^{-12}$	<b>0.6538</b>	$9.7 \times 10^{-13}$
6	(5,1)	3.9223	3.8957	169	3.9480	213
			<b>-0.6777</b>	$8.5 \times 10^{-13}$	<b>0.6538</b>	$9.4 \times 10^{-13}$

(b)

Figure B.1: (a) Field for the first (left) and degenerate second (middle) and third (right) modes in a quarter of the metallic cavity. (b) Table comparing resonance wavelength and relative errors given by the FEM and FDFFD approaches as well as total number of iterations and residuals at the last iteration.

# Bibliography

- [1] E. Ozbay, “Plasmonics: merging photonics and electronics at nanoscale dimensions,” *Science*, vol. 311, pp. 189–193, 2006.
- [2] S. A. Ramakrishna, “Physics of negative refractive index materials,” *Reports on Progress in Physics*, vol. 68, pp. 449–521, 2005.
- [3] D. K. Gramotnev and S. Bozhevolnyi, “Plasmonics beyond the diffraction limit,” *Nature Photonics*, vol. 4, pp. 83–91, 2009.
- [4] J. Zhao, P. Belov, and Y. Hao, “Subwavelength internal imagine by means of a wire medium,” *Journal of Optics A: Pure and Applied Optics*, vol. 11, p. 075101, 2009.
- [5] N. Kundtz and D. R. Smith, “Extreme-angle broadband metamaterial lens,” *Nature Materials*, vol. 9, pp. 129–132, Feb. 2010.
- [6] X. Zhang, “Electromagnetic waves in 2d photonic crystals,” *Materials Today*, vol. 12, pp. 44–51, 2009.
- [7] I. M. Vellekoop, A. Lagendijk, and A. P. Mosk, “Exploiting disorder for perfect focusing,” *Nature Photonics*, vol. 4, no. February, pp. 320–322, 2010.
- [8] J. Valentine, J. Li, T. Zentgraf, G. Bartal, and X. Zhang, “An optical cloak made of dielectrics,” *Nature Materials*, vol. 8, pp. 568–571, July 2009.
- [9] J. Zhang, Y. Luo, and N. A. Mortensen, “Minimizing the scattering of a nonmagnetic cloak,” *Applied Physics Letters*, vol. 96, p. 113511, 2010.
- [10] L. H. Gabrielli, J. Cardenas, C. B. Poitras, and M. Lipson, “Silicon nanosstructure cloak operating at optical frequencies,” *Nature*, vol. 3, pp. 461–463, July 2009.
- [11] X. Chen, Y. Luo, J. Zhang, K. Jiang, J. B. Pendry, and S. Zhang, “Macroscopic invisibility cloaking of visible light,” *Nature Communications*, vol. 2, pp. 1–6, Feb. 2011.

- [12] M. Paniccia and N. Photonics, “Integrating silicon photonics,” *Nature Photonics*, vol. 4, pp. 498–499, Aug. 2010.
- [13] H.-W. Hübers, “Terahertz technology: Towards THz integrated photonics,” *Nature Photonics*, vol. 4, pp. 503–504, Aug. 2010.
- [14] M. Ferrera, Y. Park, L. Razzari, B. E. Little, S. T. Chu, R. Morandotti, D. J. Moss, and J. Azaña, “On-chip CMOS-compatible all-optical integrator,” *Nature Communications*, vol. 1, pp. 1–5, June 2010.
- [15] D. Weinstein and S. A. Bhave, “The resonant body transistor,” *Nano Letters*, vol. 10, pp. 1234–1237, Apr. 2010.
- [16] C. C. Bof Bufon, J. D. Cojal Gonzalez, D. J. Thurmer, D. Grimm, M. Bauer, and O. G. Schmidt, “Self-assembled ultra-compact energy storage elements based on hybrid nanomembranes,” *Nano Letters*, vol. 10, pp. 2506–2510, June 2010.
- [17] J. Leuthold, C. Koos, and W. Freude, “Nonlinear silicon photonics,” *Nature Photonics*, vol. 4, pp. 535–544, July 2010.
- [18] G. Robb, “Nanophotonics: free electrons get light out of a hole,” *Nature Nanotechnology*, vol. 4, pp. 707–708, Nov. 2009.
- [19] S. Xiao, V. P. Drachev, A. V. Kildishev, X. Ni, U. K. Chettiar, H.-K. Yuan, and V. M. Shalaev, “Loss-free and active optical negative-index metamaterials,” *Nature*, vol. 466, pp. 735–738, Aug. 2010.
- [20] H.-T. Chen, W. J. Padilla, M. J. Cich, A. K. Azad, R. D. Averitt, and A. J. Taylor, “A metamaterial solid-state terahertz phase modulator,” *Nature Photonics*, vol. 3, pp. 148–151, 2009.
- [21] G. T. Reed, G. Mashanovich, F. Y. Gardes, and D. J. Thomson, “Silicon optical modulators,” *Nature Photonics*, vol. 4, pp. 518–526, July 2010.
- [22] F. Lopez-Tejeiro, S. G. Rodrigo, L. Martin-Moreno, F. J. Garcia-Vidal, E. Devaux, T. W. Ebbesen, J. R. Krenn, I. Radko, S. I. Bozhevolnyi, M. U. Gonzalez, J. C. Weber, and A. Dereux, “Efficient unidirectional nanoslit couplers for surface plasmons,” *Nature Physics*, vol. 3, pp. 324–328, 2007.
- [23] T. Kosako, Y. Kadoya, and H. F. Hofmann, “Directional control of light by a nano-optical Yagi Uda antenna,” *Nature Photonics*, vol. 4, pp. 312–315, March 2010.
- [24] S. Mingaleev, A. Miroshnichenko, Y. Kivshar, and K. Busch, “All-optical switching, bistability, and slow-light transmission in photonic crystal waveguide-resonator structures,” *Physical Review E*, vol. 74, p. 046603, Oct. 2006.

- [25] S. Carretero-Palacios, A. Minovich, D. N. Neshev, Y. S. Kivshar, F. J. Garcia-Vidal, L. Martin-Moreno, and S. G. Rodrigo, “Optical switching in metal-slit arrays on nonlinear dielectric substrates,” *Optics Letters*, vol. 35, pp. 4211–4213, Dec. 2010.
- [26] A. J. Shields, “Semiconductor quantum light sources,” *Nature Photonics*, vol. 1, pp. 215–223, Apr. 2007.
- [27] A. Fratalocchi, “Mode-locked lasers: Light condensation,” *Nature Photonics*, vol. 4, pp. 502–503, Aug. 2010.
- [28] D. Liang and J. E. Bowers, “Recent progress in lasers on silicon,” *Nature Photonics*, vol. 4, pp. 511–517, July 2010.
- [29] P. Q. Liu, A. J. Hoffman, M. D. Escarra, K. J. Franz, J. B. Khurgin, Y. Dikmelik, X. Wang, J.-y. Fan, and C. F. Gmachl, “Highly power-efficient quantum cascade lasers,” *Nature Photonics*, vol. 4, no. February, pp. 262–265, 2010.
- [30] H. J. Caulfield and S. Dolev, “Why future supercomputing requires optics,” *Nature Photonics*, vol. 4, pp. 261–263, May 2010.
- [31] A. H. J. Yang, S. D. Moore, B. S. Schmidt, M. Klug, M. Lipson, and D. Erickson, “Optical manipulation of nanoparticles and biomolecules in subwavelength slot waveguides,” *Nature*, vol. 457, pp. 71–75, 2009.
- [32] M. Celebrano, P. Kukura, A. Renn, and V. Sandoghdar, “Single-molecule imaging by optical absorption,” *Nature Photonics*, pp. 95–98, January 2011.
- [33] J. Zhu, C.-M. Hsu, Z. Yu, S. Fan, and Y. Cui, “Nanodome solar cells with efficient light management and self-cleaning,” *Nano Letters*, vol. 10, pp. 1979–1984, June 2010.
- [34] A. P. Kulkarni, K. M. Noone, K. Munechika, S. R. Guyer, and D. S. Ginger, “Plasmon-enhanced charge carrier generation in organic photovoltaic films using silver nanoprisms,” *Nano Letters*, vol. 10, pp. 1501–1505, Apr. 2010.
- [35] D. Graham-Rowe, “Solar-powered lasers,” *Nature Photonics*, vol. 4, pp. 64–65, Feb. 2010.
- [36] D. Cyranoski, “Seeing the light,” *Nature*, vol. 94, p. 726, 2003.
- [37] N. Horiuchi, “Light-emitting diodes: Natural white light,” *Nature Photonics*, vol. 4, p. 738, November 2010.
- [38] J. C. Knight, “Photonic crystal fibres,” *Nature*, vol. 424, pp. 847–851, Aug. 2003.

- [39] O. Graydon, "Biophotonics: Fluidic camera aids surgery," *Nature Photonics*, vol. 4, p. 585, Sept. 2010.
- [40] N. I. Smith, "Biophotonics: A light to move the heart," *Nature Photonics*, vol. 4, pp. 587–589, Sept. 2010.
- [41] J. D. Joannopoulos, S. G. Johnson, J. N. Winn, and R. D. Meade, *Photonic Crystals: Molding the Flow of Light*. Princeton Univ. Press, 2001.
- [42] K. Hennessy, a. Badolato, M. Winger, D. Gerace, M. Atatüre, S. Gulde, S. Fält, E. L. Hu, and a. Imamoglu, "Quantum nature of a strongly coupled single quantum dot-cavity system," *Nature*, vol. 445, pp. 896–899, Feb. 2007.
- [43] V. Rao and S. Hughes, "Single quantum dot spontaneous emission in a finite-size photonic crystal waveguide: Proposal for an efficient chip single photon gun," *Physical Review Letters*, vol. 99, p. 193901, Nov. 2007.
- [44] T. Yoshie, A. Scherer, J. Hendrickson, G. Khitrova, H. M. Gibbs, G. Rupper, C. Ell, O. B. Shchekin, and D. G. Deppe, "Vacuum Rabi splitting with a single quantum dot in a photonic crystal nanocavity," *Nature*, vol. 432, pp. 9–12, November 2004.
- [45] J. D. Jackson, *Classical Electrodynamics*. Englewood Cliffs: John Wiley & Sons Inc., 3d ed., 1999.
- [46] H. A. Haus, *Waves and Fields in Optoelectronics*. Englewood Cliffs, New Jersey: Prentice-Hall Inc., 1984.
- [47] H. A. Sakoda, *Optical Properties of Photonic Crystals*. Germany: Springer, 2001.
- [48] J. M. Gerard and B. Gayral, "InAs quantum dots: articial atoms for solid-state cavity-quantum electrodynamics," *Physica E*, vol. 9, pp. 131–139, 2001.
- [49] B.-S. Song, S.-W. Jeon, and S. Noda, "Symmetrically glass-clad photonic crystal nanocavities with ultrahigh quality factors," *Optics Letters*, vol. 36, pp. 91–93, Jan. 2011.
- [50] K. J. Vahala, "Optical microcavities," *Nature*, vol. 424, pp. 839–846, Aug. 2003.
- [51] S. Noda, M. Fujita, and T. Asano, "Spontaneous-emission control by photonic crystals and nanocavities," *Nature Photonics*, vol. 1, pp. 449–458, Aug. 2007.
- [52] K. Aoki, D. Guimard, M. Nishioka, M. Nomura, S. Iwamoto, and Y. Arakawa, "Coupling of quantum-dot light emission with a three-dimensional photonic-crystal nanocavity," *Nature Photonics*, vol. 2, pp. 688–692, Oct. 2008.

- [53] Y. Zhang, M. W. McCutcheon, I. B. Burgess, and M. Loncar, "Ultra-high-Q TE/TM dual-polarized photonic crystal nanocavities," *Optics Letters*, vol. 34, pp. 2694–2696, Sept. 2009.
- [54] B.-S. Song, S. Noda, T. Asano, and Y. Akahane, "Ultra-high-Q photonic double-heterostructure nanocavity," *Nature Materials*, vol. 4, pp. 207–210, Feb. 2005.
- [55] Z. Zhang and M. Qiu, "Small-volume waveguide-section high Q microcavities in 2D photonic crystal slabs," *Optics Express*, vol. 12, pp. 3988–3995, Aug. 2004.
- [56] O. Painter, J. Vučković, and A. Scherer, "Defect modes of a two-dimensional photonic crystal in an optically thin dielectric slab," *Journal of the Optical Society of America B*, vol. 16, pp. 275–285, Feb. 1999.
- [57] Z. Zhang and M. Qiu, "Small-volume waveguide-section high Q microcavities in 2D photonic crystal slabs," *Optics Express*, vol. 12, pp. 3988–3995, Aug. 2004.
- [58] P. L. C. Sauvan, G. Lecamp and J. P. Hugonin, "Modal-reflectivity enhancement by geometry tuning in photonic crystal microcavities," *Optics Express*, vol. 13, pp. 245–255, 2004.
- [59] Y. Tanaka, T. Asano, and S. Noda, "Design of photonic crystal nanocavity with Q equal to  $10^9$ ," *Journal of Lightwave Technology*, vol. 26, pp. 1532–1539, June 2008.
- [60] Y. Gong, B. Ellis, G. Shambat, T. Sarmiento, J. S. Harris, and J. Vuckovic, "Nanobeam photonic crystal cavity quantum dot laser," *Optics Express*, vol. 18, pp. 8781–8789, Apr. 2010.
- [61] S.-H. Kim, S.-K. Kim, and Y.-H. Lee, "Vertical beaming of wavelength-scale photonic crystal resonators," *Physical Review B*, vol. 73, p. 235117, June 2006.
- [62] P. B. Deotare, M. W. McCutcheon, I. W. Frank, M. Khan, and M. Loncar, "High quality factor photonic crystal nanobeam cavities," *Applied Physics Letters*, vol. 94, pp. 121106–3, 2009.
- [63] M. Eichenfield, R. Camacho, J. Chan, K. J. Vahala, and O. Painter, "A picogram- and nanometre-scale photonic-crystal optomechanical cavity," *Nature*, vol. 459, pp. 550–555, May 2009.
- [64] Q. Lin, J. Rosenberg, D. Chang, R. Camacho, M. Eichenfield, and K. J. Vahala, "Nano-optomechanical structures," *Nature*, vol. 4, pp. 236–242, April 2010.

- [65] N.-V.-Q. Tran, S. Combrié, and A. De Rossi, “Directive emission from high-Q photonic crystal cavities through band folding,” *Physical Review B*, vol. 79, p. 041101, Jan. 2009.
- [66] A. Mock, J. D. O. Brien, and S. Member, “Strategies for reducing the out-of-plane radiation in photonic crystal heterostructure microcavities for continuous wave laser applications,” *Journal of Lightwave Technology*, vol. 28, no. 7, pp. 1042–1050, 2010.
- [67] Y. Chassagneux, R. Colombelli, W. Maineult, S. Barbieri, H. E. Beere, D. a. Ritchie, S. P. Khanna, E. H. Linfield, and a. G. Davies, “Electrically pumped photonic-crystal terahertz lasers controlled by boundary conditions,” *Nature*, vol. 457, pp. 174–178, Jan. 2009.
- [68] Y. Kurosaka, S. Iwahashi, Y. Liang, K. Sakai, E. Miyai, W. Kuniishi, D. Ohnishi, and S. Noda, “On-chip beam-steering photonic-crystal lasers,” *Engineering*, vol. 4, pp. 447–450, July 2010.
- [69] C. Yan, Q. J. Wang, L. Diehl, M. Hentschel, J. Wiersig, N. Yu, C. Pfugl, F. Capasso, M. A. Belkin, T. Edamura, M. Yamanishi, and H. Kan, “Directional emission and universal far-field behavior from semiconductor lasers with limacon-shaped microcavity,” *Applied Physics Letters*, vol. 94, no. 25, p. 251101, 2009.
- [70] A. Yariv, Y. Xu, R. K. Lee, and A. Scherer, “Coupled-resonator optical waveguide: a proposal and analysis,” *Optics Letters*, vol. 24, pp. 711–3, June 1999.
- [71] D. Gerace, H. E. Türeci, A. Imamoglu, V. Giovannetti, and R. Fazio, “The quantum-optical Josephson interferometer,” *Nature Physics*, vol. 5, pp. 281–284, Mar. 2009.
- [72] D. G. Angelakis, L. Dai, and L. C. Kwek, “Coherent control of long-distance steady-state entanglement in lossy resonator arrays,” *Europhysics Letters*, vol. 91, p. 10003, July 2010.
- [73] K. A. Atlasov, M. Felici, K. F. Karlsson, P. Gallo, A. Rudra, B. Dwir, and E. Kapon, “1D photonic band formation and photon localization in finite-size photonic-crystal waveguides,” *Optics Express*, vol. 18, pp. 117–22, Jan. 2010.
- [74] F. Intonti, S. Vignolini, F. Riboli, M. Zani, D. S. Wiersma, L. Balet, L. H. Li, M. Francardi, A. Gerardino, A. Fiore, and M. Gurioli, “Tuning of photonic crystal cavities by controlled removal of locally infiltrated water,” *Applied Physics Letters*, vol. 95, no. 17, p. 173112, 2009.
- [75] H. Altug, D. Englund, and J. Vuckovic, “Ultrafast photonic crystal nanocavity laser,” *Nature physics*, vol. 2, pp. 484–488, 2006.

- [76] A. E. Miroshnichenko, S. Flach, and Y. S. Kivshar, “Fano resonances in nanoscale structures,” *Reviews of Modern Physics*, vol. 82, pp. 2257–2298, 2010.
- [77] B. Cluzel, K. Foubert, L. Lalouat, J. Dellinger, D. Peyrade, E. Picard, E. Hadji, and F. de Fornel, “Addressable subwavelength grids of confined light in a multislotted nanoresonator,” *Applied Physics Letters*, vol. 98, no. 8, p. 081101, 2011.
- [78] T. Baba, “Slow light in photonic crystals,” *Nature Photonics*, vol. 2, pp. 465–473, Aug. 2008.
- [79] J. D. Domenech, P. Munoz, and J. Capmany, “Transmission and group-delay characterization of coupled resonator optical waveguides apodized through the longitudinal offset technique,” *Optics Letters*, vol. 36, pp. 136–8, Jan. 2011.
- [80] S. Mookherjea and A. Yariv, “Optical pulse propagation and holographic storage in a coupled-resonator optical waveguide,” *Physical Review E*, vol. 64, p. 066602, Nov. 2001.
- [81] S. Mookherjea and A. Yariv, “Second-harmonic generation with pulses in a coupled-resonator optical waveguide,” *Physical Review E*, vol. 65, p. 026607, Jan. 2002.
- [82] S. Vignolini, F. Riboli, F. Intonti, D. S. Wiersma, L. Balet, L. H. Li, M. Francardi, A. Gerardino, A. Fiore, and M. Gurioli, “Mode hybridization in photonic crystal molecules,” *Applied Physics Letters*, vol. 97, no. 6, p. 063101, 2010.
- [83] M. Bayer, T. Gutbrod, J. Reithmaier, A. Forchel, T. Reinecke, P. Knipp, A. Dremin, and V. Kulakovskii, “Optical modes in photonic molecules,” *Physical Review Letters*, vol. 81, pp. 2582–2585, Sept. 1998.
- [84] S.-l. Qiu and Y.-p. Li, “Q-factor instability and its explanation in the staircased FDTD simulation of high-Q circular cavity,” *Journal of Optical Society of America A*, vol. 26, no. 9, pp. 1664–1674, 2009.
- [85] “Crystal Wave.” <http://www.photond.com/products/fdtd/fdtd01.htm?2>.
- [86] “CST Microwave Studio.” [http://www.cst.com/Content/Documents/Articles/article501/Characterization\\_of\\_Photonic\\_Structures\\_with\\_CST\\_Microwave\\_Studio.pdf](http://www.cst.com/Content/Documents/Articles/article501/Characterization_of_Photonic_Structures_with_CST_Microwave_Studio.pdf).
- [87] M. D. Arnold, M. G. Blaber, M. J. Ford, and N. Harris, “Universal scaling of local plasmons in chains of metal spheres,” *Optics Express*, vol. 18, pp. 7528–42, Mar. 2010.

- [88] A. Fernández-Domínguez, F. García-Vidal, and L. Martín-Moreno, “Resonant transmission of light through finite arrays of slits,” *Physical Review B*, vol. 76, p. 235430, Dec. 2007.
- [89] J. Bravo-Abad, L. Martín-Moreno, and F. García-Vidal, “Transmission properties of a single metallic slit: From the subwavelength regime to the geometrical-optics limit,” *Physical Review E*, vol. 69, p. 026601, Feb. 2004.
- [90] R. Gordon, “Light in a subwavelength slit in a metal: Propagation and reflection,” *Physical Review B*, vol. 73, p. 153405, Apr. 2006.
- [91] C. F. Boren and D. R. Huffman, *Absorption and Scattering of Light by Small Particles*. New York: John Wiley and Sons Inc., 1983.
- [92] C. Hagglund, S. P. Apell, and B. Kasemo, “Maximized optical absorption in ultrathin films and its application to plasmon-based two-dimensional photovoltaics,” *Nano Letters*, vol. 10, pp. 3135–3141, july 2010.
- [93] A. Ishimaru, *Wave Propagation and Scattering in Random Media*. NY: Academic Press, 2 ed., 1978.
- [94] R. Wannemacher, M. Quinten, and a. Pack, “Evanescent-wave scattering in near-field optical microscopy,” *Journal of Microscopy*, vol. 194, pp. 260–264, 1999.
- [95] T. Ebbesen, H. J. Lezec, H. F. Ghaemi, T. Thio, and P. A. Wolff, “Extraordinary optical transmission through sub-wavelength hole arrays,” *Nature*, vol. 391, pp. 667–669, 1998.
- [96] V. R. Almeida, Q. Xu, C. a. Barrios, and M. Lipson, “Guiding and confining light in void nanostructure,” *Optics Letters*, vol. 29, pp. 1209–11, June 2004.
- [97] R. F. Oulton, V. J. Sorger, D. A. Genov, D. F. P. Pile, and X. Zhang, “A hybrid plasmonic waveguide for subwavelength confinement and long-range propagation,” *Nature Photonics*, vol. 2, pp. 496–500, July 2008.
- [98] M. Fujii, J. Leuthold, and W. Freude, “Dispersion relation and loss of sub-wavelength confined mode of metal-dielectric-gap optical waveguides,” *IEEE Photonics Technology Letters*, vol. 21, pp. 362–364, Mar. 2009.
- [99] F. J. Garcia-Vidal, T. W. Ebbesen, and L. Kuipers, “Light passing through subwavelength apertures,” *Reviews of Modern Physics*, vol. 82, pp. 729–787, Mar. 2010.
- [100] H. Schouten, T. Visser, D. Lenstra, and H. Blok, “Light transmission through a subwavelength slit: Waveguiding and optical vortices,” *Physical Review E*, vol. 67, pp. 036608–1–4, Mar. 2003.

- [101] H. Schouten, T. Visser, G. Gbur, D. Lenstra, and H. Blok, “Connection between phase singularities and the radiation pattern of a slit in a metal plate,” *Physical Review Letters*, vol. 93, pp. 173901–1–4, Oct. 2004.
- [102] B. Vasić, G. Isić, R. Gajić, and K. Hingerl, “Coordinate transformation based design of confined metamaterial structures,” *Physical Review B*, vol. 79, p. 085103, Feb. 2009.
- [103] E. Post, *Formal Structure of Electromagnetics: General Covariance and Electromagnetics*. Amsterdam: North-Holland, 1962.
- [104] J. Pendry, D. Schurig, and D. Smith, “Controlling electromagnetic fields,” *Science*, vol. 312, pp. 1780–1782, 2006.
- [105] W. Jiang, T. Cui, X. Zhou, X. Yang, and Q. Cheng, “Arbitrary bending of electromagnetic waves using realizable inhomogeneous and anisotropic materials,” *Physical Review E*, vol. 78, p. 066607, Dec. 2008.
- [106] R. Ghasemi, P.-H. Tichit, a. Degiron, a. Lupu, and a. de Lustrac, “Efficient control of a 3D optical mode using a thin sheet of transformation optical medium,” *Optics Express*, vol. 18, pp. 20305–12, Sept. 2010.
- [107] J. Zhang, Y. Luo, and N. A. Mortensen, “Transmission of electromagnetic waves through sub-wavelength channels,” *Optics Express*, vol. 18, pp. 3864–3870, Feb. 2010.
- [108] S. S. Zivanovic, K. S. Yee, and K. K. Mei, “A subgridding method for the time-domain finite-difference method to solve Maxwells equations,” *IEEE Transactions on Microwave Theory and Technique*, vol. 39, pp. 471–479, 1991.
- [109] D. T. Prescott and N. V. Shuley, “A method for incorporating different sized cells into the finite-difference time-domain analysis technique,” *IEEE Microwave and Guided Wave Letters*, vol. 2, pp. 434–436, 1992.
- [110] M. Okoniewski, E. Okoniewska, and M. A. Stuchly, “Three-dimensional subgridding algorithm for FDTD,” *IEEE Transactions on Antennas and Propagation*, vol. 45, pp. 422–429, March 1997.
- [111] W. Yu and R. Mittra, “A new subgridding method for the finite-difference time-domain (FDTD) algorithm,” *IEEE Microwave and Optical Technology Letters*, vol. 2, pp. 330–333, 1999.
- [112] D. M. Shyroki, “Exact equivalent straight waveguide model for bent and twisted waveguides,” *IEEE Transactions on Microwave Theory and Techniques*, vol. 56, no. 2, pp. 414–419, 2008.

- [113] D. M. Shyroki, A. M. Ivinskaya, and A. V. Lavrinenko, “Free-space squeezing assists perfectly matched layers in simulations on a tight domain,” *IEEE Antennas and Wireless Propagation Letters*, vol. 9, pp. 389–392, 2010.
- [114] I. Munteanu, M. Timm, and T. Weiland, “It’s about time,” *IEEE Microwave Magazine*, vol. 11, pp. 60–69, April 2010.
- [115] M. Besbes, J. P. Hugonin, P. Lalanne, S. van Haver, O. T. A. Janssen, A. M. Nugrowati, M. Xu, A. S. van de Nes, P. Bienstman, G. Granet, A. Moreau, S. Helfert, M. Sukharev, T. Seideman, F. I. Baida, B. Guizal, and D. Van Labeke, “Numerical analysis of a slit-groove diffraction problem,” *Journal of the European Optical Society - Rapid Publications*, vol. 2, pp. 07022–1–17, 2007.
- [116] J. Hoffmann, C. Hafner, P. Leidenberger, J. Hesselbarth, and S. Burger, “Comparison of electromagnetic field solvers for the 3D analysis of plasmonic nano antennas,” *Proceedings of SPIE*, vol. 7390, pp. 73900J–1–11, 2009.
- [117] J. Hoffmann, C. Hafner, P. Leidenberger, J. Hesselbarth, and S. Burger, “Comparison of electromagnetic field solvers for the 3D analysis of plasmonic nano antennas: Erratum,” *Proceedings of SPIE*, vol. 7390, pp. 73901G–1–2, 2009.
- [118] T. Weiland, “Time domain electromagnetic field computation with finite difference methods,” *International Journal of Numerical Modeling*, vol. 9, pp. 295–319, 1996.
- [119] A. Tafove and S. C. Hagness, *Computational Electrodynamics: The Finite-Difference Time-Domain Method*. Boston: MA Artech House, 2nd ed., 2000.
- [120] K. S. Yee, “Numerical solution of initial boudary value problems involving Maxwell’s equations in isotropic media,” *IEEE Transactions on Antennas Propagation*, vol. 14, pp. 302–307, 1966.
- [121] “Modulation theorem.” <http://mathworld.wolfram.com/ModulationTheorem.html>.
- [122] K. Srinivasan and O. Painter, “Momentum space design of high-Q photonic crystal optical cavities,” *Optics Express*, vol. 10, no. 15, pp. 5751–5758, 2002.
- [123] M. Notomi and H. Taniyama, “On-demand ultrahigh-Q cavity formation and photon pinning via dynamic waveguide tuning,” *Optics Express*, vol. 16, pp. 18657–66, Nov. 2008.

- [124] Y. Hua, "Generalized pencil-of-function method for extracting poles of an EM system from its transient response," *IEEE Transactions on Antennas and Propagation*, vol. 37, no. 2, pp. 229–234, 1989.
- [125] W.-h. Guo, W.-j. Li, and Y.-z. Huang, "Computation of resonant frequencies and quality factors of cavities by FDTD technique and Padé," *IEEE Microwave and Wireless Components Letters*, vol. 11, no. 5, pp. 223–225, 2001.
- [126] C. Wang, B.-Q. Gao, and C.-P. Deng, "Accurate study of Q-Factor of resonator by a finite-difference time-domain method," *IEEE Transactions on Microwave Theory and Techniques*, vol. 43, no. 7, pp. 1524–1529, 1995.
- [127] S. Dey, R. Mittra, and L. Fellow, "Efficient computation of resonant frequencies and quality factors of cavities via a combination of the finite-difference time-domain technique and the Pade approximation," *IEEE Microwave and Guided Wave Letters*, vol. 8, no. 12, pp. 415–417, 1998.
- [128] J. A. Pereda, "Computation of resonant frequencies and quality factors of open dielectric resonator by a combination of finite-difference time-domain method (FDTD) and Prony's methods," *IEEE Microwave Guided Wave Letters*, vol. 2, pp. 431–433, 1992.
- [129] "Harminv." <http://ab-initio.mit.edu/wiki/index.php/Harminv>.
- [130] H. A. Hulst, *Waves in Scattering Media*. Englewood Cliffs, New Jersey: Prentice-Hall Inc., 1984.
- [131] D. M. Shyroki, "Efficient Cartesian-grid-based modeling of rotationally symmetric bodies," *IEEE Transactions on Microwave Theory and Techniques*, vol. 55, no. 6, pp. 1132–1138, 2007.
- [132] S. Guo and S. Albin, "Numerical techniques for excitation and analysis of defect modes in photonic crystals," *Optics Express*, vol. 11, pp. 1080–1089, May 2003.
- [133] A. V. Boriskin, S. V. Boriskina, A. Rolland, R. Sauleau, and A. I. Nosich, "Test of the fdtd accuracy in the analysis of the scattering resonances associated with high-q whispering-gallery modes of a circular cylinder," *J. Opt. Soc. Am. A*, vol. 25, pp. 1169–1173, 2008.
- [134] R. D. Cook, *Concepts and Applications of Finite Element Analysis*. John Wiley & Sons, 4 ed., 2002.
- [135] M. Albani and P. Bernardi, "A numerical method based on the discretization of Maxwell equations in integral form," *IEEE Transactions on Microwave Theory and Techniques*, vol. 17, pp. 446–450, 1974.

- [136] W. Wilhelm, "Three dimensional resonator mode computation by finite difference method," *IEEE Transactions on Magnets*, vol. 21, pp. 2340–2343, 1985.
- [137] T. Weiland, "Numerical solution of maxwell's equation for static, resonant and transient problems," *DESY*, vol. 82-24, pp. 537–542, 1982.
- [138] T. Weiland, "On the computation of resonant modes in cylindrically symmetric cavities," *Nuclear Instruments and Methods*, vol. 216, pp. 329–348, 1983.
- [139] T. Weiland, "On the unique numerical solution of maxwellian eigenvalue problems in three dimensions," *Particle Accelerators*, vol. 17, pp. 227–242, 1985.
- [140] A. Christ and H. L. Hartnagel, "Three-dimensional finite-difference method for the analysis of microwave-device embedding," *IEEE Transactions of Microwave Theory Techniques*, vol. 35, pp. 688–696, 1987.
- [141] T. Weiland, M. Timm, I. Munteanu, and T. Weiland, "It's about time," *IEEE Microwave Magazine*, vol. 9, pp. 62–75, December 2008.
- [142] R. M. Makinen, H. D. Gersem, T. Weiland, and M. A. Kivikoski, "Modelling of lossy curved surfaces in the 3-D frequency-domain finite-difference methods," *International Journal of Numerical Modeling*, no. August, pp. 421–431, 2006.
- [143] G. Lubkowski, B. Bandlow, R. Schuhmann, and T. Weiland, "Effective modeling of double negative metamaterial macrostructures," *IEEE Transactions on Microwave Theory and Techniques*, vol. 57, no. 7, pp. 1136–1146, 2009.
- [144] T. Terao, "Computing interior eigenvalues of nonsymmetric matrices: Application to three-dimensional metamaterial composites," *Physical Review E*, vol. 82, pp. 026702–1–6, 2010.
- [145] D. M. Shyroki, "Modeling of sloped interfaces on a Yee grid," *IEEE Transactions on Antennas and Propagation*, in press, 2011.
- [146] J. T. Smith, "Conservative modeling of 3-d electromagnetic fields, part i: Properties and error analysis," *Geophysics*, vol. 61, pp. 1308–1318, 1995.
- [147] J. T. Smith, "Conservative modeling of 3-d electromagnetic fields, part ii: Biconjugate gradient solution and an accelerator," *Geophysics*, vol. 61, pp. 1319–1324, 1995.
- [148] R. B. Lehoucq, D. C. Sorensen, and C. Yang, *ARPACK users' guide: solution of large-scale eigenvalue problems with implicitly restarted Arnoldi methods*. Philadelphia: SIAM, 1998.

- [149] Y. Gong and J. Vuckovic, "Photonic crystal cavities in silicon dioxide," *Applied Physics Letters*, vol. 96, no. 3, p. 031107, 2010.
- [150] M. Belotti, M. Galli, D. Gerace, L. C. Andreani, G. Guizzetti, A. R. Md Zain, N. P. Johnson, M. Sorel, and R. M. De La Rue, "All-optical switching in silicon-on-insulator photonic wire nano-cavities," *Optics Express*, vol. 18, pp. 1450–1461, Jan. 2010.
- [151] S.-H. Kim, S.-K. Kim, and Y.-H. Lee, "Vertical beaming of wavelength-scale photonic crystal resonators," *Physical Review B*, vol. 73, p. 235117, 2006.
- [152] P. B. Deotare, M. W. McCutcheon, I. W. Frank, M. Khan, and M. Loncar, "Coupled photonic crystal nanobeam cavities," *Applied Physics Letters*, vol. 95, no. 3, p. 031102, 2009.
- [153] K. Foubert, L. Lalouat, B. Cluzel, E. Picard, D. Peyrade, F. de Fornel, and E. Hadji, "An air-slotted nanoresonator relying on coupled high Q small V Fabry-Perot nanocavities," *Applied Physics Letters*, vol. 94, no. 25, p. 251111, 2009.
- [154] S. Mandal, X. Serey, and D. Erickson, "Nanomanipulation using silicon photonic crystal resonators," *Nano Letters*, vol. 10, pp. 99–104, Jan. 2010.
- [155] H. J. Kimble, "The quantum internet," *Nature*, vol. 453, pp. 1023–30, June 2008.
- [156] S. Ha, A. A. Sukhorukov, A. V. Lavrinenko, and Y. S. Kivshar, "Cavity mode control in side-coupled periodic waveguides: Theory and experiment," *Photonics and Nanostructures - Fundamentals and Applications*, vol. 8, pp. 310–317, May 2010.
- [157] M. J. Steel, T. P. White, C. M. de Sterke, R. C. McPhedran, and L. C. Botten, "Symmetry and degeneracy in microstructured optical fibers," *Optics Letters*, vol. 26, pp. 488–490, 2001.
- [158] L. D. Landau and E. M. Lifshitz, *Quantum Mechanics*. USA: MA Addison Wesley, 1958.
- [159] M. A. Seo, H. R. Park, S. M. Koo, D. J. Park, J. H. Kang, O. K. Suwal, S. S. Choi, P. C. M. Planken, G. S. Park, N. K. Park, Q. H. Park, and D. S. Kim, "Terahertz field enhancement by a metallic nano slit operating beyond the skin-depth limit," *Nature Photonics*, vol. 3, pp. 152–156, March 2009.
- [160] M. Born and E. Wolf, *Principles of Optics*. Oxford: Pergamon Press, 1980.

- [161] M. Seo, J. Kyoung, H. Park, S. Koo, H.-s. Kim, H. Bernien, B. J. Kim, J. H. Choe, Y. H. Ahn, H.-T. Kim, N. Park, Q.-H. Park, K. Ahn, and D.-s. Kim, "Active Terahertz Nanoantennas Based on VO<sub>2</sub> Phase Transition," *Nano Letters*, vol. 10, pp. 2064–2068, May 2010.
- [162] Y. Takakura, "Optical resonance in a narrow slit in a thick metallic screen," *Physical Review Letters*, vol. 86, pp. 5601–5603, June 2001.
- [163] J. Suckling, A. Hibbins, M. Lockyear, T. Preist, J. Sambles, and C. Lawrence, "Finite conductance governs the resonance transmission of thin metal slits at microwave frequencies," *Physical Review Letters*, vol. 92, pp. 147401–1–4, Apr. 2004.
- [164] B. Sturman, E. Podivilov, and M. Gorkunov, "Transmission and diffraction properties of a narrow slit in a perfect metal," *Physical Review B*, vol. 82, p. 115419, Sept. 2010.
- [165] D. Wang, T. Yang, and K. B. Crozier, "Charge and current reservoirs for electric and magnetic field enhancement," *Optics Express*, vol. 18, pp. 10388–94, May 2010.
- [166] Y. Lu, W. Zhang, and M. Qiu, "Metamaterials, plasmonics, and THz frequency photonic components," *Active and Passive Electronic Components*, vol. 2007, 2008.
- [167] D. J. Park, S. B. Choi, Y. H. Ahn, F. Rotermund, I. B. Sohn, C. Kang, M. S. Jeong, and D. S. Kim, "Terahertz near-field enhancement in narrow rectangular apertures on metal film," *Optics Express*, vol. 17, pp. 12493–501, July 2009.
- [168] J. Kang, D. Kim, and Q.-H. Park, "Local capacitor model for plasmonic electric field enhancement," *Physical Review Letters*, vol. 102, pp. 093906–1–4, Mar. 2009.
- [169] B. Gelmont, R. Parthasarathy, T. Globus, A. Bykhovski, and N. Swami, "Terahertz (THz) electromagnetic field enhancement in periodic subwavelength structures," *IEEE Sensors Journal*, vol. 8, pp. 791–796, June 2008.
- [170] M. Kutteruf, "Terahertz spectroscopy of short-chain polypeptides," *Chemical Physics Letters*, vol. 375, pp. 337–343, July 2003.
- [171] J. Suckling, J. Sambles, and C. Lawrence, "Remarkable zeroth-order resonant transmission of microwaves through a single subwavelength metal slit," *Physical Review Letters*, vol. 95, pp. 187407–1–4, Oct. 2005.
- [172] T. Ribaud, D. C. Adams, B. Passmore, E. A. Shaner, and D. Wasserman, "Spectral and spatial investigation of midinfrared surface waves on a plasmonic grating," *Applied Physics Letters*, vol. 94, no. 20, p. 201109, 2009.

- [173] J. B. Pendry, L. Martín-Moreno, and F. J. Garcia-Vidal, “Mimicking surface plasmons with structured surfaces,” *Science*, vol. 305, pp. 847–8, Aug. 2004.
- [174] A. D. Pouliarikas, *The Transformations and Applications Handbook*. Florida: CRC Press LLC, 2010.
- [175] “Ansoft.” <http://www.ansoft.com>.